Coherent manipulation of normal and Andreev fermions

Vilkelis, K.

DOI
10.4233/uuid:1019957f-906a-4ca3-9abe-e1ae9479ef4f

Publication date
2024

Document Version
Final published version

Citation (APA)
Vilkelis, K. (2024). *Coherent manipulation of normal and Andreev fermions*. [Dissertation (TU Delft), Delft University of Technology]. https://doi.org/10.4233/uuid:1019957f-906a-4ca3-9abe-e1ae9479ef4f

Important note
To cite this publication, please use the final published version (if applicable).
Please check the document version above.

COHERENT MANIPULATION OF NORMAL AND ANDREEV FERMIONS

COHERENT MANIPULATION OF NORMAL AND ANDREEV FERMIONS

Dissertation

for the purpose of obtaining the degree of doctor
at Delft University of Technology
by the authority of the Rector Magnificus prof. dr. ir. T.H.J.J. van der Hagen,
chair of the Board for Doctorates,
to be defended publicly on
Monday 5 February 2024 at 12:30 o'clock

by

Kostas VILKELIS

Master of Chemical Physics, University of Edinburgh, United Kingdom
born in Vilnius, Lithuania

This dissertation has been approved by the

promotor: Dr. A. R. Akhmerov
copromotor: Dr. M. T. Wimmer

Composition of the doctoral committee:

Rector Magnificus,	chairperson
Dr. A. R. Akhmerov	Delft University of Technology, promotor
Dr. M. T. Wimmer	Delft University of Technology, copromotor

Independent members:

Prof. dr. J.M. Thijssen	Delft University of Technology
Prof. dr. A.F. Otte	Delft University of Technology
Dr. A. Chatterjee	Delft University of Technology
Dr. Ç. Girit	Collège de France, France
Dr. M. Veldhorst	Delft University of Technology, reserve member

This work was supported by the European Research Council (ERC) under the European Union's Horizon 2020 research and innovation program grant agreement No. 828948 (AndQC).

Printed by: Print&Bind

Front & Back: *Untitled, Untitled*, Kostas Vilkelis via Midjourney

ISBN 978-94-6384-535-9

An electronic version of this dissertation is available at
http://repository.tudelft.nl/.

Contents

SUMMARY

A large part of condensed matter physics concerns itself with understanding the behaviour of electrons in solids and finding ways to control them. However, in mesoscopic systems (i.e., systems with nanometer to micrometre scale), the behaviour of electrons is difficult to predict through the Schrödinger equation. Instead, it is often more fruitful to use an approximate semiclassical theory that re-introduces the concept of particle trajectories into the quantum world. These trajectories not only depend on the applied external fields but also on the Fermi surface of the material itself. The control over the Fermi surface allows to engineer electron trajectories not present in classical physics and therefore leads to new novel phenomena. For example, in highly anisotropic materials with open Fermi surfaces, the semiclassical trajectories of electrons in a magnetic field are no longer closed but instead move in an oscillating open trajectory that travels from one sample edge to the next. These open trajectories result in magnetoresistance oscillations with a period proportional to the flux passing through the sample — similar to the Aharonov–Bohm effect. However, unlike the Aharonov–Bohm effect, the magnetoresistance oscillations here are not due to interference effects.

Open trajectories not only lead to novel transport phenomena but also contribute to the magnetic response. Two counter-propagating open trajectories couple via boundary reflections and form an effective closed trajectory. Unlike usual cyclotron orbits that shrink with increasing magnetic field, these effective closed trajectories extend over the entire sample width irrespective of the magnetic field. The magnetic response of these effectively closed trajectories oscillates between diamagnetism and paramagnetism with a period proportional to the flux quanta passing through the area defined by the width of the sample and the distance between adjacent atomic layers. These oscillations are distinct from the de Haas–van Alphen effect, where due to the shrinking of cyclotron orbits the oscillation period is proportional to the inverse magnetic field. Additionally, these oscillations require sample-wide coherence and high-quality boundaries.

In mesoscopic systems, interfacing different materials is a common way to engineer devices with precise electronic properties. In particular, superconductor interfaces with other materials (e.g., semiconductors or ferromagnets) often host subgap Andreev bound states (ABS). The charge and energy of these ABS are highly electrically tunable through gate voltages and flux bias. As a result, ABS are excellent mediators of interactions between local fermionic modes. For example, a superconducting island between two quantum dots mediates the normal hopping and superconducting pairing processes between the dots. In addition, a tunable capacitor between the dots allows for control of the Coulomb interaction between them. Together, these processes allow precise electrical control of the fermionic modes within the dots and thus offer a practical implementation of a fermionic universal quantum computer. Our design consists of an array of quantum dots tunnel coupled by a hybrid superconducting island together with a tunable capacitor coupling the dots.

In addition to new devices, hybrid superconducting nanostructure makes it possible to engineer phases of matter — topological superconductors which host Majorana bound states. Majorana bound states are zero-energy modes that are their own antiparticles. Most modern attempts to realize Majorana bound states focus on hybrid superconducting nanostructures with strong spin-orbit coupling and an external magnetic field. Recent experiments suggest that instead of an external magnetic field, it might be possible to proximity-induce the required exchange field through a ferromagnetic material. To validate the validity of such a zero-field device, we perform detailed microscopic simulations and map the topological phase diagram as a function of gate voltages and proximity-induced exchange couplings. We show that the ferromagnetic hybrid nanowire with overlapping superconducting and ferromagnetic layers can become a topological superconductor within realistic parameter regimes.

An alternative way to realize a topological superconductor is to build a magnetic adatom chain atom-by-atom on a superconductor surface. These chains are known as Yu–Shiba–Rusinov (YSR or Shiba) chains. While several experiments realised YSR chains, realistic numerical modelling remains a challenge. To model a YSR chain correctly, we require a superconductor of a size much larger than the coherence length. Such a requirement is often computationally intractable in realistic systems. Instead, we propose to exploit the long coherence length of the superconductor through the short-junction approximation. The short-junction approximation reduces the whole superconductor to a boundary condition for the adatoms and thus allows a computationally cheaper method to model YSR chains. We further reduce the computational complexity of the short-junction approximation by removing modes that do not couple the adatoms to the superconductor. We do so by developing the concept of virtual leads — eigenmodes of the current operator — which provide a natural basis for the problem.

SAMENVATTING

Een groot deel van de fysica van gecondenseerde materie houdt zich bezig met het begrijpen van het gedrag van elektronen in vaste stoffen en het vinden van manieren om ze te beheersen. In mesoscopische systemen (d.w.z. systemen op nanometer- tot micrometerschaal) is het gedrag van elektronen echter moeilijk te voorspellen met de Schrödingervergelijking. In plaats daarvan is het vaak nuttiger om een benaderende semiklassieke theorie te gebruiken die het concept van deeltjesbanen opnieuw introduceert in de kwantumwereld. Deze banen zijn niet alleen afhankelijk van de toegepaste externe velden, maar ook van het Fermi-oppervlak van het materiaal zelf. De controle over het Fermi-oppervlak maakt het mogelijk om elektronenbanen te construeren die niet voorkomen in de klassieke fysica en leidt daarom tot nieuwe fenomenen. In zeer anisotrope materialen met open Fermi-oppervlakken zijn de semiklassieke banen van elektronen in een magnetisch veld bijvoorbeeld niet langer gesloten, maar bewegen ze in plaats daarvan in een oscillerende open baan die van de ene monsterrand naar de volgende gaat. Deze open banen resulteren in magnetoresistentie-oscillaties met een periode die evenredig is met de flux die door het monster gaat — vergelijkbaar met het Aharonov-Bohm effect. In tegenstelling tot het Aharonov-Bohm effect zijn de magnetoresistentie oscillaties hier echter niet het gevolg van interferentie effecten.

Open banen leiden niet alleen tot nieuwe transportverschijnselen maar dragen ook bij aan de magnetische respons. Twee tegengestelde voortbewegende open banen koppelen via grensreflecties en vormen een effectieve gesloten baan. In tegenstelling tot gebruikelijke cyclotronbanen die krimpen met toenemend magneetveld, strekken deze effectieve gesloten banen zich uit over de gehele monsterbreedte, ongeacht het magneetveld. De magnetische respons van deze effectief gesloten banen schommelt tussen diamagnetisme en paramagnetisme met een periode die evenredig is met de fluxquanta die door het gebied gaan dat gedefinieerd wordt door de breedte van het monster en de afstand tussen aangrenzende atoomlagen. Deze oscillaties zijn te onderscheiden van het de Haas–van Alphen effect, waarbij door het krimpen van cyclotronbanen de oscillatieperiode evenredig is met het omgekeerde magneetveld. Bovendien vereisen deze oscillaties monsterbrede coherentie en hoogwaardige grenzen.

In mesoscopische systemen is het samenstellen van verschillende materialen een gebruikelijke manier om apparaten te maken met nauwkeurige elektronische eigenschappen. In het bijzonder, supergeleider-oppervlakken met andere materialen (bijv. halfgeleiders of ferromagneten) bevatten vaak subkloof Andreev gebonden toestanden (ABS). De lading en energie van deze ABS zijn in hoge mate elektrisch afstembaar via gatespanningen en fluxbias. Daardoor zijn ABS uitstekende bemiddelaars van interacties tussen lokale fermionische toestanden. Zo bemiddelt een supergeleidend eiland tussen twee kwantumstippen de normale hopping en supergeleidende paarprocessen tussen de stippen. Daarnaast zorgt een afstembare condensator tussen de stippen voor controle over de Coulomb-interactie tussen de stippen. Samen maken deze processen een

nauwkeurige elektrische besturing van de fermionische toestanden binnen de stippen mogelijk en bieden zo een praktische implementatie van een fermionische universele quantumcomputer. Ons ontwerp bestaat uit een array van kwantumstippen die tunnelgekoppeld zijn door een hybride supergeleidend eiland, samen met een afstembare condensator die de stippen met elkaar verbindt.

Naast nieuwe apparaten maakt de hybride supergeleidende nanostructuur het mogelijk om fasen van materie te ontwikkelen — topologische supergeleiders die Majorana-gebonden toestanden dragen. Majorana gebonden toestanden zijn nulpunten van energie die hun eigen antideeltjes zijn. De meeste moderne pogingen om Majorana-gebonden toestanden te realiseren richten zich op hybride supergeleidende nanostructuren met een sterke spin-baankoppeling en een extern magneetveld. Recente experimenten suggereren dat in plaats van een extern magnetisch veld, het mogelijk zou kunnen zijn om het vereiste uitwisselingsveld nabij te induceren via een ferromagnetisch materiaal. Om de validiteit van een dergelijk nul-veld apparaat te valideren, voeren we gedetailleerde microscopische simulaties uit en brengen we het topologische fasediagram in kaart als functie van gatespanningen en nabijheids-geïnduceerde uitwisselingskoppelingen. We laten zien dat de ferromagnetische hybride nanodraad met overlappende supergeleidende en ferromagnetische lagen een topologische supergeleider kan worden binnen realistische parameterregimes.

Een alternatieve manier om een topologische supergeleider te realiseren is door een magnetische adatoomketen atoom voor atoom op te bouwen op een supergeleideroppervlak. Deze ketens staan bekend als Yu-Shiba-Rusinov (YSR of Shiba) ketens. Hoewel verschillende experimenten YSR-ketens realiseerden, blijft realistische numerieke modellering een uitdaging. Om een YSR-keten correct te modelleren, hebben we een supergeleider nodig die veel groter is dan de coherentielengte. Een dergelijke vereiste is vaak rekenkundig onuitvoerbaar in realistische systemen. In plaats daarvan stellen we voor om de lange coherentielengte van de supergeleider te benutten door middel van de korte-kringbenadering. De korte-splitsingsbenadering reduceert de hele supergeleider tot een randvoorwaarde voor de adatomen en maakt zo een rekenkundig goedkopere methode mogelijk om YSR-ketens te modelleren. We verminderen de rekenkundige complexiteit van de korte-koppelingbenadering verder door modi te verwijderen die de adatomen niet aan de supergeleider koppelen. Dit doen we door het concept van virtuele afleidingen — eigenmodes van de stroomoperator — te ontwikkelen die een natuurlijke basis voor het probleem vormen.

1

INTRODUCTION

1

1.1. PREFACE

The last century saw a great deal of progress in condensed matter physics: semiconductor devices ushered in electronics, liquid crystals paved the way for smartphones, the discovery of superconductors led to the development of strong magnets used in magnetic resonance imaging and maglev trains, and many more advances. What gives rise to these materials' characteristic properties is a specific basic constituent of matter — the electron. Today in condensed matter physics we understand the electron as a spin 1/2 fermion with dynamics governed by the Schrödinger equation. The Schrödinger equation is incredibly successful in explaining material properties, but it is in no way simple. Such a precise model is often unhelpful in understanding the underlying physics and often it is more useful to identify the key features of a phenomenon and choose a simpler model that captures these features.

In the most simple case, we can treat an electron as a simple ball-like particle with a fixed charge and a classical trajectory defined through Newton's laws of motion. Applied to metals, this model is known as the Drude model. While the model is crude, it does explain the conductivity of metals, the Hall effect and partly the Wiedmann-Franz law.

However, a fully classical description of electrons is not sufficient to explain more complex properties. In particular, the continuous phase space in the classical picture does not allow magnetism according to the Bohr–van Leeuwen. Therefore, to deal with magnetic phenomenon we need to borrow an important feature from quantum mechanics — quantisation. Quantisation allows only certain classical trajectories whose classical action fulfils the condition known as the Bohr–Sommerfeld quantisation. Such a combination of classical and quantum is known as the semiclassical theory. The semiclassical theory is a powerful yet simple tool to explain electron dynamics in electromagnetic fields and magnetic phenomena like the de Haas–van Alphen effect.

Things get even more involved when we consider superconductors. In superconductors, electrons form Cooper pairs and condense into a macroscopic quantum state. When we place a weak link such as a thin metal or insulator between two superconductors, current flows without any voltage applied — a phenomenon known as the Josephson effect. While superconductivity is an inherently quantum phenomenon, the Josephson effect does not require a full quantum description. In the weak link, instead of electron states, we now consider variable charge fermionic quasi-particles known as Andreev states. Andreev states are bound states of electrons and holes that in the weak link follow classical trajectories. At the superconductor interface, the particles retro-reflect and switch charge — an effect known as Andreev reflection. Andreev reflection leads to a current passing through the weak link at zero voltage bias, an effect known as the Josephson effect.

The semiclassical theory is a powerful tool that explains many phenomena on a mesoscopic scale, but it does have its limitations. Because particles have a fixed position and velocity in the semiclassical picture, interference is not possible. For example, a current in a ring oscillates with the passing magnetic flux as a result of interference of clockwise and counterclockwise moving electrons — known as the Aharonov–Bohm effect. Furthermore, concepts like entanglement and superposition are absent in semiclassics which makes it unsuitable to analyse strongly correlated phenomena. Lastly, semiclassics requires dynamics at length scales much larger than the de Broglie wavelength and therefore cannot explain the bandstructure in crystals.

1.2. SEMICLASSICAL EQUATIONS OF MOTION

The everyday macroscopic world we experience — the elliptical orbits of planets, the swings of a pendulum, the scattering of billiard balls — work according to the laws of classical mechanics. These constant reminders of Newton's laws of motion build an intuitive picture of the physics of the world around us. In part thanks to that, when faced with a classical mechanics problem, we often have a good idea of what solution to expect.

Despite its simplicity, classical mechanics is merely an approximation of a more fundamental theory. When we look at the world on a smaller scale — the world of electrons, atoms and molecules — the Newtonian picture breaks down. To get a valid description of the world, we turn to quantum mechanics. While valid, quantum mechanics is both more technically involved and less intuitive than classical mechanics: non-commuting operators replace commuting variables of position and momentum, and the trajectories of particles become wavefunctions which interfere as waves. Because of these difficulties, we often require various approximations to solve the Schrödinger equation.

While the quantum and classical pictures seem to govern different regimes, they are not mutually exclusive. In mesoscopic condensed matter systems, it is possible to combine the best of both theories. To illustrate this, consider an electron in a crystal lattice with potential $V(\mathbf{r})$ that is subject to additional slowly-varying external potential $U(\mathbf{r}, t)$ and magnetic field $B = \nabla \times \mathbf{A}(\mathbf{r}, t)$ where $\mathbf{r}$ is position and t is time. The time-dependent Schrödinger equation for such a system is

$$i\hbar\gamma \frac{\partial}{\partial \tau}\Psi(\rho,\tau) = \left[\frac{1}{2m_e}\left(-i\hbar\gamma\nabla_\rho - q_e A(\rho,\tau)\right)^2 + V(\rho) + U(\rho,\tau)\right]\Psi(\rho,\tau), \tag{1.1}$$

where m_e and q_e are the mass and charge of an electron. We re-scaled time, $t = \tau/\gamma$, and position, $r = \rho/\gamma$ where the small parameter γ describes the ratio between microscopic and macroscopic scales of the problem. A good choice of γ is the ratio between the Fermi (or de Broglie) wavelength λ_F and the relevant length scale of the problem L. The ratio between the derivatives of the external fields and the crystal potential is on the order of $O(\gamma)$. Because of this, we expect the crystal potential to dominate the fast oscillations of the wavefunction and the external fields to slowly modulate the overall amplitude.

To separate the dynamics of the system into two regimes, we use the Ansatz wavefunction

$$\Psi(\rho,\tau) = \Psi'(\rho,\tau)\, u_{n\mathbf{k}}(\rho) \exp\left(\frac{i}{\gamma\hbar} S(\rho,\tau)\right), \tag{1.2}$$

where Ψ' is the slowly modulating part and $u_k(\rho)$ is the n-th band eigenfunction of the crystal with crystal momentum $\mathbf{k}$:

$$\left(-\frac{\hbar^2\gamma^2}{2m_e}\nabla_p^2 + V(\rho)\right) u_{n\mathbf{k}}(\rho)\exp\left(i\mathbf{k}\cdot\rho\right) = \varepsilon_n(\mathbf{k})\, u_{n\mathbf{k}}(\rho)\exp\left(i\mathbf{k}\cdot\rho\right), \tag{1.3}$$

where $\varepsilon_n(\mathbf{k})$ is the band dispersion of the unperturbed crystal. Because the effect of the external field must be smaller than that of the crystal potential, we expand the slowly modulating part of the wavefunction in orders of the small parameter:

$$\Psi' = \Psi'_0 + \gamma\Psi'_1 + O(\gamma^2), \tag{1.4}$$

and solve Eq.(1.1) order by order — an approach known as the WKB approximation [1, 2]. At zeroth order, we obtain the eikonal equation that governs the overall motion of the particle [3, 4]:

$$-\frac{\partial S(\mathbf{r},t)}{\partial t} = \varepsilon_n\Big(\mathbf{k}(\mathbf{r},t) + \frac{q_e}{\hbar}\mathbf{A}(\mathbf{r},\tau)\Big) + U(\mathbf{r},t), \tag{1.5}$$

$$\hbar\mathbf{k}(\mathbf{r},t) = \nabla_r S(\mathbf{r},t), \tag{1.6}$$

where we switched back to the original position and time variables $(\mathbf{r}, t)$. Equation (1.5) is similar to the Hamilton–Jacobi equation from classical mechanics: the right-hand side acts as a classical Hamiltonian whereas the crystal momentum $\hbar\mathbf{k}$ corresponds to the canonical momentum and S is the classical action of a trajectory. Based on this correspondence, we transform Eq. (1.5) into Newtonian-like equations known as the semiclassical equations of motion:

$$\hbar\frac{d\kappa}{d\tau} = \nabla_r U(\mathbf{r},t) - q_e\frac{d\mathbf{r}}{dt}\times\mathbf{B}, \tag{1.7}$$

$$\frac{d\mathbf{r}}{dt} = \nabla_\kappa \varepsilon_n(\kappa), \tag{1.8}$$

$$\kappa(\mathbf{r},t) = \mathbf{k}(\mathbf{r},t) + \frac{q_e}{\hbar}\mathbf{A}(\mathbf{r},t), \tag{1.9}$$

where we introduced the kinetic crystal momentum κ. Equation (1.7) describes the evolution of kinetic momentum κ through the classical equation of a particle under the Lorentz force. However, the relationship between momentum is no longer proportional to velocity as is in classical mechanics. Instead, the velocity in Eq. (1.8) is now the group velocity of the wavepacket given by the band dispersion of the crystal. In other words, the electrons behave as an anisotropic classical liquid that follows the Fermi–Dirac distribution — a Fermi liquid. Such semiclassical treatment of electrons successfully explains electron transport properties in metals [5, 6], semiconductors [7, 8], 2D materials [9, 10] and magnetic multilayers [11]. In addition, a first-order γ term introduces modulation to the wavepacket Ψ_0' which leads to anomalous velocity and magnetic moment terms [4, 12]. These additions further explain the anomalous Hall effect [13, 14] and transport in Weyl metals [15].

While the semiclassical theory allows us to model many phenomena with ease, it does have its limitations. To begin with, the semiclassical theory assumes that quantum systems approximately follow classical dynamics, which is not always the case. It does not apply to systems where effects such as superposition and entanglement are significant. In addition, it does not account for the wave nature of particles and therefore cannot explain interference and diffraction phenomena. Furthermore, it fails to accurately describe phenomena at small position and time scales. Rather, it is only valid when the de Broglie wavelength of the particle is much smaller than the length scale of the problem. Additionally, semiclassics treats each band separately and does not account for transitions between them.[1] To ensure no transitions, a large band gap must separate the bands and any applied external fields must be weak enough to not cause transitions.

[1] Although it is worthwhile to note that it is possible to extend the semiclassical equations to two coupled bands [16–18] and spin transport [19].

1.3. SEMICLASSICAL QUANTISATION

Classical physics deals with continuous quantities such as energy, angular momentum, magnetic flux, etc. However, in quantum mechanics, physical quantities cannot take any arbitrary values but rather must be quantised — allowing only integer multiples of some fundamental unit. Quantisation is a direct consequence of the wave nature of particles in quantum mechanics and is necessary to ensure that the wavefunction is single-valued. In practice, quantisation arises from the application of boundary conditions to the wavefunction. For example, in a box of length L, the wavefunction must fulfil hard-wall boundary conditions $\Psi(0) = \Psi(L) = 0$ for the particle to stay within the box. The constraint forces the wavefunction to be a standing wave within the box with wavevector $k = n\pi/L$ where n is an integer. Similarly, the semiclassical wavefunction in Eq. (1.2) must fulfil the periodic boundary conditions $\Psi(\rho,\tau) = \Psi(\rho + L,\tau)$ to be a valid solution. In general, these restrictions give rise to Bohr–Sommerfeld quantisation condition [20] which states the action of a closed trajectory must be quantised [21, 22]:

$$S(E)/\hbar \equiv \oint_{\varepsilon(\mathbf{k})=E} \mathbf{k}(\mathbf{r}) \cdot d\mathbf{r} = 2\pi n + \gamma_M + \gamma_B, \tag{1.10}$$

where n is an integer and $\mathbf{k}(\mathbf{r})$ is the canonical crystal momentum as a function of orbit position $\mathbf{r}$. We assumed that the Hamiltonian is time-independent and therefore the dynamics conserve the total energy E. An analogous interpretation is that the total phase accumulated along a closed trajectory must be an integer multiple of 2π. Based on this interpretation, we identify the left-hand side of Eq. (1.10) as a dynamic phase accumulated along a trajectory where the trajectory follows a constant energy contour along $\varepsilon(\mathbf{k}) = E$. In addition to the dynamical phase, the total phase also contains contributions from the Maslov index γ_M and the Berry phase γ_B. The Maslov index takes into account the phase accumulation at classical turning points — points where the particle switches its direction of motion [23]. In practice, these arise due to boundary reflections. Each reflection from a hardwall boundary, such as a discrete potential step, contributes a phase of π. On the other hand, a reflection from a soft continuous potential, such as a potential well, contributes a phase of $\pi/2$. Similarly to a soft potential, particle direction switching due to a magnetic field also contributes a phase of $\pi/2$. Lastly, the Berry phase originates from the periodic adiabatic evolution of the system and only arises in crystals without inversion and time-reversal symmetry [24]. We shall neglect the Berry phase contribution in this thesis, so $\gamma_B = 0$.

As an example, consider a particle in a box of length L. In the absence of any fields, the particle moves with constant momentum and reflects twice from the hard-wall boundaries such that $\gamma_M \mod 2\pi = 0$. The quantisation condition in Eq. (1.10) allows only certain momenta $k = n\pi/L$. Because we know that the momentum is related to the energy through the dispersion relation $\varepsilon = \hbar^2 k^2/2m$, we rewrite the quantisation condition in terms of energy:

$$\varepsilon_n = \frac{1}{2m}\left(\frac{\hbar\pi n}{L}\right)^2, \tag{1.11}$$

which is the energy spectrum of a particle in a box.

Similarly, we can apply the quantisation condition to a harmonic oscillator where the particle is trapped in a parabolic potential well $V(x) = m\omega^2 x^2/2$. In this case, the

momentum reads:

$$k(x) = \pm\sqrt{2m\left(E - m\omega^2 x^2/2\right)}, \tag{1.12}$$

where $\pm$ corresponds to the two directions of motion. Additionally, the particle changes its motion twice due to the soft potential turning points at $x_\pm = \pm\sqrt{2E/(m\omega^2)}$ and therefore obtains phase $\gamma_M = \pi$. As a result, Eq. (1.10) defines the allowed energies of the oscillator:

$$\varepsilon_n = \hbar\omega\left(n + \frac{1}{2}\right), \tag{1.13}$$

which is the energy spectrum of a quantum harmonic oscillator.

1.4. ORBITAL MAGNETIC RESPONSE

As a final example, consider a particle in a uniform magnetic field $\mathbf{B} = B\hat{\mathbf{z}}$ where $\mathbf{z}$ is the unit vector along z-direction. The particle moves in a closed cyclotron orbit such that the direction of motion smoothly switches twice and therefore the Maslov phase is $\gamma_M = \pi$. We choose the Landau gauge vector potential $\mathbf{A} = -By\hat{\mathbf{x}}$ in which the quantisation condition in Eq. (1.10) reads:

$$\oint k_y(y)\,dy = 2\pi\left(n + \frac{1}{2}\right), \tag{1.14}$$

whereas k_x and k_z do not appear in the integral because they are both constants of motion due to the specific choice of the gauge. The equations of motion in Eqs. (1.7—1.9) directly define the evolution of kinetic momentum κ rather than the canonical momentum k. Therefore, it is more convenient to re-write Eq. (1.14) in terms of the kinetc momentum [20, 25]:

$$A(E, k_z) \equiv \oint \kappa_y d\kappa_x = \frac{2\pi}{l_B^2}\left(n + \frac{1}{2}\right), \tag{1.15}$$

where we used $\hbar d\kappa_x = q_e B dy$ and defined the magnetic length $l_B = \sqrt{\hbar/(q_e B)}$. Equation (1.15) quantises the allowed area enclosed by the momentum trajectory, $A(E, k_z)$. In the case of a simple isotropic dispersion, it is easy to show that Equation (1.15) correctly calculates the Landau energy levels. More importantly, Eq. (1.15) allows us to identify the general properties of a system with any dispersion relation. For example, the energy levels of any system in a finite magnetic field B shift by ΔE [25]:

$$\Delta E = E_{n+1} - E_n \approx \frac{2\pi}{l_B^2}\left(\frac{\partial A(E, k_z)}{\partial E}\right)^{-1}. \tag{1.16}$$

Because the energy levels shift, the total energy changes and the system develops finite magnetisation as a result. At a weak magnetic field B, this magnetisation is proportional to the applied magnetic field and is known as Landau diamagnetism [26]. At higher magnetic fields, the magnetisation starts to oscillate with the inverse magnetic field and is known as the de Haas–van Alphen effect [27]. The main contributions to the de Haas–van Alphen effect come from energy levels shifting around the Fermi energy E_F, and therefore the period of these oscillations is directly related to the Fermi surface cross-section perpendicular to the magnetic field:

$$\frac{1}{B_{n+1}} - \frac{1}{B_n} \approx \frac{2\pi q_e}{\hbar A(E_F, k_z)}. \tag{1.17}$$

By measuring the period of these oscillations at different magnetic field orientations, it is possible to reconstruct the full Fermi surface of a metal [28, 29].

1.5. SUPERCONDUCTIVITY

In simple systems such as metals, semiconductors, and insulators — the global phase of the wavefunction does not influence physical properties and therefore we often neglect it. However, that is not the case in superconductors. Superconductors are a class of materials that transmit electric current without any resistance and perfectly expel magnetic fields from their interior. According to BCS theory [30], these strange properties originate from the formation of electron pairs, called Cooper pairs[2]. These Cooper pairs condense into a perfectly coherent macroscopic ground state which leads to a well-defined global phase of the wavefunction. To parametrise the superconductivity we use the superconducting order parameter $\Delta = |\Delta| e^{i\phi}$ where $|\Delta|$ is the superconducting gap value and ϕ is the superconducting phase.

The most common and simplest superconductivity is spin-singlet s-wave where electrons with opposite spin form Cooper pairs. To describe such a superconducting state, we use a four-component Bogoliubov-de Gennes (BdG) Hamiltonian:

$$\hat{H}_{\mathrm{BdG}} = \left(-\frac{\hbar^2 \nabla^2}{2m} - \mu + V(x) \right) \tau_z + \Delta(x) \sigma_y \tau_x, \tag{1.18}$$

where μ is the chemical potential, V is the potential, σ_i and τ_i are Pauli matrices that act on spin and particle-hole spaces respectively.

Whenever the parameters $V(x), \Delta(x)$ in Eq. (1.18) are slowly varying in space, the semiclassical WKB approximation from the previous section applies. Furthermore, we assume that μ is much larger than the superconducting order parameter and the energy of the system, $\Delta(x), E \ll \mu$. These two approximations allow us to conveniently partition the wavefunction into the slowly and rapidly modulating parts [33]:

$$\Psi(x) = \Psi_+(x) \exp\left(i \int_{x_0}^{x} k_F(x') dx' \right) + \Psi_-(x) \exp\left(-i \int_{x_0}^{x} k_F(x') dx' \right), \tag{1.19}$$

where we define the position dependent Fermi wavector $k_F(x) = \sqrt{2m\left(\mu + V(x)\right)}/\hbar$. The slowly modulating spinors have physical meaning: Ψ_+ describes the right-moving electrons and left-moving holes, and Ψ_- describes the left-moving electrons and right-moving holes. These two slowly modulating spinors follow the semiclassical BdG Hamiltonian

$$\hat{H}_\pm = \mp i \tau_z \frac{\hbar^2 k_F(x)}{m} \frac{\partial}{\partial x} + \Delta(x) \sigma_y \tau_x. \tag{1.20}$$

Assuming spatially homogeneous potentials $\Delta(x) = \Delta, V(x) = V$, the eigenproblem defined through the Hamiltonian in Eq. (1.20) reduces to a matrix ordinary differential equation:

$$\frac{d\Psi_\pm(x)}{dx} = \pm \frac{m}{\hbar^2 k_F} \left(E\tau_z + i\Delta \sigma_y \tau_y \right) \psi_\pm(x). \tag{1.21}$$

[2] See the following references for a more pedagogical introduction to superconductivity [31, 32]

At $E = 0$, we see that the solutions to Eq. (1.21) must be eigenfunctions of $\sigma_y \tau_y$ which are equal superpositions of electrons and holes. Additionally, we note that there are no plane wave solutions to Eq. (1.21) whenever $E < |\Delta|$. In large superconductors that means that no quasiparticles exist below the superconducting gap.

1.6. ANDREEV BOUND STATES

In Section 1.5, we briefly discussed some of the properties of a single bulk s-wave superconductor. In practise we often deal with superconductors in contact with other, different materials like metals, ferromagnets or semiconductors. These heterojunctions lead to novel phenomena which are not possible in each material separately. Here, we shall focus on one such phenomenon — Andreev reflection [34].

Consider a metal-superconductor (NS) junction where an electron with energy $E < |\Delta|$ approaches the superconductor from the metal side. If the superconductor was a normal metal, the electron would simply transmit into it as an electron quasiparticle. However, the superconductor is not a normal metal — due to the condensation of Cooper pairs at the Fermi energy, it has a quasiparticle gap of size $|\Delta|$. Instead, the electron transmits into the superconductor as a Cooper pair and leaves behind a hole to conserve the overall charge. To conserve the momentum, the left-over hole appears to retro-reflect from the superconductor. Such a process is known as Andreev reflection. A similar process happens in reverse when a hole approaches the superconductor from the metal: a Cooper pair in the superconductor breaks apart and one of its electrons recombines with the hole, leaving the other electron behind. Because the leftover electron is from the Cooper pair, it acquires the superconducting phase and an additional phase from the reflection process itself [34]:

$$\phi_A = \phi - \cos^{-1}\left(\frac{E}{|\Delta|}\right), \tag{1.22}$$

where ϕ is the superconducting phase.

While the phases in Eq. (1.22) seem redundant in an NS junction, they become important in a superconductor-normal-superconductor (SNS) junction also known as a Josephson junction. Consider the left superconductor and right superconductor to have superconducting order parameters $\Delta_L = |\Delta|$ and $\Delta_R = |\Delta| e^{i\phi}$ respectively. As a result of two successive Andreev reflections, the electron and hole in the middle metal form a bound state known as the Andreev bound state [35]. To find the energy of the Andreev bound state, we use the Bohr–Sommerfeld quantisation condition [36, 37] in Eq. (1.10) and calculate the reflection (Maslov) phase according to Eq.(1.22):

$$2k_F L = 2\pi n + 2\cos^{-1}\left(\frac{E}{|\Delta|}\right) - \phi, \tag{1.23}$$

where L is the length and k_F is the Fermi momentum of the metal. We assume the short-junction limit, $k_F L \ll 1$, and therefore disregard the dynamic phase term which gives the phase-dependent energy of the Andreev bound state:

$$E_A = \Delta \cos\left(\frac{\phi}{2}\right). \tag{1.24}$$

Upon a single closed trajectory, the particle experiences two Andreev reflections: at one superconductor it breaks apart a Cooper pair and at the other, it creates a Cooper pair. Overall, a single Cooper pair transmits through the junction even tho we did not apply any voltage bias. This phenomenon is known as the Josephson effect and the passing current is known as the Josephson current [38]. Josephson junctions form the basis of modern electronic devices such as superconducting quantum interference devices (SQUIDs) [39], superconducting charge and flux qubits [40].

In addition to the Josephson effect, Andreev bound states give rise to many other interesting phenomena and thus are a subject of intense research in mesoscopic physics. Andreev bound states act as a tunable mediator between elastic co-tunelling and crossed Andreev reflection in devices called Cooper pair splitters [41–43]. In addition, the microscopic Andreev states couple strongly to electromagnetic fields and therefore are a prospective candidate for qubit realisation [32].

1.7. MAJORANA BOUND STATES

In Section 1.5, we discussed the simplest superconducting state — an s-wave spin-singlet state. There exist other superconducting states with different spatial and spin symmetries. One of the more interesting ones is the spin-triplet p-wave superconductivity (also known as topological superconductivity) that pairs electrons with the same spin. While intrinsic p-wave superconductivity is not yet observed, it is possible to engineer it by combining a spin-singlet s-wave superconductor with a one-dimensional spin-orbit coupled material (nanowire) in a magnetic field [33, 44]:

$$\hat{H}_{\mathrm{BdG}} = \left(\frac{\hat{p}^2}{2m} - \mu + V(x) - B\sigma_x + \alpha p \sigma_y \right) \tau_z + \Delta(x) \sigma_y \tau_x, \tag{1.25}$$

where Δ is now the proximity-induced superconducting gap, B is the Zeeman energy due to the applied magnetic field, and α is the spin-orbit coupling strength. The potential that confines the electron to the semiconductor is $V(x)$ and we assume that near one of the nanowire's edges, it is approximated by a linear potential $V(x) = \mu - V'x$.

Equation (1.25) is similar to Eq. (1.18) and therefore the semiclassical WKB approximation used in Section 1.5 also applies. However, the presence of spin-orbit coupling complicates the problem and it is simpler to perform a basis transformation on the coordinate x such that spin-orbit coupling becomes an effective position-dependent magnetic field (see Ref. [33] for detailed derivation). In the limit of $B \gg \Delta$ and $V' \ll B\Delta/(\hbar\alpha)$ there exists near-zero energy solutions at the edges of the nanowire:

$$E \approx \Delta \exp\left(-\frac{B^3}{\hbar\alpha V' \Delta} \right). \tag{1.26}$$

These solutions are known as the Majorana bound states.

Majorana bound states are similar to Andreev bound states at zero energy: they are both chargeless, spinless, their own antiparticles. However, unlike Andreev bound states which are fermions, Majorana bound states are non-abelian anyons: exchanging two Majoranas results in a unitary transformation that is not just an overall phase factor. In addition, Majorana bound states are non-local and appear in pairs at the opposite

edges of the nanowire. The non-locality of the Majorana bound states also means that they are not affected by local perturbations such as disorder. For example, by comparing Eq. (1.24) to Eq. (1.26) we see that Andreev bound state energy is sensitive to the variations of superconducting phase whereas the Majorana bound state is not sensitive to any local parameter variations as long as its deep within the topological phase. The non-abelian exchange statistics and protection against local perturbations make Majorana bound states a promising candidate for topological quantum computation [44–47].

1.8. THIS THESIS

The motion of electrons in a crystal determines the electronic transport properties of the material. For example, the Hall effect is a well-known phenomenon where a current-carrying conductor develops a voltage perpendicular to the applied current and magnetic field. The origin of the effect is the Lorentz force which deflects the electrons in the conductor and therefore creates a charge imbalance. The explanation assumes the band structure of the conductor is isotropic and therefore the electrons move in simple circular orbits. However, the motion of electrons in crystals is not always so simple. Many metals have a highly anisotropic structure which makes the trajectories also anisotropic. In Chapter 2, we consider one such anisotropic system — a quasi-two-dimensional electron gas in an in-plane magnetic field. Because of the anisotropy, the orbit of an electron in a magnetic field is no longer closed. Instead, it moves in an oscillating open trajectory that travels from one sample edge to the next. These open trajectories result in magnetoresistance oscillations [48] that closely resemble the Aharonov–Bohm effect. However, unlike the Aharonov–Bohm effect, the observed magnetoresistance oscillations do not rely on phase coherence and instead only require ballistic transport.

The magnetic response of a material also depends on the trajectories of its electrons. For example, the oscillations in the de Haas–van Alphen effect depend directly on the shape of the closed electron trajectories [25]. Therefore, one might expect that open orbits do not have a diamagnetic response. Contrary to this expectation, in Chapter 3 we show that open orbits in finite systems do contribute to the magnetic response that oscillates between diamagnetism and paramagnetism. The oscillations are similar to the Aharonov–Bohm effect because the oscillation phase is set by the number of flux quanta through the area defined by the width of the sample and the distance between adjacent atomic layers. The magnetic response originates from the closed trajectories formed by counter-propagating open orbits coupled via specular boundary reflections. The phenomenon acts as a probe of the phase coherence of open electron trajectories.

Thanks to advances in hybrid nanostructure fabrication [49], it is now possible to combine physical properties from different materials into a single device. In particular, the combination of semiconductors and superconductors [50, 51] allows to engineer of new electronic devices with novel properties. Chapter 4 proposes a practical implementation of a universal quantum computer that uses local fermionic modes rather than qubits. Our design consists of an array of quantum dots tunnel coupled by a hybrid superconducting island together with a tunable capacitor coupling the dots. The superconductor islands host Andreev bound states which act as a tunable mediator of interaction between the dots [41–43]. We show that coherent control of Cooper pair splitting, elastic cotunneling, and Coulomb interactions allows us to implement the universal set of quantum gates

defined by Bravyi and Kitaev [52]. Finally, we discuss possible limitations of the device and list necessary experimental efforts to overcome them.

In addition to new devices, hybrid nanostructure makes it possible to engineer novel phases of matter — topological superonductors [53]. In Chapter 5, we study the electronic properties of InAs/EuS/Al heterostructures as explored in a recent experiment [54], combining both spectroscopic results and microscopic device simulations. In particular, we use angle-resolved photoemission spectroscopy to investigate the band bending at the InAs/EuS interface. The resulting band offset value serves as an essential input to subsequent microscopic device simulations, allowing us to map the electronic wave function distribution. We conclude that the magnetic proximity effects at the Al/EuS as well as the InAs/EuS interfaces are both essential to achieve topological superconductivity at zero applied magnetic field. Mapping the topological phase diagram as a function of gate voltages and proximity-induced exchange couplings, we show that the ferromagnetic hybrid nanowire with overlapping Al and EuS layers can become a topological superconductor within realistic parameter regimes.

Another proposed platform to host topological superconductivity is a chain of magnetic adatoms on a superconducting substrate — a Yu–Shiba-Rusinov (YSR or Shiba) chain [55–58]. While the theory of such chains is well-established [56, 57], their exact modelling is challenging. To model a YSR chain correctly, we need to ensure that the size of the superconductor is much larger than the superconducting coherence length. In practice, this requirement makes the modelling of YSR chains computationally intractable. In Chapter 6, we propose a computationally cheaper method to model YSR chains that employ the short-junction approximation [59]. We further reduce the computational complexity of the short-junction approximation by removing modes that do not couple the adatoms to the superconductor. We do so by developing the concept of virtual leads — eigenmodes of the current operator — which provide a natural basis for the problem. We demonstrate the efficiency of our method by calculating the dispersion of a YSR chain.

1

REFERENCES

[1] S. C. Miller and R. H. Good, *A wkb-type approximation to the schrödinger equation,* Physical Review **91**, 174–179 (1953).

[2] N. Balazs, *One dimensional band theory in the wkb approximation,* Annals of Physics **53**, 421–438 (1969).

[3] J. Guillot, J. Ralston, and E. Trubowitz, *Semi-classical asymptotics in solid state physics,* Communications in mathematical physics **116**, 401 (1988).

[4] M. Dimassi, J. C. Guillot, and J. Ralston, *Semiclassical asymptotics in magnetic bloch bands,* Journal of Physics A: Mathematical and General **35**, 7597–7605 (2002).

[5] D. A. Greenwood, *The boltzmann equation in the theory of electrical conduction in metals,* Proceedings of the Physical Society **71**, 585–596 (1958).

[6] W. Li, *Electrical transport limited by electron-phonon coupling from boltzmann transport equation: An ab initio study of si, al, and* mos_2, Phys. Rev. B **92**, 075405 (2015).

[7] V. Sverdlov, E. Ungersboeck, H. Kosina, and S. Selberherr, *Current transport models for nanoscale semiconductor devices,* Materials Science and Engineering: R: Reports **58**, 228–270 (2008).

[8] M. Nedjalkov, H. Kosina, S. Selberherr, C. Ringhofer, and D. K. Ferry, *Unified particle approach to wigner-boltzmann transport in small semiconductor devices,* Physical Review B **70** (2004), 10.1103/physrevb.70.115319.

[9] S. Adam, E. Hwang, and S. Das Sarma, *Scattering mechanisms and boltzmann transport in graphene,* Physica E: Low-dimensional Systems and Nanostructures **40**, 1022–1025 (2008).

[10] S. Adam and S. Das Sarma, *Boltzmann transport and residual conductivity in bilayer graphene,* Physical Review B **77** (2008), 10.1103/physrevb.77.115436.

[11] A. Barthélémy and A. Fert, *Theory of the magnetoresistance in magnetic multilayers: Analytical expressions from a semiclassical approach,* Physical Review B **43**, 13124–13129 (1991).

[12] G. Sundaram and Q. Niu, *Wave-packet dynamics in slowly perturbed crystals: Gradient corrections and berry-phase effects,* Physical Review B **59**, 14915–14925 (1999).

[13] N. Nagaosa, J. Sinova, S. Onoda, A. H. MacDonald, and N. P. Ong, *Anomalous hall effect,* Reviews of Modern Physics **82**, 1539–1592 (2010).

[14] N. A. Sinitsyn, *Semiclassical theories of the anomalous hall effect,* Journal of Physics: Condensed Matter **20**, 023201 (2007).

[15] K.-S. Kim, H.-J. Kim, and M. Sasaki, *Boltzmann equation approach to anomalous transport in a weyl metal,* Physical Review B **89** (2014), 10.1103/physrevb.89.195137.

[16] D. Culcer, Y. Yao, and Q. Niu, *Coherent wave-packet evolution in coupled bands,* Physical Review B **72** (2005), 10.1103/physrevb.72.085110.

[17] C. Leblanc, G. Malpuech, and D. D. Solnyshkov, *Universal semiclassical equations based on the quantum metric for a two-band system,* Physical Review B **104** (2021), 10.1103/physrevb.104.134312.

[18] M. Di Liberto, N. Goldman, and G. Palumbo, *Non-abelian bloch oscillations in higher-order topological insulators,* Nature Communications **11** (2020), 10.1038/s41467-020-19518-x.

[19] D. Culcer, J. Sinova, N. A. Sinitsyn, T. Jungwirth, A. H. MacDonald, and Q. Niu, *Semiclassical spin transport in spin-orbit-coupled bands,* Physical Review Letters **93** (2004), 10.1103/physrevlett.93.046602.

[20] L. Onsager, *Interpretation of the de haas-van alphen effect,* The London, Edinburgh, and Dublin Philosophical Magazine and Journal of Science **43**, 1006–1008 (1952).

[21] A. Alexandradinata and L. Glazman, *Semiclassical theory of landau levels and magnetic breakdown in topological metals,* Physical Review B **97** (2018), 10.1103/physrevb.97.144422.

[22] J. N. Fuchs, F. Piéchon, M. O. Goerbig, and G. Montambaux, *Topological berry phase and semiclassical quantization of cyclotron orbits for two dimensional electrons in coupled band models,* The European Physical Journal B **77**, 351–362 (2010).

[23] J. B. Keller, *Corrected bohr-sommerfeld quantum conditions for nonseparable systems,* Annals of Physics **4**, 180–188 (1958).

[24] G. P. Mikitik and Y. V. Sharlai, *Manifestation of berry's phase in metal physics,* Physical Review Letters **82**, 2147–2150 (1999).

[25] I. Lifshitz and A. Kosevich, *Theory of magnetic susceptibility in metals at low temperatures,* Sov. Phys. JETP **2**, 636 (1956).

[26] L. Landau, *Diamagnetismus der metalle,* Zeitschrift für Physik **64**, 629 (1930).

[27] D. Haas and W. J. Van Alphen, *The dependence of the susceptibility of diamagnetic metals upon the field,* Proc. Netherlands Roy. Acad. Sci **33** (1930).

[28] D. Shoenberg, *The fermi surfaces of copper, silver and gold. i. the de haas-van alphen effect,* Philosophical Transactions of the Royal Society of London. Series A, Mathematical and Physical Sciences **255**, 85 (1962).

[29] D. Shoenberg and P. J. Stiles, *The de haas van alphen effect in alkali metals,* Proceedings of the Royal Society of London. Series A. Mathematical and Physical Sciences **281**, 62 (1964).

[30] J. Bardeen, L. N. Cooper, and J. R. Schrieffer, *Theory of superconductivity,* Physical Review **108**, 1175–1204 (1957).

[31] M. Tinkham, *Introduction to Superconductivity*, Dover Books on Physics Series (Dover Publications, 2004).

[32] M. Hays, V. Fatemi, D. Bouman, J. Cerrillo, S. Diamond, K. Serniak, T. Connolly, P. Krogstrup, J. Nygård, A. Levy Yeyati, A. Geresdi, and M. H. Devoret, *Coherent manipulation of an andreev spin qubit,* Science **373**, 430–433 (2021).

[33] G. Kells, D. Meidan, and P. W. Brouwer, *Near-zero-energy end states in topologically trivial spin-orbit coupled superconducting nanowires with a smooth confinement,* Physical Review B **86** (2012), 10.1103/physrevb.86.100503.

[34] B. Pannetier and H. Courtois, Journal of Low Temperature Physics **118**, 599–615 (2000).

[35] J. A. Sauls, *Andreev bound states and their signatures,* Philosophical Transactions of the Royal Society A: Mathematical, Physical and Engineering Sciences **376**, 20180140 (2018).

[36] K. Duncan and B. Györffy, *Semiclassical theory of quasiparticles in the superconducting state,* Annals of Physics **298**, 273–333 (2002).

[37] C. W. J. Beenakker and H. van Houten, *Josephson current through a superconducting quantum point contact shorter than the coherence length,* Physical Review Letters **66**, 3056–3059 (1991).

[38] A. A. Golubov, M. Y. Kupriyanov, and E. Il'ichev, *The current-phase relation in josephson junctions,* Reviews of Modern Physics **76**, 411–469 (2004).

[39] R. L. Fagaly, *Superconducting quantum interference device instruments and applications,* Review of Scientific Instruments **77** (2006), 10.1063/1.2354545.

[40] Y. Makhlin, G. Schön, and A. Shnirman, *Quantum-state engineering with josephson-junction devices,* Reviews of Modern Physics **73**, 357–400 (2001).

[41] C.-X. Liu, G. Wang, T. Dvir, and M. Wimmer, *Tunable superconducting coupling of quantum dots via andreev bound states in semiconductor-superconductor nanowires,* Physical Review Letters **129** (2022), 10.1103/physrevlett.129.267701.

[42] G. Wang, T. Dvir, G. P. Mazur, C.-X. Liu, N. van Loo, S. L. D. ten Haaf, A. Bordin, S. Gazibegovic, G. Badawy, E. P. A. M. Bakkers, M. Wimmer, and L. P. Kouwenhoven, *Singlet and triplet cooper pair splitting in hybrid superconducting nanowires,* Nature **612**, 448–453 (2022).

[43] T. Dvir, G. Wang, N. van Loo, C.-X. Liu, G. P. Mazur, A. Bordin, S. L. D. ten Haaf, J.-Y. Wang, D. van Driel, F. Zatelli, X. Li, F. K. Malinowski, S. Gazibegovic, G. Badawy, E. P. A. M. Bakkers, M. Wimmer, and L. P. Kouwenhoven, *Realization of a minimal kitaev chain in coupled quantum dots,* Nature **614**, 445–450 (2023).

[44] M. Sato and Y. Ando, *Topological superconductors: a review,* Reports on Progress in Physics **80**, 076501 (2017).

[45] A. Kitaev, *Fault-tolerant quantum computation by anyons,* Annals of Physics **303**, 2–30 (2003).

[46] A. Stern and N. H. Lindner, *Topological quantum computation—from basic concepts to first experiments,* Science **339**, 1179–1184 (2013).

[47] T. Hyart, B. van Heck, I. C. Fulga, M. Burrello, A. R. Akhmerov, and C. W. J. Beenakker, *Flux-controlled quantum computation with majorana fermions,* Physical Review B **88** (2013), 10.1103/physrevb.88.035121.

[48] C. Putzke, M. D. Bachmann, P. McGuinness, E. Zhakina, V. Sunko, M. Konczykowski, T. Oka, R. Moessner, A. Stern, M. König, S. Khim, A. P. Mackenzie, and P. J. Moll, *h/e oscillations in interlayer transport of delafossites,* Science **368**, 1234 (2020), https://www.science.org/doi/pdf/10.1126/science.aay8413 .

[49] C. Tan, J. Chen, X.-J. Wu, and H. Zhang, *Epitaxial growth of hybrid nanostructures,* Nature Reviews Materials **3** (2018), 10.1038/natrevmats.2017.89.

[50] P. Krogstrup, N. L. B. Ziino, W. Chang, S. M. Albrecht, M. H. Madsen, E. Johnson, J. Nygård, C. M. Marcus, and T. S. Jespersen, *Epitaxy of semiconductor–superconductor nanowires,* Nature Materials **14**, 400–406 (2015).

[51] A. Tosato, V. Levajac, J.-Y. Wang, C. J. Boor, F. Borsoi, M. Botifoll, C. N. Borja, S. Martí-Sánchez, J. Arbiol, A. Sammak, M. Veldhorst, and G. Scappucci, *Hard superconducting gap in germanium,* Communications Materials **4** (2023), 10.1038/s43246-023-00351-w.

[52] S. B. Bravyi and A. Y. Kitaev, *Fermionic quantum computation,* Annals of Physics **298**, 210–226 (2002).

[53] S. M. Frolov, M. J. Manfra, and J. D. Sau, *Topological superconductivity in hybrid devices,* Nature Physics **16**, 718–724 (2020).

[54] S. Vaitiekėnas, Y. Liu, P. Krogstrup, and C. M. Marcus, *Zero-bias peaks at zero magnetic field in ferromagnetic hybrid nanowires,* Nature Physics **17**, 43–47 (2020).

[55] B. W. Heinrich, J. I. Pascual, and K. J. Franke, *Single magnetic adsorbates on s -wave superconductors,* Progress in Surface Science **93**, 1–19 (2018).

[56] P. M. R. Brydon, S. Das Sarma, H.-Y. Hui, and J. D. Sau, *Topological yu-shiba-rusinov chain from spin-orbit coupling,* Physical Review B **91** (2015), 10.1103/physrevb.91.064505.

[57] F. Pientka, Y. Peng, L. Glazman, and F. v. Oppen, *Topological superconducting phase and majorana bound states in shiba chains,* Physica Scripta **T164**, 014008 (2015).

[58] L. Schneider, P. Beck, T. Posske, D. Crawford, E. Mascot, S. Rachel, R. Wiesendanger, and J. Wiebe, *Topological shiba bands in artificial spin chains on superconductors,* Nature Physics **17**, 943–948 (2021).

[59] B. van Heck, S. Mi, and A. R. Akhmerov, *Single fermion manipulation via superconducting phase differences in multiterminal josephson junctions*, Physical Review B **90** (2014), 10.1103/physrevb.90.155450.

2

BLOCH-LORENTZ MAGNETORESISTANCE OSCILLATIONS IN DELAFOSSITES

This chapter has been previously published as Kostas Vilkelis, Lin Wang, Anton Akhmerov *Bloch-Lorentz magnetoresistance oscillations in delafossites*, SciPost Phys. 15, 019 (2023).
Own contribution to work: I developed the theory, carried out the numerical simulations and analyzed the data with input from other authors. I wrote the manuscript together with other authors.

2

2.1. INTRODUCTION

Known since the discovery of mineral $CuFeO_2$ by Friedel in 1873, delafossites are materials with the general formula ABO_2 [1, 2]. Delafossites are naturally occurring layered structures of alternating conductive A layer and insulating BO_2 layer with the overall $R\bar{3}m$ space group [3]. These materials are considered to be 2D owing to their weak interlayer coupling which results in a nearly cylindrical Fermi surface [4, 5]. Of particular interest are $PdCoO_2$ and $PtCoO_2$ which were first synthesized and characterized at room temperature in 1971 by Shannon *et al.* [2, 3, 6]. Even though nearly 50 years have passed since then, the area of research is still very active due to the delafossites' impressive electronic transport properties [7]. At room temperature, it was shown that the conductivity of $PdCoO_2$ is 2.6 μΩ cm, very close to that of elemental copper [8]. Part of the reason for such large conductivity is the high Fermi velocity $7.5 \times 10^5\,\mathrm{m\,s^{-1}}$ [8]. Another reason is their exceptional mean-free path at 4 K which exceed 20 μm [8]. Such value of mean-free path is accredited mostly to anomalously clean nature of delafossites and orbital-momentum locking [9, 10]. Overall, all of these properties of delafossites make them a good platform to study mesoscopic ballistic transport [11].

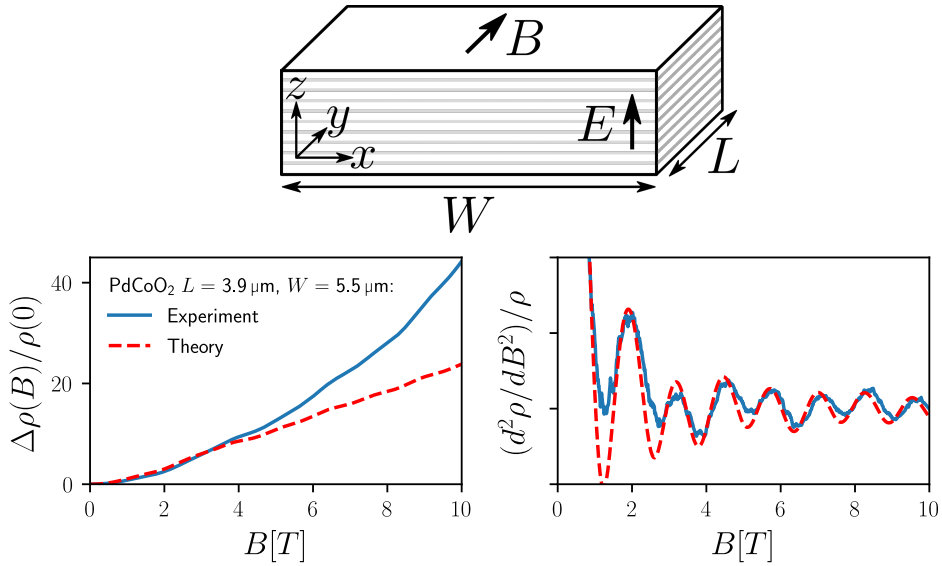

Figure 2.1: $PdCoO_2$ magnetoresistance experimental set up (top) and results (solid blue lines) obtained by Putzke *et al.* [12]. The semiclassical prediction (dashed red lines) was obtained by modeling the finite size $PdCoO_2$ sample.

Recent experiments studied the out-of-plane transport of $PdCoO_2$ [12], with the setup and the measured magnetoconductance shown in Fig. 2.1. Magnetoconductance was measured with the magnetic field applied in the plane of the delafossite layers and the current passing out-of-plane. Surprisingly, the magnetoconductance showed oscillations with a magnetic field similar to the Aharonov-Bohm effect, and therefore appearing to be of quantum origin. The period of the oscillations corresponded to adding a flux quantum

through the area Wc with $W \sim 5\,\mu$m the width of the sample and c the spacing between the adjacent conducting layers. Given that the oscillations persist up to elevated temperature of 50 K, this result is remarkable compared with *e. g.* quantum Hall interferometers, where coherence at micron length scale vanishes below 100 mK [13].

Simulations performed by Putzke *et al.* confirmed that the oscillations of Kubo conductivity with Aharonov-Bohm periodicity indeed appear in a minimal tight-binding model that combines high anisotropy with magnetic field [12]. Based on this observation, Ref. [12] attributed the oscillations to long-range coherence of the delafossite layers ($l_\phi \geq 10\,\mu$m) and separately ruled out multiple semiclassical or macroscopic origins of these oscillations. The manuscript therefore opens a question about the possible origins of this unusual long length and high temperature phase coherence. The coherent origins of the phenomenon also require closed trajectories, and are therefore hard to reconcile with boundary scattering at the strongly disordered sample boundaries[1].

Here, we argue that contrary to the claim of long range coherence, the oscillations are a consequence of the shape of the semiclassical trajectories rather than an interference pattern of electron waves traversing the sample. Our construction extends the idea put forward by Pippard [14] used to explain magnetoresistance oscillations in gallium [15]. Our formalism does not rely on sample-scale phase coherence and therefore is compatible with the low temperature phase coherence length l_ϕ =400 nm estimated from Shubnikov-de Haas [12] experiments. The semiclassical approach also allows us to incorporate the appropriate bulk and boundary scattering rates, and simulate the full 2D cross-section of the sample. The semiclassical approach also allows us to isolate the role of different scattering mechanisms and to conclude that in the clean samples, the sample aspect ratio is the most likely factor limiting the visibility of the oscillations.

2.2. BALLISTIC IN-PLANE MODEL IN THE WEAK OUT-OF-PLANE COUPLING LIMIT

Delafossites' conduction band is well approximated by the energy dispersion

$$\varepsilon(\mathbf{k}) = \varepsilon_\parallel(\mathbf{k}_\parallel) - t_z \cos(k_z c'), \tag{2.1}$$

where $\varepsilon_\parallel(\mathbf{k}_\parallel)$ is the in-plane dispersion relation with an approximately hexagonal Fermi surface [8, 16, 17], c' is the interlayer distance and t_z is the interlayer hopping. While interlayer dispersion is weak [4, 8]—$t_z \sim 10$ meV is much smaller than the in-plane bandwidth—it exceeds the thermal broadening of the Fermi surface at temperatures $T \lesssim 50$ K. This motivates a perturbative approach in terms of t_z that we use throughout the paper.

We compute electron density $f(\mathbf{r},\mathbf{k},t)d^3\mathbf{k}$ at position $\mathbf{r}$, time t and momentum $\mathbf{k}$ by using the Boltzmann equation. We separate electron density into the equilibrium part and non-equilibrium parts:

$$f(\mathbf{r},\mathbf{k}) = f^0 - g(\mathbf{r},\mathbf{k})\frac{\partial f^0}{\partial \varepsilon}, \tag{2.2}$$

[1] The samples in Ref. [12] were produced using focused ion beam lithography, and therefore have a few nm amorphous layer at the boundary

where the equilibrium density f^0 (Fermi-Dirac distribution) becomes at zero temperature a Heaviside function so that its derivative $\frac{\partial f^0}{\partial \varepsilon}$ becomes a Dirac delta function centered around the Fermi energy. The resulting steady-state linearised Boltzmann equation [18] reads:

$$\mathbf{v}\cdot\nabla_{\mathbf{r}}g-\frac{e}{\hbar}(\mathbf{v}\times\mathbf{B})\cdot\nabla_{\mathbf{k}}g-ev_z\mathscr{E}_z=\mathscr{L}g, \tag{2.3}$$

where $\mathbf{v}$ is the velocity, e is the elementary charge, $\hbar$ is the reduced Planck constant, $\mathbf{B}$ is the magnetic field, $\mathscr{E}_z$ is the electric field along the out-of-plane direction, and $\mathscr{L}g$ is the linearised collision integral. The boundary conditions at the boundary coordinate $\mathbf{r_B}$ are

$$\begin{gathered}|\mathbf{v}(\mathbf{k}_\parallel)\cdot\hat{\mathbf{n}}_\mathbf{B}|g(\mathbf{r_B},\mathbf{k})=\int\limits_{\mathbf{v}(\mathbf{k}'_\parallel)\cdot\hat{\mathbf{n}}_\mathbf{B}>0}K\left(\mathbf{k}',\mathbf{k}\right)\times\left|\mathbf{v}(\mathbf{k}_\parallel)\cdot\hat{\mathbf{n}}_\mathbf{B}\right|g(\mathbf{r_B},\mathbf{k}')d^3k',\\ \mathbf{v}(\mathbf{k}_\parallel)\cdot\hat{\mathbf{n}}_\mathbf{B}<0.\end{gathered} \tag{2.4}$$

where $\hat{\mathbf{n}}_\mathbf{B}$ is the unit normal vector of the boundary (pointing inwards) and K is the boundary scattering kernel.

Utilizing the smallness of t_z, we expand g in Eq. (2.3) as a series to first order in t_z:

$$g(\mathbf{r},\mathbf{k})\approx g_0(\mathbf{r},\mathbf{k})+g_1(\mathbf{r},\mathbf{k}), \tag{2.5}$$

where g_0 does not depend on t_z and $g_1\propto t_z$. With the magnetic field inside the yz-plane $\mathbf{B}=(0,B_y,B_z)$, the zeroth-order expansion is

$$\mathbf{v}_\parallel\cdot\frac{\partial g_0}{\partial\mathbf{r}_\parallel}-\frac{e}{\hbar}(\mathbf{v}_\parallel\times\mathbf{B})\cdot\nabla_{\mathbf{k}}g_0=\mathscr{L}g_0, \tag{2.6}$$

where $\mathbf{v}_\parallel$ is in-plane velocity. Equation (2.6) describes an electron in a magnetic field with no external forces capable of generating a steady non-equilibrium distribution. Under these conditions, non-zero scattering ensures that the steady state solution is $g_0=0$. Therefore, to first order in t_z linearised Boltzmann equation is

$$\mathbf{v}_\parallel\cdot\frac{\partial g}{\partial\mathbf{r}_\parallel}-\frac{e}{\hbar}\left(\mathbf{v}_\parallel\times\mathbf{B}\right)\cdot\nabla_{\mathbf{k}}g-ev_z\mathscr{E}_z=\mathscr{L}g. \tag{2.7}$$

Additionally, since $g\propto t_z$, it is sufficient to approximate $\mathscr{L}$ to zeroth order in t_z.

Integrating Eq. (2.7) over k_z within the 1st Brillouin zone, we obtain an equation identical to Eq. (2.6), but with g_0 replaced by $g_\parallel(\mathbf{r},\mathbf{k}_\parallel)\equiv\int_{\mathrm{BZ}}g(\mathbf{r},\mathbf{k})dk'_z$. Therefore, the in-plane current of electrons vanishes in the steady state:

$$\int\limits_{BZ}g(\mathbf{r},\mathbf{k})dk_z=0. \tag{2.8}$$

We assume that the disorder in the bulk and at the boundaries is weakly correlated across the layers. Therefore, the disorder rapidly randomizes out-of-plane momentum k_z and leads to k_z-independent K and $\mathscr{L}$. The weakly correlated disorder together with Eq. (2.8) simplifies the linearised collision integral:

$$\mathscr{L}g=-\frac{g(\mathbf{k}_\parallel,k_z)}{\tau(\mathbf{k}_\parallel)}, \tag{2.9}$$

where τ is the relaxation time which depends only on the in-plane wavevector $\mathbf{k}_\parallel$. Similarly, substitution of Eq. (2.8) in Eq. (2.4) and using the independence of K from k_z yields the simplified boundary conditions:

$$g(\mathbf{r_B}, \mathbf{k}_\parallel, \mathbf{k_z}) = 0, \text{for } \mathbf{v}(\mathbf{k}_\parallel) \cdot \hat{\mathbf{n}}_\mathbf{B} < 0. \tag{2.10}$$

Neither the scattering Eq. (2.9) nor boundary conditions Eq. (2.10) mix non-equilibrium electron densities along different trajectories defined by the semiclassical equations of motion

$$\hbar \frac{d\mathbf{r}(t)}{dt} = \nabla_\mathbf{k} \varepsilon(\mathbf{k}), \quad \hbar \frac{d\mathbf{k}(t)}{dt} = -e\mathbf{v}(t) \times \mathbf{B}, \tag{2.11}$$

where t is the time along the trajectory. Therefore, using Eq. (2.11), we obtain the evolution of g along a single trajectory:

$$\frac{\partial g(t, \mathbf{r_0}, \mathbf{k_0})}{\partial t} = \mathbf{v} \cdot \nabla_\mathbf{r} g - \frac{e}{\hbar} (\mathbf{v} \times \mathbf{B}) \cdot \nabla_\mathbf{k} g. \tag{2.12}$$

Here we parameterize each trajectory originating at a sample boundary through its initial coordinate and wave vector $\mathbf{r_0} = (x_0, y_0, z_0)$ and $\mathbf{k_0} = (k_0 \cos\theta_0, k_0 \sin\theta_0, k_{z,0})$. Substituting Eq. (2.12) and Eq. (2.9) into Eq. (2.7), we obtain the Boltzmann equation along a single trajectory

$$\frac{\partial g(t, \mathbf{r_0}, \mathbf{k_0})}{\partial t} - e\mathscr{E}_z v_z(k_z(t)) = -\frac{g(t, \mathbf{r_0}, \mathbf{k_0})}{\tau(\mathbf{k}_\parallel(t))}, \tag{2.13}$$

with solution

$$\begin{aligned} g(t, \mathbf{r_0}, \mathbf{k_0}) &= -e\mathscr{E}_z \int_0^t v_z\left(k_z(t')\right) \times \exp\left(-\frac{(t-t')}{\tau(\mathbf{k}_\parallel(t))}\right) dt' \\ &= -\frac{e\mathscr{E}_z t_z}{\hbar} \operatorname{Re}\left[\exp\left(ik_{z,0}\right) \int_0^t \exp\left(i\Delta k_z(t)\right) \times \exp\left(-\frac{(t-t')}{\tau(\mathbf{k}_\parallel(t))}\right) dt'\right], \end{aligned} \tag{2.14}$$

where $\Delta k_z(t)$ is the $k_z(t)$ solution to Eq. (2.11) with $k_z(0) = 0$ initial condition. Because $\Delta k_z(t)$ is fully determined by the in-plane trajectories, Eq. (2.14) shows that the excess electron distribution g is also fully determined by the in-plane trajectories.

To analyze experimental observations, we compute the current along z

$$I_{zz} = e \int_{S_\parallel} d^2\boldsymbol{r}_\parallel \iiint_{\mathrm{BZ}} f(\mathbf{r}, \mathbf{k}) v_z(\mathbf{k}) d\mathbf{k}, \tag{2.15}$$

where the triple integral is over the 1st Brillouin zone, and $S_\parallel$ is the in-plane surface area of the sample. We express the out-of-plane conductivity $\sigma_{zz} = I_{zz}/(S_\parallel \mathscr{E}_z)$ at zero temperature by substituting Eq. (2.2) into Eq. (6.6):

$$\sigma_{zz} = \frac{e}{S_\parallel \mathscr{E}_z} \int_{S_\parallel} d^2\boldsymbol{r}_\parallel \iiint_{\mathrm{BZ}} \delta(\varepsilon - \varepsilon_F) g(x, \mathbf{k}) v_z(\mathbf{k}) d\mathbf{k}, \tag{2.16}$$

where ε_F is the Fermi energy. In order to compute the lowest nonvanishing contribution in t_z to conductivity, we use $g_0 = 0$, and approximate the energy $\varepsilon(k_x, k_y, k_z) \approx \varepsilon_\parallel$ only to

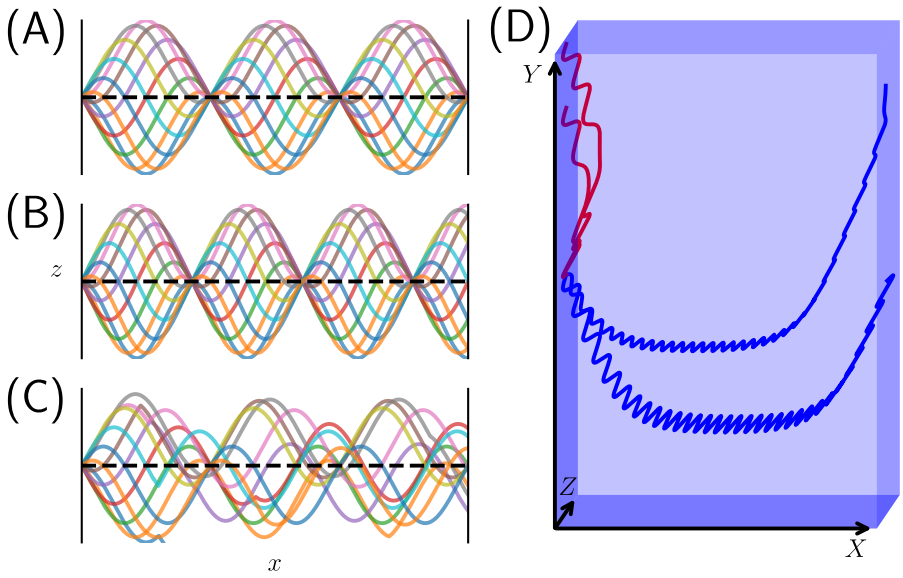

Figure 2.2: **(A)** Trajectories with oscillations commensurate to the sample width due to an in-plane magnetic field. Different curves indicate the different initial phases of the trajectory. **(B)** Same as in (A), but the in-plane magnetic field is chosen to give incommensurate oscillations. **(C)** Same as in (A), but with scattering present. **(D)** Trajectories due to an out-of-plane magnetic field. Blue lines are boundary-to-boundary trajectories whereas the red lines are edge-localized trajectories. Only the boundary-to-boundary trajectories produce current oscillations due to a net k_z drift throughout the trajectory.

zeroth order in t_z. We switch to cylindrical coordinates in k-space (x,k,θ,k_z) where k is the in-plane wavevector length and θ is the azimuth. The conductivity to the lowest order in t_z is

$$\sigma_{zz} = \frac{e}{S_\parallel \mathscr{E}_z \hbar} \int_{S_\parallel} \int_0^{2\pi} \int_{-\frac{\pi}{c'}}^{\frac{\pi}{c'}} \frac{k_F(\theta)}{v_R(\theta)} g(x, k_F(\theta), \theta, k_z) \times v_z(k_z) d^2\boldsymbol{r}_\parallel d\theta dk_z, \tag{2.17}$$

where

$$v_R(\theta) = \frac{1}{\hbar} \frac{\partial \varepsilon_\parallel}{\partial k}, \tag{2.18}$$

and $k_F(\theta)$ is the Fermi wavevector $\varepsilon(k_F(\theta),\theta) = \varepsilon_F$. We further simplify Eq. (2.17) by using that k_z enters Eq. (2.14) as a single complex exponent and carry out integration over k_z in a closed form.

2.3. RESULTS

2.3.1. LARGE ASPECT RATIO LIMIT

Because the mean free path of delafossites is larger than the sample size [12], to illustrate the origin of the oscillations we first neglect scattering $\mathscr{L} g = 0$. Furthermore, we assume

the sample has a large aspect ratio $L/W \to \infty$ and therefore we utilize translational invariance of the sample along the y-direction. With in-plane magnetic field $\mathbf{B} = (0, B_y, 0)$, the Boltzmann Eq. (2.7) reduces to

$$v_x \frac{\partial g(x, v_x, k_z)}{\partial x} - v_x \frac{eB_y}{\hbar} \frac{\partial g(x, v_x, k_z)}{\partial k_z} - e\mathscr{E}_z v_z = 0. \tag{2.19}$$

In this simple limit, $g(x, v_x, k_z)$ only depends on k_x and k_y through $v_x(k_x, k_y)$. Solution to Eq. (2.19) fulfilling the boundary conditions of Eq. (2.10) is

$$g(x, v_x, k_z) = \frac{-t_z \mathscr{E}_z}{B_y v_x} \left[\cos(k_z c') - \cos\left(k_z c' + \frac{\omega B_y}{W} x_B \right) \right], \tag{2.20}$$

with:

$$\omega = \frac{e}{\hbar} c' W, \quad x_B = \begin{cases} x & \text{for } v_x > 0 \\ x - W & \text{for } v_x < 0. \end{cases} \tag{2.21}$$

We substitute Eq. (2.20) into Eq. (2.17), and obtain the conductivity along z

$$\sigma_{zz} = \frac{e\pi t_z^2}{\omega \hbar B_y^2} \left(1 - \cos(\omega B_y)\right) \int_0^{2\pi} \frac{k_F(\theta)}{v_x(\theta) v_R(\theta)} d_\theta. \tag{2.22}$$

In other words, the conductivity has oscillations with an experimentally observed periodicity, but it vanishes in the minima so that the oscillations have a much larger amplitude.

To explain the large amplitude of the oscillations, we consider electron trajectories. When the magnetic field is of the form $\mathbf{B} = (0, B_y, B_z)$, the k_z dependence on x is

$$k_z(x) = k_{z0} + \frac{e}{\hbar} B_y x. \tag{2.23}$$

This ensures that all trajectories have a similar oscillatory vertical displacement as a function of x:

$$z(x) = \frac{t_z}{\hbar v_x} \left[\cos\left(k_{z0} + \frac{e}{\hbar} B_y x \right) - \cos(k_{z0}) \right]. \tag{2.24}$$

We plot the trajectories in Fig. 2.2(A, B). The universal trajectory shape is a result of the k_z advancing over the complete out-of-plane Brillouin zone, similar to Bloch oscillations [19], however, the origin of the momentum drift is Lorentz force instead of the electric field. This gives k_z a universal dependence on x regardless of the in-plane trajectory. When the oscillation period is commensurate with the sample width, all trajectories have a zero net vertical displacement over the time of flight, and therefore carry no current as shown in Fig. 2.2(A). At the same time, the vertical displacement of different trajectories—and therefore the current—is maximal when a half-integer number of oscillation periods fits into the sample width as shown in Fig. 2.2(B). Because the contribution of every trajectory to the conductance has the same magnetic field dependence, as seen in Eq. (2.22), this minimal model yields an oscillatory conductance with a correct frequency, but full visibility of the oscillations in contrast to the experimental data. We define the overall phenomenon as Bloch-Lorentz oscillations.

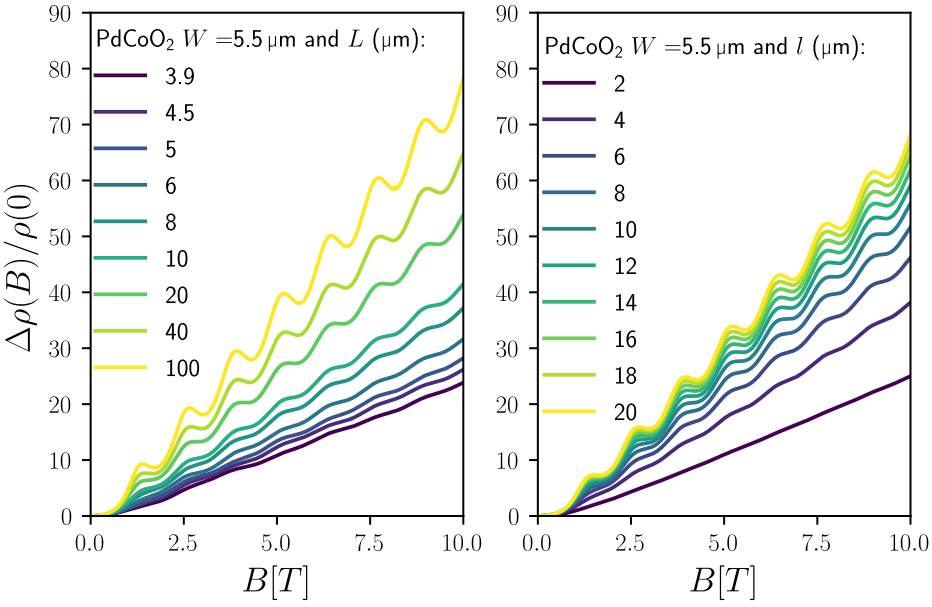

Figure 2.3: (Left panel) Semiclassical predictions of $PdCoO_2$ magnetoresistance with variable sample aspect ratio and no bulk scattering. (Right Panel) Semiclassical predictions of $PdCoO_2$ magnetoresistance sample with translational invariance along y and variable bulk scattering (mean-free-path l).

2.3.2. REALISTIC SAMPLE GEOMETRY

Bulk scattering cannot explain the disagreement between the experiment and the minimal model because the mean-free-path of 20 μm [8] is much larger than the dimensions of samples used by Putzke *et al.* [12] (4 μm to 6 μm). Therefore, the dominant source of scattering must originate from the boundaries. In the experimental setup by Putzke *et al.* [12], the sample has a low aspect ratio with a sample length shorter than the width $W > L$. As a result, we expect the boundaries along the length of the sample to alter the semiclassical trajectories.

To analyse the effects of small aspect ratio, we consider a rectangular geometry with boundaries at: $x = 0$, $x = W$, $y = 0$, $y = L$. We parameterize the trajectories by their point of origin at the boundary and the initial angle θ_0. At a sufficiently high out-of-plane magnetic field, bulk cyclotron orbits appear that do not intersect with sample boundaries. We disregard these trajectories because they do not contribute to the h/e magnetoresistance oscillations, however extending our approach to those trajectories is straightforward. By changing the variables in Eq. (2.17) to the trajectory coordinate

system (t,θ_0,k_{z0}), we bring σ_{zz} to the form

$$\sigma_{zz}=\frac{-e}{W\mathscr{E}_z\hbar}\oint dr_0\int_{\theta_{min}}^{\theta_{max}}d\theta_0\int_0^{t_B(\theta_0,\mathbf{r_0})}dt'\frac{k_F(\theta(\theta_0,t'))}{v_R(\theta(\theta_0,t'))}J(t',\theta_0)\times \int_{-\pi/c}^{\pi/c}dk_{z0}\,g(\mathbf{r_0},t',\theta_0,k_{z0})\,v_z(\mathbf{r_0},t',\theta_0,k_{z0}), \quad (2.25)$$

with the Jacobian determinant:

$$J(t',\theta_0)=\left(\frac{\partial\theta}{\partial t'}\Big|_{t'=0}\right)^{-1}\frac{\partial\theta}{\partial t'}v_x(0,\theta_0). \quad (2.26)$$

In Eq. (2.25), the r_0 integral is over the sample boundary and $t_B(\theta)$ is the time that the trajectory hits a boundary. The integral over θ_0 includes the contributions of all trajectories within the sample.

We solve Eq. (2.25) numerically with an in-plane magnetic field B_y and without bulk scattering $\tau\to\infty$. The results in Fig. 2.3 left panel shows the oscillations decaying with decreasing aspect ratio L/W of the sample. The visibility of the oscillations drops with a lower aspect ratio due to more trajectories scattering off the sample side-boundaries. Using the geometry of the sample of Ref. [12], we confirm that the computed relative magnitude of the oscillations agrees with the measured values, however, the overall resistance profile is somewhat different, as shown in Fig. 2.1. The possible reasons for this disagreement are residual bulk scattering, minor misalignment of the magnetic field, or inhomogeneity of the sample along the z-direction.

The scattering from the side-boundaries plays a similar role to bulk disorder. To demonstrate this, we apply the theory in the high aspect ratio limit in Eq. (2.19) to include bulk scattering through Eq. (2.9). The solution to the resulting linearised Boltzmann equation with relaxation is

$$g(x,\theta,k_z)=\frac{\mathscr{E}_z\tau ec' t_z}{\hbar\left(B_y^2\phi^2+1\right)}\Big(B_y\phi\cos\left(k_zc'\right)+\sin\left(k_zc'\right) -\exp\left(-\frac{x_B}{l}\right)\left[B_y\phi\cos\left(k_zc'+\frac{\omega B_y}{W}x_B\right)+\sin\left(k_zc'+\frac{\omega B_y}{W}x_\theta\right)\right]\Big), \quad (2.27)$$

with

$$l(\theta)=\tau v_x(\theta),\quad \phi(\theta)=\frac{e}{\hbar}c'l(\theta). \quad (2.28)$$

Here we assume that τ is constant along the Fermi surface. We substitute Eq. (2.27) into Eq. (2.17), and obtain conductivity per unit azimuth

$$\sigma_{zz}(B_y)=\frac{\tau e^2t_z^2c'\pi}{\hbar^2}\int_0^{2\pi}\frac{k_F(\theta)}{v_R(\theta)\left(B_y^2\phi^2+1\right)^2}\times\Big(1-r+(B_y\phi)^2r+(B_y\phi)^2+r\exp\left(-\frac{1}{r(\theta)}\right) \times\left[(1-B_y^2\phi^2)\cos(\omega B_y)-2B_y\phi\sin(\omega B_y)\right]\Big)d\theta,\quad r\equiv l(\theta)/W. \quad (2.29)$$

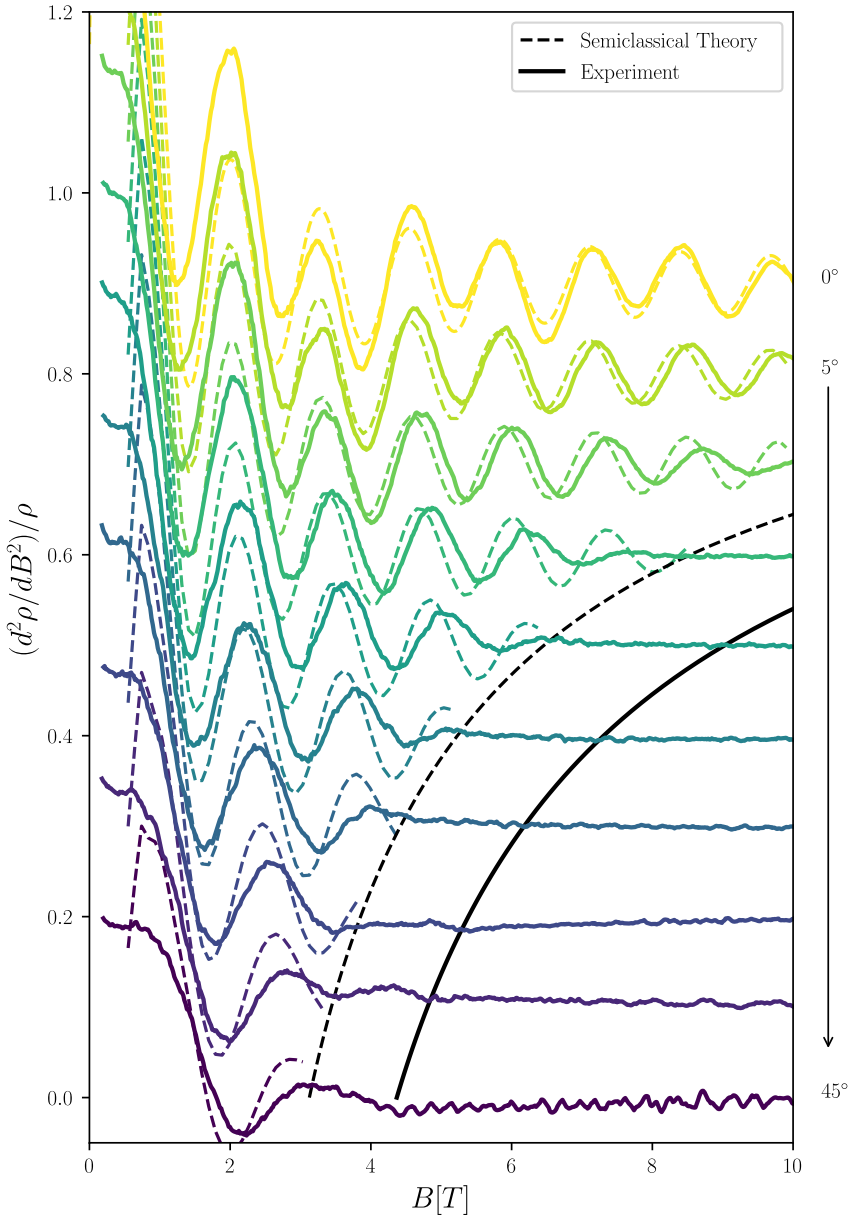

Figure 2.4: Numerical results from the semiclassical theory (dashed lines) with $l(0) = 4.4\mu m$ compared to the experimental (solid lines) magnetoresistance results by Putzke *et al.* [12] for magnetic field tilted out-of-plane by 5° steps. Black lines indicate the critical field when the cyclotron orbit fits inside the sample. The critical field value is determined by the shorter side of the sample. In the experiment, this is the length of the sample L, whereas in the semiclassical prediction it is the width of the sample W.

We recover a simple Drude model B^2 resistivity scaling [20] in Eq. (2.29) by removing the boundaries, $W \to \infty$, which removes the second term in Eq. (2.29). The results of Eq. (2.29) for various values of mean-free-path l are shown in the right panel of Fig. 2.3. We observe that the scattering of the side boundaries in a sample with a finite aspect ratio results in a similar magnetoresistance as bulk scattering. Moreover, our simulations show that the magnitude of the oscillations due to side boundary scattering in the geometry used in the experiment is comparable to the observed one (see Fig. 2.1). Based on this we conclude that the sample aspect ratio is the factor likely limiting the oscillation visibility in the experiment.

2.3.3. OUT-OF-PLANE MAGNETIC FIELD

In the presence of an out-of-plane magnetic field B_z, the in-plane projection of each trajectory is a rotated and rescaled hexagonal Fermi surface, while the out-of-plane motion follows the oscillatory pattern of Eq. (2.24) (see Fig. 2.2(D)). We use the integral form of the Boltzmann Eq. (2.25) to find the magnetoresistance response. To reduce the numerical cost required to evaluate a 4D integral of Eq. (2.25), we approximate the side boundary scattering by using a finite relaxation time τ instead. We expect that this approximation, while somewhat crude, should capture the essential physics, as supported by the comparison between the two mechanisms shown in Fig. 2.3. To evaluate the remaining 3D integral, we choose the starting point of each trajectory as $t = 0$, so that its initial conditions are $\mathbf{r_0} = (x_0, y_0, z_0)$ and $\mathbf{k_0} = (k_0 \cos\theta_0, k_0 \sin\theta_0, k_{z,0})$. Here $x_0 = 0$ and $-\pi/2 < \theta_0 < \pi/2$ at the left boundary, while $x_0 = W$ and $\pi/2 > \theta_0 > 3\pi/2$ at the right boundary.

In presence of the out-of-plane magnetic field, some trajectories cross from one boundary to the opposite, while others return to the boundary from which they originated, as shown in Fig. 2.2(D). Only the trajectories that cross the sample contribute to the conductance oscillations because they have a net k_z drift given by Eq. (2.23). On the other hand, the trajectories returning to the boundary where they originated do not contribute to the oscillations. As Putzke *et al.* [12] pointed out, once the cyclotron orbits become smaller than W, which happens at

$$B_z > \left(\frac{2\hbar k_F}{eW}\right), \tag{2.30}$$

with k_F the Fermi wavevector, ballistic trajectories crossing the sample disappear, and so do the conductance oscillations.

We perform numerical integration of Eq.(2.25), with the result shown in Fig. 2.4. The model qualitatively agrees with the experimental data at the small tilt angles from the xy-plane. However, the disagreement increases with B_z, likely due to our calculation approximating side boundary scattering with a constant relaxation time. This is likely a crude approximation because the sample length L is shorter than W in the experiment. The extension of the theory to a realistic sample geometry is straightforward—especially since one may still compute g for every trajectory independently—but it strongly increases the computational costs, and therefore we consider it unjustified for our study.

2.4. SUMMARY

In summary, we demonstrated that the observed magnetoresistance of delafossite materials is explained by the Bloch-like oscillations of the out-of-plane electron trajectories. These Bloch-Lorentz oscillations arise from the quasi-2D dispersion of these materials combined with the nearly ballistic motion of the electrons. We identify the sample aspect ratio as the most likely factor limiting the oscillation visibility. modelingling achieves a qualitative agreement with the experiment without introducing any free parameters.

ACKNOWLEDGEMENTS

We would like to thank Ady Stern, Veronika Sunko, and Maja Bachmann for the helpful discussions in the early stages of the project. Special thanks to Carlo Beenakker for his valuable feedback and advice on the manuscript. Also, we are grateful to Philip J.W. Moll and Carsten Putzke for sharing with us their experimental findings and subsequent consultations.

DATA AVAILABILITY

All code and data used in the manuscript are available at Ref. [21].

AUTHOR CONTRIBUTIONS

A.A. formulated the project idea. K.V. developed the theory, carried out numerical simulations, and analyzed the data with input from the other authors. The manuscript was written jointly by K.V. and A.A. with input from L.W.

FUNDING INFORMATION

This work was supported by the NWO VIDI Grant (016.Vidi.189.180), an ERC Starting Grant 638760, and European Union's Horizon 2020 research and innovation programme FE-TOpen Grant No. 828948 (AndQC).

REFERENCES

[1] C. Friedel, *Sur une combinaison naturelle des oxydes de fer et de cuivre, et sur la reproduction de l'atacamite,* Sciences Academy **77**, 211 (1873).

[2] R. D. Shannon, D. B. Rogers, and C. T. Prewitt, *Chemistry of noble metal oxides. i. syntheses and properties of abo2 delafossite compounds,* Inorganic Chemistry **10**, 713 (1971).

[3] R. D. Shannon, C. T. Prewitt, and D. B. Rogers, *Chemistry of noble metal oxides. ii. crystal structures of platinum cobalt dioxide, palladium cobalt dioxide, coppper iron dioxide, and silver iron dioxide,* Inorganic Chemistry **10**, 719 (1971).

[4] K. P. Ong, J. Zhang, J. S. Tse, and P. Wu, *Origin of anisotropy and metallic behavior in delafossite pdcoo$_2$*, Phys. Rev. B **81**, 115120 (2010).

[5] H.-J. Noh, J. Jeong, J. Jeong, E.-J. Cho, S. B. Kim, K. Kim, B. I. Min, and H.-D. Kim,

Anisotropic electric conductivity of delafossite $pdcoo_2$ *studied by angle-resolved photoemission spectroscopy,* Phys. Rev. Lett. **102**, 256404 (2009).

[6] R. D. Shannon, D. B. Rogers, C. T. Prewitt, and J. L. Gillson, *Chemistry of noble metal oxides. iii. electrical transport properties and crystal chemistry of abo2 compounds with the delafossite structure,* Inorganic Chemistry **10**, 723 (1971).

[7] A. P. Mackenzie, *The properties of ultrapure delafossite metals,* Reports on Progress in Physics **80**, 032501 (2017).

[8] C. W. Hicks, A. S. Gibbs, A. P. Mackenzie, H. Takatsu, Y. Maeno, and E. A. Yelland, *Quantum oscillations and high carrier mobility in the delafossitepdcoo2,* Physical Review Letters **109** (2012), 10.1103/physrevlett.109.116401.

[9] V. Sunko, P. McGuinness, C. Chang, E. Zhakina, S. Khim, C. Dreyer, M. Konczykowski, H. Borrmann, P. Moll, M. König, and et al., *Controlled introduction of defects to delafossite metals by electron irradiation,* Physical Review X **10** (2020), 10.1103/physrevx.10.021018.

[10] H. Usui, M. Ochi, S. Kitamura, T. Oka, D. Ogura, H. Rosner, M. W. Haverkort, V. Sunko, P. D. C. King, A. P. Mackenzie, and K. Kuroki, *Hidden kagome-lattice picture and origin of high conductivity in delafossite* $ptcoo_2$, Phys. Rev. Materials **3**, 045002 (2019).

[11] M. D. Bachmann, A. L. Sharpe, A. W. Barnard, C. Putzke, M. König, S. Khim, D. Goldhaber-Gordon, A. P. Mackenzie, and P. J. W. Moll, *Super-geometric electron focusing on the hexagonal fermi surface of pdcoo2,* Nature Communications **10** (2019), 10.1038/s41467-019-13020-9.

[12] C. Putzke, M. D. Bachmann, P. McGuinness, E. Zhakina, V. Sunko, M. Konczykowski, T. Oka, R. Moessner, A. Stern, M. König, S. Khim, A. P. Mackenzie, and P. J. Moll, *h/e oscillations in interlayer transport of delafossites,* Science **368**, 1234 (2020), https://www.science.org/doi/pdf/10.1126/science.aay8413 .

[13] P. Roulleau, F. Portier, P. Roche, A. Cavanna, G. Faini, U. Gennser, and D. Mailly, *Direct measurement of the coherence length of edge states in the integer quantum hall regime,* Phys. Rev. Lett. **100**, 126802 (2008).

[14] A. B. Pippard, *Magnetomorphic oscillations due to open orbits,* The Philosophical Magazine: A Journal of Theoretical Experimental and Applied Physics **13**, 1143 (1966), https://doi.org/10.1080/14786436608213529 .

[15] J. A. Munarin and J. A. Marcus, *New oscillatory magnetoresistance effect in gallium,* in *Low Temperature Physics LT9*, edited by J. G. Daunt, D. O. Edwards, F. J. Milford, and M. Yaqub (Springer US, Boston, MA, 1965) pp. 743–747.

[16] H. Takatsu, J. J. Ishikawa, S. Yonezawa, H. Yoshino, T. Shishidou, T. Oguchi, K. Murata, and Y. Maeno, *Extremely large magnetoresistance in the nonmagnetic metal* $pdcoo_2$, Phys. Rev. Lett. **111**, 056601 (2013).

[17] J. C. A. Prentice and A. I. Coldea, *Modeling the angle-dependent magnetoresistance oscillations of fermi surfaces with hexagonal symmetry,* Phys. Rev. B **93**, 245105 (2016).

[18] J. M. Ziman, *Principles of the Theory of Solids* (Cambridge University Press, 1972) p. 425.

[19] F. Bloch, *Über die quantenmechanik der elektronen in kristallgittern,* Zeitschrift für physik **52**, 555 (1929).

[20] S. Zhang, Q. Wu, Y. Liu, and O. V. Yazyev, *Magnetoresistance from fermi surface topology,* Phys. Rev. B **99**, 035142 (2019).

[21] K. Vilkelis and A. Akhmerov, *Bloch-Lorentz magnetoresistance oscillations in delafossites,* (2020), This work was supported by the NWO VIDI Grant (016.Vidi.189.180), an ERC Starting Grant 638760 and European Union's Horizon 2020 research and innovation programme FE-TOpen Grant No. 828948 (AndQC).

3

AHARONOV-BOHM MAGNETISM IN OPEN FERMI SURFACES

This chapter has been previously published as Kostas Vilkelis, Ady Stern, Anton Akhmerov *Aharonov-Bohm magnetism in open Fermi surfaces*, arXiv:2303.04310 (2023).
Own contribution to work: I developed the theory, carried out the numerical simulations and analyzed the data with input from other authors. I wrote the manuscript together with other authors.
Note: Upon completion of this work we learned about related references that analyze the same phenomenon without considering the effects of the 3D dispersion and disorder [1, 2]

3.1. INTRODUCTION

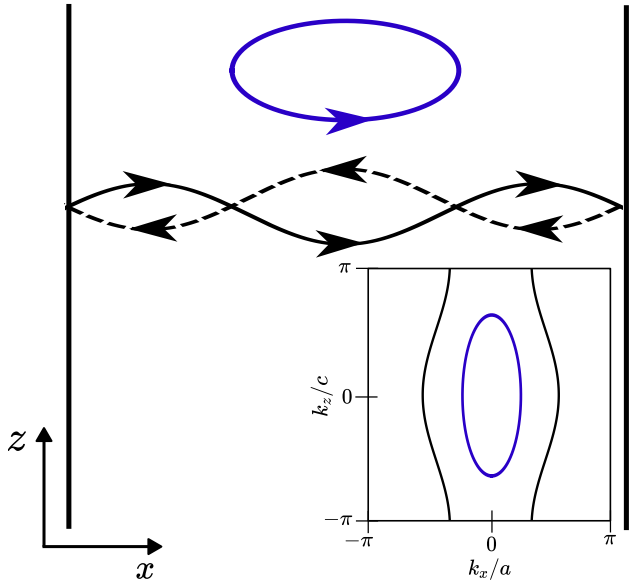

Figure 3.1: An example of closed (blue curve) and open (black curve) orbits. The right-moving (solid black line) and the left-moving (dashed black line) open trajectories are connected through boundary reflections. The inset at the bottom right shows the corresponding Fermi surface which is closed(open) for the blue(black) curve.

According to the classical theory by Langevin, diamagnetism is a result of the cyclotron motion of electrons in a magnetic field [3]. While this explanation provides an intuitive picture, it is incorrect due to the Bohr–van Leeuwen theorem [4, 5] that proves the absence of magnetic response in classical mechanics. On the other hand, a more modern interpretation by Liftshiftz-Kosevich [6] explains diamagnetism as a result of quantized closed orbits along the Fermi surface. The picture by Lifshitz-Kosevich is simple yet sufficient at explaining phenomena like de Haas-van Alphen (dHVA) diamagnetic oscillations [7] through the Fermi surface shape of metallic systems [8, 9].

Because ballistic orbits in the magnetic field are rotated and rescaled cuts of the Fermi surface, a Fermi surface that spans the whole Brillouin zone results in an open cyclotron orbit. An example of an open orbit is shown in Fig. 6.1 by the black curve. These orbits appear in metals such as copper [10] and gallium [11] or in highly anisotropic materials like delafossites [12]. The Liftshiftz-Kosevich theory [6] states that open orbits do not have a magnetic response. However, in multi-band materials with magnetic breakdown regions, it is possible to couple several open orbits into an effective closed orbit [13]. Such effective closed orbits have a magnetic response, but the contribution is exponentially small. On the other hand, open orbits in single-band materials do not close. As a result, the open orbits cannot be quantized and thus do not have a magnetic response according to the Bohr–van Leeuwen theorem [4, 5]. That raises the question of whether it is possible to observe quantum interference phenomena in open orbits without magnetic breakdown.

In this paper, we develop a theory of the orbital magnetic response of open orbits

in finite samples and predict magnetic oscillations alternating between diamagnetism and paramagnetism. These magnetic oscillations have the frequency of the Aharonov-Bohm effect [14] through the loop defined between the adjacent conducting atomic layers and the width of the sample. The effect is similar to h/e magnetoresistance oscillations observed in delafossites [15] and predicted in twisted bilayer graphene [16]. However, while the role of phase coherence in h/e magnetoresistance oscillations is uncertain, ballistic phase-coherent propagation is vital to the magnetic oscillations discussed in this paper. In addition, we find that these magnetic oscillations are sensitive to boundary quality such that diffusive boundaries destroy the effect. With these conditions fulfilled, we predict that this phenomenon has a strength comparable to Landau diamagnetism.

3.2. OPEN ORBIT QUANTIZATION VIA BOUNDARY REFLECTIONS

We begin by considering an open Fermi surface in layered materials with weak interlayer coupling, however, our theory equally applies to any other open Fermi surfaces. The dispersion of such a layered system is

$$\varepsilon(\kappa_x, k_z) = \varepsilon_\parallel(\kappa_x) + 2t_\perp \cos(k_z c), \tag{3.1}$$

where κ_x, k_z are the crystal momentum along x (in-plane) and z (out-of-plane) directions respectively, c is unit cell spacing along the z-direction, $t_\perp$ is the interlayer coupling and $\varepsilon_\parallel(k_\kappa)$ is the in-plane dispersion. Note we use an unconventional symbol κ_x for crystal momentum along the x-direction to distinguish it from the average crystal momentum k_x in a system with broken translational symmetry along x-direction which we will introduce shortly. For brevity, we omit the y-dimension here and will introduce it later on. We linearize the dependence of $\epsilon_\parallel$ on κ_x at energy E:

$$\begin{aligned} &\varepsilon_\parallel(\kappa_x) \approx E + \hbar v_x(E)\,[\kappa_x - k_x(E)] \\ &\varepsilon_\parallel(k_x) = E, \quad \hbar v_x(E) = \frac{\partial \varepsilon_\parallel(k_x(E))}{\partial k_x}, \end{aligned} \tag{3.2}$$

where $k_x(E)$ and $v_x(E)$ are momentum and and velocity along x-direction at energy E when $k_z = \pi/(2c)$, such that the out-of-plane energy is zero. Note that we require Eq. (3.1) to define an open Fermi surface at $\varepsilon = \mu$ along the k_z direction.

In the presence of an in-plane magnetic field, the semiclassical motion follows constant energy lines in momentum space and a real-space trajectory that is perpendicular to the momentum-space one. Without loss of generality, we consider the in-plane magnetic field along the y-direction $\mathbf{B} = (0, B, 0)$ and choose a vector potential $\mathbf{A} = (0, 0, -Bx)$ in the Landau gauge. For the open Fermi surface we consider, this implies periodic motion in the z-direction, but not in the x-direction along which the trajectory is open. To describe the trajectory in momentum space, we substitute [17] $k_z \to k_z - \frac{e}{\hbar} Bx$ into Eq. (3.1) and define local momentum along x at a fixed energy $\varepsilon(\kappa_x, k_z) = E$:

$$\kappa_x(E, k_z, x) = \pm \left[k_x(E) - \frac{2t_\perp}{\hbar v_x(E)} \cos\left(k_z c - \frac{e}{\hbar} cBx \right) \right] \tag{3.3}$$

where the trajectory is open whenever $k_x(E) > 2t_\perp/(\hbar v_x(E))$.

The allowed trajectories are those that fulfill by the Bohr-Sommerfeld quantization rule [18] given via WKB theory [19]:

$$S(E,k_z) \equiv \oint \kappa_x(E,k_z)\,dx = 2\pi n, \tag{3.4}$$

where $n \in \mathbb{Z}$ and we choose hard-wall boundaries such that there is no Maslov index. In the case of an open trajectory, the electron flips its direction of motion only when it scatters off a boundary. Therefore, we substitute Eq. (3.3) into Eq. (3.4) and consider particles specularly reflecting from the boundaries to obtain the open orbit quantization equation:

$$\begin{aligned} S(E,k_z) &\equiv 2k_x(E)W - \frac{2\Gamma(\phi)\cos(k_z c)}{\Delta E_x} = 2\pi n, \\ \Delta E_x(E) &\equiv \frac{\hbar v_x(E)}{W}, \quad \phi = \frac{e}{\hbar} cWB, \quad \Gamma = 2t_\perp \operatorname{sinc}(\phi/2), \end{aligned} \tag{3.5}$$

with ΔE_x the subband spacing due to confinement along x-direction, ϕ is the number of magnetic flux quanta (in units of 2π) passing through the loop of area cW.

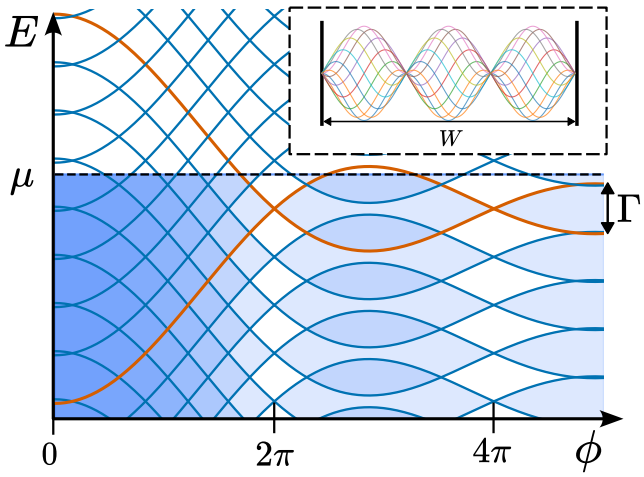

Figure 3.2: Plot of multiple displaced and overlapping k_z bands (blue curves) as a function of flux quanta ϕ passing through the system. The orange curve highlights one such band and its variation of bandwidth Γ with ϕ. The blue filling illustrates the occupation of bands below the chemical potential μ (dashed line), with the intensity indicating the number of overlapping bands at that point. As the bandwidth changes with respect to μ, the occupation of the bands changes which leads to a magnetic response. When an integer number of flux quanta pass through the system, different k_z trajectories are identical since they lead to the same energy as shown in the top right inset and therefore the bandwidth collapses.

We invert Eq. (3.5) and find the open orbit spectrum:

$$E_n = \varepsilon_\parallel\left(\frac{\pi n}{W}\right) + \Gamma\cos(k_z c), \tag{3.6}$$

where n is the index of the miniband that comes from the confinement along x-direction and Γ is the bandwidth as defined in Eq. (3.5). The bandwidth oscillates with the number

of flux quanta ϕ threading a rectangle of size Wc. The oscillations decay in a way similar to Fraunhofer diffraction, and their periodicity is that of the Aharonov-Bohm effect, as shown in Fig. 4.2. When the number of flux quanta is an integer, the bandwidth Γ collapses to zero so that the different k_z channels decouple. In the opposite limit, we see that if we take $B = 0$ in Eq. (3.6), we recover the original dispersion given by Eq. (3.1).

3.3. DIAMAGNETIC RESPONSE OF AN OPEN FERMI SURFACE

To find the total magnetisation of the system, we reintroduce the y-dimension. We start with a zero-temperature case and consider finite temperature later. The magnetisation of occupied states at fixed k_y is:

$$M(\mu, k_y) = \frac{d}{dB}\int_{-\infty}^{\mu} E\rho(E, k_y)dE, \tag{3.7}$$

where $\rho(E, k_y)$ is the density of states at energy E and wavevector k_y. We express the density of states ρ through the action of a trajectory in Eq. (3.5), similar to the work by Doron and Smilansky [20]:

$$\rho(E, k_y) = -\frac{1}{W\pi^2}\int_{-\pi/c}^{\pi/c} dk_z \frac{d}{dE}\mathrm{Im}\ln\left(1 - e^{iS(E+i0^+)}\right), \tag{3.8}$$

with Im the imaginary part. To regularise the oscillatory integrand along energy E given by Eq. (3.8), we perform analytic continuation of Eq. (3.7) into the complex energy $E + i\mathscr{E}$ (see supplementary). The analytic continuation converts the oscillatory terms into exponentially decaying functions away from $\mathscr{E} = 0$ and fixes the convergence of the integral in Eq. (3.7). That allows us to linearise the dispersion in Eq. (3.2) around the Fermi level μ and compute the magnetisation at k_y:

$$\begin{aligned} M(k_y, \mu) &= \frac{1}{Wc\pi}\frac{d\Gamma}{dB}\sum_{n=1}^{\infty}\frac{\sin(2nk_F W)}{n}J_1\left(\frac{2n\Gamma}{\Delta E_x}\right), \\ k_F(k_y) &= k_x(\mu, k_y), \quad \Delta E_x(k_y) = \frac{\hbar v_F(k_y)}{W}, \\ v_F(k_y) &= v_x(E, k_y), \end{aligned} \tag{3.9}$$

where J_1 is a Bessel function of the first kind and k_F and v_F are the Fermi momentum and Fermi velocity. For $k_y = 0$, Eq. (3.9) is the magnetisation of a 2D system with an open Fermi surface.

Equation (3.9) depends in an oscillatory way on the flux ϕ and chemical potential μ. The flux dependence has two characteristic frequencies. The first is the dependence similar to the Aharonov-Bohm effect of Γ on the flux ϕ. The second is from the $\Gamma/\Delta E_x$ term that originates from commensuration of the energy separation ΔE_x between minibands with the bandwidth Γ. Lastly, the chemical oscillatory dependence comes from $k_F W$ that originates from the position of the chemical potential with respect to the center of a k_z band. The sum over n represents the different Fourier components of the oscillations with respect to the chemical potential μ.

In 3D, the total magnetisation per unit volume is:

$$\mathcal{M}(\mu) = \frac{1}{\pi}\int_{FS} M(k_y,\mu)\,dk_y, \tag{3.10}$$

where the integral over k_y is along the Fermi surface. We utilize the steepest-descent method to evaluate the leading order contributions to this integral originating from its behavior near the maxima of $k_F(k_y)$. To do so, we define the maxima of the Fermi wavevector along x as K_F and compute the corresponding Fermi surface curvature:

$$\begin{aligned} K_F = k_F(k_{y,0}), \quad \frac{dk_F(k_{y,0})}{dk_y} = 0, \\ k_{y,\text{eff}} = \left(\frac{d^2k_F(k_{y,0})}{d^2k_y}\right)^{-1} = \left(\frac{\partial^2\varepsilon_\parallel}{\partial k_y^2}\frac{\partial k_F}{\partial\varepsilon_\parallel}\right)^{-1} = \frac{m_y V_F}{\hbar}, \end{aligned} \tag{3.11}$$

where m_y is the effective mass along the y-direction, $V_F = v_F(k_{y,0})$ is the Fermi velocity at K_F and $k_{y,\text{eff}}$ is related to the Fermi surface curvature and defines the effective Fermi y-momentum below which all the trajectories point predominantly along the x-direction. We substitute Eq. (3.11) into Eq. (3.10), deform the integration contour along the steepest descent and obtain total magnetisation:

$$\begin{aligned} \mathcal{M}(\mu) &= \mathcal{M}_0 \frac{d\,\text{sinc}(\phi/2)}{d\phi}\sum_{n=1}^{\infty}\frac{\sin(2nK_FW)}{n^{3/2}}J_1\left(\frac{2n\Gamma}{\Delta E_x}\right), \\ \mathcal{M}_0 &= \frac{2et_\perp}{W\hbar\pi^{3/2}}\sqrt{k_{y,\text{eff}}W} \end{aligned} \tag{3.12}$$

The magnetisation in Eq. (3.12) is a complex oscillatory function of the Fermi wavevector and the magnetic field B. To simplify the expression, we consider thermal broadening of the order of miniband spacing, $k_BT \approx \Delta E_x$, which suppresses the terms with $n > 1$ (see the supplementary material for details).

$$\begin{aligned} \mathcal{M}(\mu, k_BT \approx \Delta E_x) \approx \\ \mathcal{M}_0 \frac{d\,\text{sinc}(\phi/2)}{d\phi}\sin(2K_FW)J_1\left(\frac{2\Gamma}{\Delta E_x}\right). \end{aligned} \tag{3.13}$$

In Eq. (3.13), there are two distinct regimes: the single-band limit, where $t_\perp/\Delta E_x \ll 1$ and the many-band limit, where $t_\perp/\Delta E_x \gg 1$.

In the single-band limit $t_\perp/\Delta E_x \ll 1$, we expand the Bessel function J_1 in Eq. (3.13) for small arguments and find a simplified form of magnetisation:

$$\begin{aligned} \mathcal{M}(\mu, k_BT \approx \Delta E_x) \approx \\ -\frac{2\mathcal{M}_0}{\phi^3}\frac{t_\perp}{\Delta E_x}\sin(2K_FW)\left(2-\phi\sin\phi-2\cos\phi\right). \end{aligned} \tag{3.14}$$

The magnetisation in Eq. (3.14) oscillates with ϕ, the number of flux quanta passing through an area cW similar to the Aharonov-Bohm effect, however, the oscillations decay

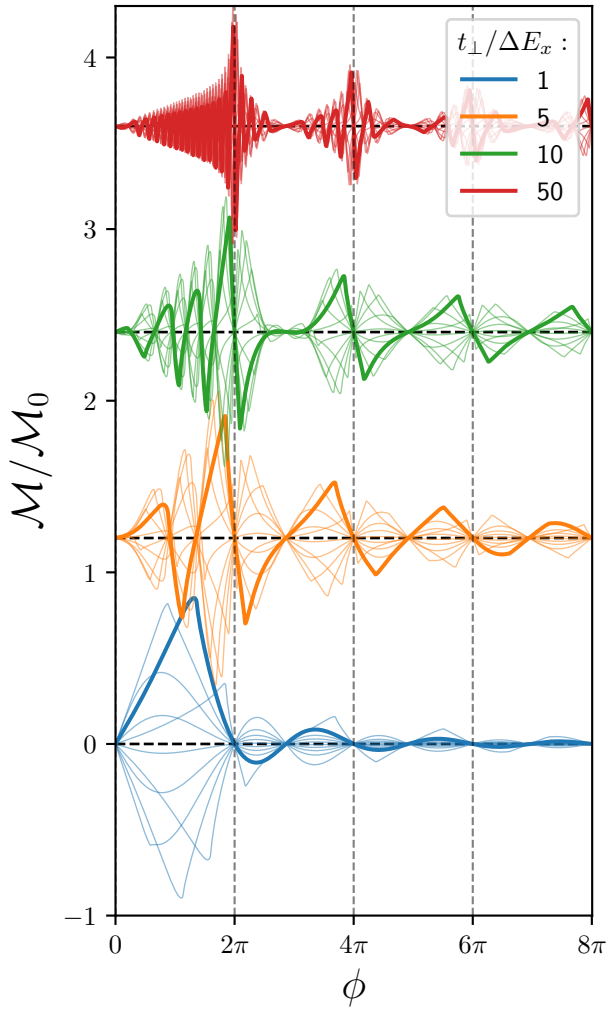

Figure 3.3: The magnetisation as a function of magnetic flux quanta passing through the system for different $t_\perp/\Delta E_x$ ratios. The main (thick) curves are evaluated at $K_F W = \pi/8$ whereas the thin secondary (thin) curves are evaluated at other $K_F W$ values.

with ϕ^2. Figure 4.2 provides a qualitative explanation of this behavior as a response of a partially occupied band with bandwidth that both oscillates and decays with ϕ. These oscillations are distinct from the dHVA diamagnetism [7] that oscillates with inverse magnetic field $1/B$ because the cyclotron orbit shrinks with a magnetic field. Due to their similarity with the Aharonov-Bohm effect, we name the magnetisation oscillations of open Fermi surfaces Aharonov-Bohm magnetism.

In the many-band limit $t_\perp/\Delta E_x \gg 1$, Eq. (3.13) exhibits a combination of multiple

frequency oscillations combined with an overall decay, as shown in Fig 4.3. However, Aharonov-Bohm magnetism is still evident in this regime because regardless of the chemical potential, the amplitude of the magnetization oscillations reaches its maximum whenever an integer number of flux quanta passes through the area cW.

3.4. PRACTICAL CONSIDERATIONS

Under the ideal conditions which include ballistic phase-coherent transport with specular boundaries and the absence of thermal broadening, the $\mathscr{M}_0$ term controls the overall magnetization magnitude of the phenomenon as shown in Fig 4.3. Therefore we see in Eq. (3.12) that Aharonov-Bohm magnetism favors small sample widths W, large interlayer hopping $t_\perp$, and flat in-plane Fermi surfaces with large $k_{y,\text{eff}}$. In a typical delafossite sample, we find the magnetisation from Aharonov-Bohm magnetism to be $\mathscr{M}_0 \approx 1\,\text{A}\,\text{m}^{-1}$ which is an order of magnitude weaker than Landau diamagnetism (see supplementary).

If we move away from the ideal conditions, we find that the Bohr-Sommerfeld quantization condition in Eq. (3.4) relies on specular boundary reflections at the ends of the sample to close the trajectory. To examine the role of diffusive boundary scattering, we numerically calculate the magnetisation in finite samples with variable boundary reflectivity r. We observe that the amplitude of the magnetisation is proportional to r^2, consistent with the idea that closed trajectories require two specular reflections in order to close. Furthermore, we remark that random bulk scattering and dephasing must work in the same way as diffusive boundary reflection: the probability to encounter a random scattering/dephasing event in a $2W$ width sample with mean-free path/phase coherence length $l_{0/\phi}$ is $exp(-2W/l_{0/\phi})$. Therefore, the strength of Aharonov-Bohm magnetism depends on both mean-free-path and boundary quality:

$$\mathscr{M} \propto r^2 \left[1 - \exp\left(-\frac{l_{0/\phi}}{2W}\right)\right]. \tag{3.15}$$

Finally, we summarize the necessary conditions required to observe Aharonov-Bohm magnetism:

1. Open component to the Fermi surface.
2. Phase coherence length and mean-free path larger than the sample width, $W \leq l_\phi, l_0$.
3. High-quality sample boundaries to ensure specular reflections.

One candidate family of materials that fulfill conditions 1. and 2. are the delafossites [21] like $PdCoO_2$ and $PtCoO_2$. Delafossites are highly anisotropic materials with a cylindrical Fermi surface [12] and mean-free path on the order of 20 µm [22]. Additionally, the hexagonal Fermi surface in delafossites allows one to align a sample in a way that does not permit trajectories along the magnetic field direction and thus maximizes $k_{y,\text{eff}}$. An alternative candidate material is elemental copper [10]. Despite not having a fully open Fermi surface, it does have small open components. Even though that reduces the number of possible open trajectories (and thus $k_{y,\text{eff}}$), the out-of-plane mass $m_\perp$ in copper is smaller and thus more favourable than in delafossites. Additionally, it is possible

to engineer copper samples with a mean-free path well into the micrometre scale [23]. However, in both cases, the sample boundaries pose a significant bottleneck which should be overcome for the effect to be observed.

3.A. DIAMAGNETIC RESPONSE DERIVATION

3.A.1. 2D RESULT

We substitute the density of states in Eq. (3.8) into the definition of magnetisation in Eq. (3.7):

$$\begin{aligned} M(k_y,\mu) = &-\frac{\mathrm{Im}}{W\pi^2}\frac{d}{dB}\int_{-\infty}^{\mu}\int_{-\pi}^{\pi} dE dk_z E \frac{d}{dE}\ln\left(1-e^{iS(E+i0^+)}\right) = \\ &-\frac{1}{W\pi^2}\int_{-\pi/c}^{\pi/c} dk_z \mathrm{Im}\frac{d}{dB}\left(\mu\ln\left(1-e^{iS(\mu)}\right)-\int_{-\infty}^{\mu}\ln\left(1-e^{iS(E)}\right)dE\right), \end{aligned} \tag{3.16}$$

where we use integration by parts to split the integral into two. The first part of the integral simplifies to:

$$\mathrm{Im}\frac{d}{dB}\left(\ln\left(1-e^{iS(\mu)}\right)\right) = -\mathrm{Im}\left(\frac{ie^{iS(E)}}{1-e^{iS(E)}}\frac{dS(E)}{dB}\right) = -\mathrm{Im}\left(i\frac{1-e^{-iS(E)}}{2-2\cos(S)}\frac{dS(E)}{dB}\right) = \frac{1}{2}\frac{dS(E)}{dB}. \tag{3.17}$$

From Eq. (3.5), we see that the Eq. (3.17) will average out to zero in an integral over k_z and therefore will not contribute to the magnetisation. As a result, we focus our attention on the second term in Eq. (3.16)

$$M(k_y,\mu) = -\frac{1}{W\pi^2}\int_{-\pi/c}^{\pi/c} dk_z \mathrm{Im}\int_{-\infty}^{\mu} dE \frac{ie^{iS(E)}}{1-e^{iS(E)}}\frac{dS(E)}{dB} \tag{3.18}$$

To complete the integral over E in Eq. (3.18), we employ analytic continuation and extend the energy into the complex plane $E+i\mathscr{E}$. We use the following integration contour as shown in Fig. 3.4:

I. $E\to-\infty$ and $\mathscr{E}\in(0,+\infty)$.

II. $E\in(-\infty,\mu)$ and $\mathscr{E}\to+\infty$

III. $E=\mu$ and $\mathscr{E}\in(+\infty,0)$.

One can check through Eq. (3.5) that integral contours I and II do not contribute because $\lim_{E\to-\infty}e^{iS(E)}=0$ and $\lim_{\mathscr{E}\to\infty}e^{iS(E)}=0$. To proceed with the remaining integral III, we work with open trajectories which arise when $k_x > 2t_\perp/(\hbar v_x)$. We argue that this relation breaks only when the trajectories are aligned with the magnetic field direction and therefore should not contribute to the magnetisation. We express action in terms of linearised momentum as we did in Eq. (3.5), but now include a first order $\mathscr{E}$ term:

$$S(\mu+i\mathscr{E},k_y,k_z) = 2k_F W + i\frac{\mathscr{E}}{\Delta E_x} - \frac{2\Gamma\cos\left(\phi/2+k_z c\right)}{\Delta E_x}, \tag{3.19}$$

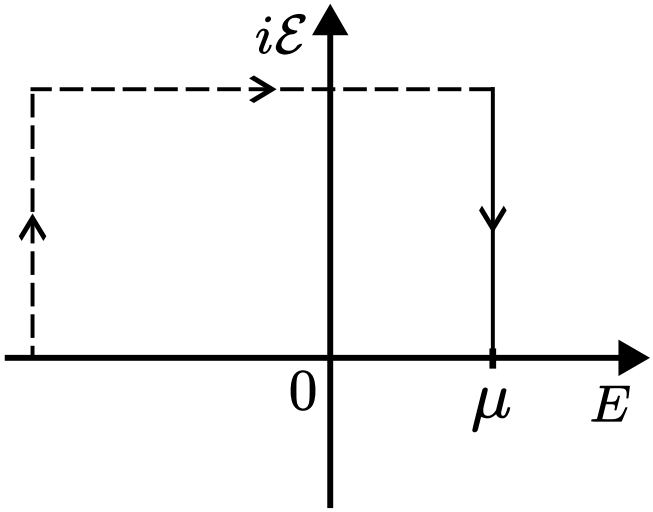

Figure 3.4: Integration contour along real energy deformed into the complex plane through analytical continuation. The dashed parts of the contour are chosen sufficiently far away such that they do not contribute to the overall integral and the only contribution comes from the solid vertical contour line.

where we define $k_F = k_x(k_y, \mu)$ and $\Delta E_x = \Delta E_x(\mu, k_y)$ and exclude the explicit dependence on k_y and μ in the equations for brevity. Higher order $\mathscr{E}$ terms are neglected due to the exponential decay $e^{-\mathscr{E}/\Delta E_x}$ of the ingrand. We substitute Eq. (3.19) into the integral Eq. (3.18) along contour III:

$$\begin{aligned} M(k_y,\mu) = \frac{\Delta E_x}{W\pi^2}\int_{-\pi/c}^{\pi/c} dk_z \mathrm{Im}\int_0^\infty d\mathscr{E}\frac{ie^{-\frac{\mathscr{E}}{\Delta E_x}+iS(\mu)}}{1-e^{-\frac{\mathscr{E}}{\Delta E_x}+iS(\mu)}}\frac{dS(\mu)}{dB} = \\ -\frac{\Delta E_x}{W\pi^2}\mathrm{Im}\int_{-\pi/c+\phi/2}^{\pi/c+\phi/2} dk_z\, i\ln\left(1-e^{iS(\mu)}\right)\frac{dS(\mu)}{dB}, \end{aligned} \tag{3.20}$$

$$\frac{dS}{dB} = \frac{ecW}{\hbar\Delta E_x}\left[\Gamma\sin(k_z c) - \frac{d\Gamma}{d\phi}\cos(k_z c)\right]. \tag{3.21}$$

We expand the natural logarithm ln in Eq. (3.18) in a power series:

$$\ln\left(1-e^{iS}\right)\frac{dS}{dB} = \sum_{p=1}^{\infty}\frac{e^{iSp}}{p}\frac{dS}{dB}, \tag{3.22}$$

and utilize the Jacobi-Anger expansion on the exponential term in Eq. (3.22):

$$e^{inS} = e^{i2nk_F W}\left[J_0\left(\frac{2n\Gamma}{\Delta E_x}\right) + 2\sum_{q=1}^{\infty} i^q J_q\left(-\frac{2n\Gamma}{\Delta E_x}\right)\cos\left(qk_z c\right)\right], \tag{3.23}$$

where J_q are the Bessel functions of the first kind. Due to the orthogonality between trigonometric function in Eq. (3.21) and Eq. (3.23), the integration in Eq. (3.20) will only leave the $q = 1$ term remaining:

$$M(k_y,\mu) = \frac{1}{Wc\pi}\frac{d\Gamma}{dB}\sum_{n=1}^{\infty}\frac{\sin(2nk_FW)}{n}J_1\left(\frac{2n\Gamma}{\Delta E_x}\right). \tag{3.24}$$

3.B. EFFECT OF TEMPERATURE

Equation (3.10) is a result at zero temperature. The addition of temperature can simplify the form of magnetisation by removing the higher frequency $n > 1$ components. To achieve this, we write $\mathscr{M}$ at non-zero temperature:

$$\mathscr{M}(\mu,T) = \int_{-\infty}^{\infty}\mathscr{M}(E,T=0)\frac{dF(E-\mu,T)}{dE}dE = \left(\mathscr{M}\circledast\frac{dF}{dE}\right)(\mu) = \mathscr{F}^{-1}\left\{\mathscr{F}\{\mathscr{M}\}\cdot\mathscr{F}\left\{\frac{dF}{dE}\right\}\right\}, \tag{3.25}$$

where $F(E-\mu,T)$ is the Fermi-Dirac distribution. In the last part of the equation, we utilize the convolution theorem to express magnetisation as a product of Fourier components of zero temperature magnetisation and Fermi-Dirac distribution. The Fourier Transform of a Fermi-Dirac distribution is [24]:

$$\mathscr{F}\{F\}(s) = \frac{1}{\sqrt{2\pi}}\int_{-\infty}^{\infty}F(E)e^{-isE}dE = \sqrt{\frac{\pi}{2}}\delta(s) + \frac{1}{\sqrt{2\pi}}\left(\frac{\sinh(s\pi k_BT)}{i\pi k_BT}\right)^{-1}. \tag{3.26}$$

On the other hand, to find the Fourier transform, we work with the linearised momentum:

$$k_x(E) = K_F + \frac{1}{\Delta E_x W}(E-\mu), \tag{3.27}$$

where we drop the k_y index since $k_x(E)$ is evaluated at the extrema. The zero temperature magnetisation at energy E close to Fermi level μ reads:

$$\mathscr{M}(E) = \mathscr{M}_0\frac{d\,\mathrm{sinc}(\phi/2)}{d\phi}\sum_{n=1}^{\infty}\frac{\sin\left(2nWK_F + \frac{n(E-\mu)}{\Delta E_x}\right)}{n^{3/2}}J_1\left(\frac{2\Gamma}{\Delta E_x}\right), \tag{3.28}$$

where only the sin term was substituted in by Eq. (3.27) and other terms are kept constant K_F as a result of a steepest-descent approximation. The approximation is valid as long as $\mu \gg k_BT$. Therefore, the Eq. (3.26) becomes:

$$\mathscr{M}(\mu) = \mathscr{M}_0\frac{d\,\mathrm{sinc}(\phi/2)}{d\phi}\sum_{n=1}^{\infty}\left(\frac{\sinh(\frac{n\pi k_BT}{\Delta E_x})}{\frac{(n\pi k_BT)}{\Delta E_x}}\right)^{-1}\frac{\sin(2nWK_F)}{n^{3/2}}J_1\left(\frac{2n\Gamma}{\Delta E_x}\right). \tag{3.29}$$

Whenever the thermal temperature is comparable to or larger than the energy spacing, $k_BT \approx \Delta E_x$, the Eq. (3.29) reduces to a single component:

$$\mathscr{M}(\mu) \approx \mathscr{M}_0\frac{d\,\mathrm{sinc}(\phi/2)}{d\phi}\sin(2K_FW)J_1\left(\frac{2\Gamma}{\Delta E_x}\right). \tag{3.30}$$

3.C. MAGNETIC SUSCEPTIBILITY MAGNITUDE

In order to estimate the magnitude of the magnetic susceptibility χ, we expand the magnetisation in Eq. (3.13) to first order in flux ϕ:

$$\chi = \mu_0 \frac{d\mathcal{M}}{dB} \approx -\mu_0 \frac{\mathcal{M}_0}{12} \frac{d\phi}{dB} \sin(2K_F W) J_1\left(\frac{4t_\perp}{\Delta E_x}\right), \tag{3.31}$$

where μ_0 is the vacuum permeability. To compare we consider Landau diamagnetism [25] of an isotropic dispersion with mass $m_\parallel$ and Fermi wavevector K_F:

$$\chi_L = -\mu_0 \frac{e^2 K_F}{12\pi^2 m_\parallel}. \tag{3.32}$$

The ratio between Aharonov-Bohm magnetism in Eq. (3.31) and Landau diamagnetism in Eq.(3.32) is:

$$\frac{\max(\chi)}{\chi_L} \approx \sqrt{k_{y,\text{eff}} W}\,(cK_F)^{-1} \left(\frac{m_\parallel}{m_\perp}\right) J_1\left(\frac{4t_\perp}{\Delta E_x}\right) \tag{3.33}$$

where we substituted $t_\perp = \hbar^2/(2m_\perp c^2)$ where $m_\perp$ is the mass along the z direction and $m_\parallel$ ($m_y = m_x = m_\parallel$) is the mass along the in-plane direction. Note that in Eq. (3.33) we consider $\sin(2K_F W) = 1$ and thermal broadening on the order of miniband spacing $k_B T \approx \Delta E_x$ to simplify the estimate. We see from Eq. (3.33) that Aharonov-Bohm magnetism favors large mass anisotropy $m_\parallel/m_\perp$ and flat in-plane Fermi surfaces that maximize $k_{y,\text{eff}}$. Furthermore, the thermal broadening of highly oscillatory terms in the many-band regime decreases the magnitude of the effect through the J_1 term.

As a check, we estimate the magnitude of the effect in typical delafossites samples[21] with Fermi momentum $K_F = 1.0\text{Å}^{-1}$, Fermi velocity $V_F = 1\,\text{m}\mu\text{s}^{-1}$ sample width $W = 1.0\,\mu\text{m}$, inter-layer lattice spacing $c = 1\text{Å}$, inter-layer hopping $t_\perp = 10\,\text{meV}$ and mass anisotropy $m_\parallel/m_\perp = 10^{-2}$. We further estimate $\sqrt{k_{y,\text{eff}} W} \approx 10^2$, miniband spacing $\Delta E_x = 1\,\text{meV}$ and $J_1 = 0.1$. As a result, we predict Aharonov-Bohm magnetism to be at least an order of magnitude weaker than Landau diamagnetism $\max(\chi)/\chi_L \approx 0.1$.

REFERENCES

[1] M. Y. Azbel', *Aharonov-bohm–de haas–van alphen supermagnetization,* Physical Review Letters **82**, 422–425 (1999).

[2] M. Y. Azbel', O. V. Kirichenko, and V. G. Peschanskii, *On the quantum magnetic size oscillation effects in organic conductors,* Low Temperature Physics **26**, 594–597 (2000).

[3] P. Langevin, *Sur la théorie du magnétisme,* J. Phys. Theor. Appl. **4**, 678 (1905).

[4] B. Savoie, *A rigorous proof of the bohr–van leeuwen theorem in the semiclassical limit,* Rev. Math. Phys. **27**, 1550019 (2015).

[5] N. Bohr, *The doctor's dissertation (text and translation),* (Elsevier, 1972) pp. 163–393.

[6] I. Lifshitz and A. Kosevich, *Theory of magnetic susceptibility in metals at low temperatures,* Sov. Phys. JETP **2**, 636 (1956).

[7] D. Haas and W. J. Van Alphen, *The dependence of the susceptibility of diamagnetic metals upon the field,* Proc. Netherlands Roy. Acad. Sci **33** (1930).

[8] D. Shoenberg, *The fermi surfaces of copper, silver and gold. i. the de haas-van alphen effect,* Philosophical Transactions of the Royal Society of London. Series A, Mathematical and Physical Sciences **255**, 85 (1962).

[9] D. Shoenberg and P. J. Stiles, *The de haas van alphen effect in alkali metals,* Proceedings of the Royal Society of London. Series A. Mathematical and Physical Sciences **281**, 62 (1964).

[10] D. Roaf, *The fermi surfaces of copper, silver and gold. ii. calculation of the fermi surfaces,* Philosophical Transactions of the Royal Society of London. Series A, Mathematical and Physical Sciences **255**, 135 (1962).

[11] W. A. Reed and J. A. Marcus, *Topology of the fermi surface of gallium,* Phys. Rev. **126**, 1298 (1962).

[12] K. Kim, H. C. Choi, and B. I. Min, *Fermi surface and surface electronic structure of delafossite PdCoO2,* Phys. Rev. B **80**, 035116 (2009).

[13] M. Kaganov and A. Slutskin, *Coherent magnetic breakdown,* Physics Reports **98**, 189 (1983).

[14] Y. Aharonov and D. Bohm, *Significance of electromagnetic potentials in the quantum theory,* Phys. Rev. **115**, 485 (1959).

[15] C. Putzke, M. D. Bachmann, P. McGuinness, E. Zhakina, V. Sunko, M. Konczykowski, T. Oka, R. Moessner, A. Stern, M. König, S. Khim, A. P. Mackenzie, and P. J. Moll, *h/e oscillations in interlayer transport of delafossites,* Science **368**, 1234 (2020).

[16] T. Vakhtel, D. O. Oriekhov, and C. W. J. Beenakker, *Bloch oscillations in the magnetoconductance of twisted bilayer graphene,* Phys. Rev. B **105**, L241408 (2022).

[17] R. Peierls, *Zur theorie des diamagnetismus von leitungselektronen,* Zeitschrift für Physik **80**, 763 (1933).

[18] A. Alexandradinata and L. Glazman, *Semiclassical theory of landau levels and magnetic breakdown in topological metals,* Phys. Rev. B **97**, 144422 (2018).

[19] C. M. Bender, S. Orszag, and S. A. Orszag, *Advanced mathematical methods for scientists and engineers I: Asymptotic methods and perturbation theory*, Vol. 1 (Springer Science and Business Media, 1999).

[20] E. Doron and U. Smilansky, *Chaotic spectroscopy,* Chaos: An Interdisciplinary Journal of Nonlinear Science **2**, 117 (1992).

[21] A. P. Mackenzie, *The properties of ultrapure delafossite metals,* Rep. Prog. Phys. **80**, 032501 (2017).

[22] C. W. Hicks, A. S. Gibbs, A. P. Mackenzie, H. Takatsu, Y. Maeno, and E. A. Yelland, *Quantum oscillations and high carrier mobility in the delafossite PdCoO2,* Phys. Rev. Lett. **109**, 116401 (2012).

[23] B. C. Deaton and J. D. Gavenda, *Electron relaxation time anisotropy in copper,* Phys. Rev. **129**, 1990 (1963).

[24] C. Belardinelli, *Generalized fourier transforms applied to fractional derivatives and quantum statistics distributions,* (2019).

[25] L. Landau, *Diamagnetismus der metalle,* Zeitschrift für Physik **64**, 629 (1930).

4

FERMIONIC QUANTUM COMPUTATION WITH COOPER PAIR SPLITTERS

This chapter has been previously published as Kostas Vilkelis, Antonio Manesco, Juan Daniel Torres Luna, Sebastian Miles, Michael Wimmer, Anton Akhmerov *Fermionic quantum computation with Cooper pair splitters*, arXiv:2309.00447 (2023)
Own contribution to work: I was supervising the project, and participated in developing all the aspects of the theory and numerical calculations. I wrote the manuscript together with all the co-authors.

4.1. INTRODUCTION

Over the years, qubits emerged as the de facto basis for quantum computation with a plethora of host platforms: superconducting circuits [1, 2], trapped ions [3, 4] and quantum dots [5], to name a few. Recent works used qubit-based quantum computers to simulate fermionic systems [6–8]. However, the mapping from qubits to local fermionic modes (LFMs) is inefficient because it introduces additional overhead to the calculations [9, 10]. For example, a map from n qubits to fermions requires $O(n)$ additional operations through the Jordan-Wigner transformation [11] and $O(\log n)$ through the Bravyi-Kitaev transformation [12].

An alternative to avoid the overhead in the qubit to LFM map is to use a quantum computer that already operates with local fermionic modes [12]. Moreover, the advantage of local fermionic modes is not limited to the simulation of fermionic systems. A set of $2n$ local fermionic modes maps directly to n parity-preserving qubits, which corresponds to $n-1$ qubits. Therefore, the map from local fermionic modes to qubits only requires a constant number of operations regardless of the system size and is, therefore, more efficient than the reverse [12]. Recently, Ref. [13, 14] showed that local fermionic modes offer advantages in quantum optimization problems of finding the ground state energy of fermionic Hamiltonians.

Motivated by this advantage of local fermionic modes over qubits, we propose an experimental implementation of a quantum computer with local fermionic modes. Our device is inspired by recently reported Cooper pair splitters [15–20], and our design includes an additional tunable capacitance to control Coulomb interactions. We show that the device implements the necessary universal set of gates proposed by Bravyi and Kitaev [12]. We also discuss the limitations of the device.

4.2. DESIGN

Bravyi and Kitaev [12] showed that fermionic quantum computation is equivalent to parity-preserving qubit operations. As a consequence, given a set of fermionic creation ($c_i^\dagger$) and annihilation operators (c_i), it follows that

$$\left\{ \begin{array}{ll} \mathcal{U}_1(\alpha) = \exp\left(i\alpha c_i^\dagger c_i\right), & \mathcal{U}_2(\beta) = \exp\left[i\beta\left(c_i^\dagger c_j + c_j^\dagger c_i\right)\right], \\ \mathcal{U}_3(\gamma) = \exp\left[i\gamma\left(c_i^\dagger c_j^\dagger + c_j c_i\right)\right], & \mathcal{U}_4(\delta) = \exp\left(i\delta c_i^\dagger c_i c_j^\dagger c_j\right) \end{array} \right\} \tag{4.1}$$

with $\alpha = \beta = \gamma = \pi/4$, and $\delta = \pi$, is a universal set of gate operators. The case of two LFMs is similar to two uncoupled qubits: each operation within a given fermion parity sector is a rotation within SU(2). In the odd fermion parity sector, the operations $\mathcal{U}_1(\alpha)$ and $\mathcal{U}_2(\beta)$ are rotations around perpendicular axes in the Bloch sphere. Likewise $\mathcal{U}_3(\gamma)$ and $\mathcal{U}_1(\delta)$ are perpendicular rotations within the even fermion parity sector. In the presence of an extra ancilla LFM, applying $\mathcal{U}_4$ entangles the even and odd subspaces of the two computational LFMs.

We thus propose a device where excitations occupy single-orbital sites, numbered by the subindex i and j. A practical platform for such a proposal is an array of spin-polarized quantum dots, as the scheme shown in Fig. 6.1. Within this platform, the unitary operations in Eq. 4.1 are a time-evolution of the following processes:

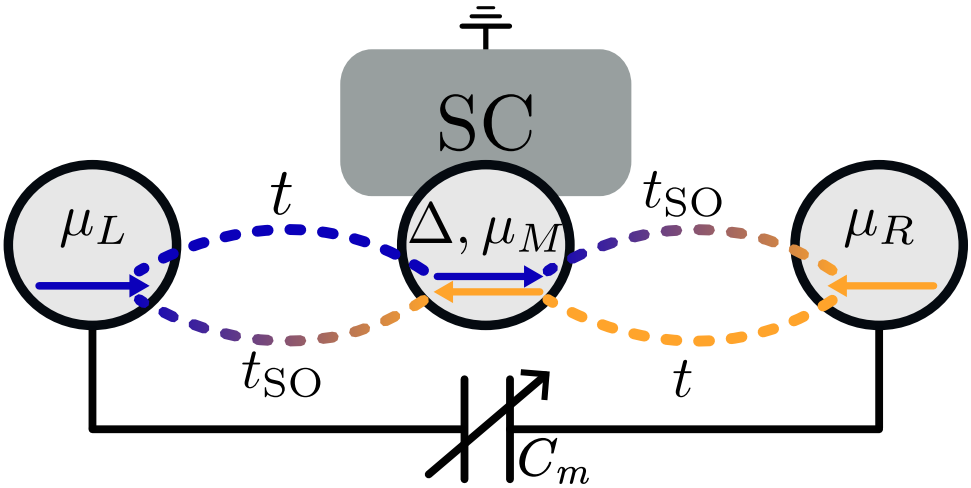

Figure 4.1: The unit cell of a fermionic quantum computer. Two singly-occupied spin-(anti)polarized quantum dots host the local fermionic modes L and R. Two tunnel barriers enable normal t and spin-dependent t_{SO} tunnelings between the two dots. A middle superconducting island mediates superconducting correlations between the two local fermionic modes. An external mutual capacitor C_m allows Coulomb interactions between the sites.

1. $c_i^\dagger c_i$ onsite energy shift of the fermionic state at site i;
2. $c_i^\dagger c_j$ hopping of a fermion between sites i and j;
3. $c_i^\dagger c_j^\dagger$ superconducting pairing between fermions at sites i and j;
4. $c_i^\dagger c_i c_j^\dagger c_j$ Coulomb interaction between fermions at sites i and j.

We control the onsite energies μ_i with plunger gates. Similarly, a tunnel gate between neighboring pairs of quantum dots controls hopping strength t between them. Manipulation with plunger and tunnel gates is a well-established technique in charge [21, 22] and spin [5] qubits.

To implement the superconducting coupling between the spin-polarized dots, we utilize the design of a triplet Copper pair splitter [16–20]. We include an auxiliary quantum dot in proximity to an s-wave superconductor mediating crossed Andreev reflection (CAR) and elastic cotunelling (ECT) between the two quantum dots that encode the LFMs. Thus, the ECT rate Γ sets the hopping strength between the two dots, whereas the CAR rate Λ sets the effective superconducting pairing. Because the dots are spin-polarised, the superconducting pairing must be of spin-triplet, enabled by spin-orbit hopping in the hosting material. We quantify the spin-orbit coupling in the hosting material by the spin precession angle between the dots $\theta_i = 2\pi d/l_{so}$, where d is the interdot distance and l_{so} is the spin-orbit length. The spin-orbit coupling in InSb wires leads to a spin-precession length $l_{\mathrm{so}} \approx 100\,\mathrm{nm}$ [23, 24] resulting on non-negligible θ_i within the order of dot-to-dot distance.

Finally, we achieve Coulomb interaction between a pair of dots through capacitive coupling C_m. Our design requires a variable capacitive coupling to implement the $\mathscr{U}_4$ gate. Several recent works demonstrate variable capacitive coupling in various platforms: gate-tunable two-dimensional electron gas [25], varactor diodes [26], and external double quantum dots [27].

We show the unit cell of a fermionic quantum computer with two LFMs in Fig. 6.1. The basic building block consists of three tunnel-coupled quantum dots in a material with large spin-orbit coupling. The middle dot is proximitized by an s-wave superconductor with an induced gap Δ that mediates CAR and ECT between the outer dots. The spin-polarised outer dots (L,R) encode the LFMs, whereas the middle one is an auxiliary component. Finally, a tunable capacitor couples the outer dots. We generalize the device to an arbitrary number of LFMs by repeating the unit cell in a chain. To read out the fermionic state, we propose to measure the occupation in each quantum dot through charge sensing [28].

4.3. EFFECTIVE HAMILTONIAN

4.3.1. TUNNEL COUPLING

In the absence of capacitive and tunnel coupling, the approximate Hamiltonian for the two spin-polarised dots is

$$H_d = \sum_{i=L,R} \mu_i c^\dagger_{i\sigma_i} c_{i\sigma_i} \,, \tag{4.2}$$

where $c_{i\sigma}$ is the electron anihilation operator at site i and spin σ, and μ_i is the corresponding chemical potential. The Hamiltonian in Eq. (4.2) is valid if the charging energy and Zeeman splitting on each dot are larger than all other energy scales in the problem. Recent experiments on similar devices measure charging energy of 2 meV and Zeeman splitting of 400 µeV at 200 mT [16, 17, 19, 20]. Both charging energy and Zeeman splitting are larger than the usual induced superconducting gap inside the quantum dot $\Delta \sim 100\,\mu$eV [20, 29, 30], justifying the approximation in Eq. (4.2).

The proximity of the middle dot to the superconductor suppresses its g-factor [31]. Thus, differently from the outer dots, we consider a finite Zeeman energy B. The Hamiltonian of the middle dot is

$$H_{\text{ABS}} = \sum_{\sigma,\sigma'} \left[\mu_M(\sigma_0)_{\sigma\sigma'} + B(\sigma_z)_{\sigma\sigma'}\right] c^\dagger_{M\sigma} c_{M\sigma'} + \Delta c^\dagger_{M\uparrow} c^\dagger_{M\downarrow} + \text{h.c.} \tag{4.3}$$

where $c^\dagger_{M\sigma}$ is the creation operator of electron on the middle dot with spin σ, Δ is the induced superconducting gap, and σ_l are the Pauli matrices ($l = \{0,x,y,z\}$) acting on the spin subspace. Both spin-polarised dots in Eq. (4.2) connect to the middle dot by symmetric tunnel barriers with strength t. The barrier t controls both normal and spin-orbit tunneling processes:

$$H_t = t \sum_{i=L,R} \cos\theta_i c^\dagger_{i\sigma_i} c_{M\sigma} + it \sum_{i=L,R} \sum_{\sigma'} (\sigma_y)_{\sigma_i\sigma'} \sin\theta_i c^\dagger_{i\sigma_i} c_{M\sigma'} + \text{h.c.}\,, \tag{4.4}$$

where θ_i is the spin precession angle from dot i to the middle island. Thus, the total Hamiltonian is

$$H = H_d + H_{\text{ABS}} + H_t \,. \tag{4.5}$$

We obtain the effective low-energy Hamiltonian in the weak-coupling limit, $t \ll \Delta$, through a Schrieffer-Wolf (the derivation is in Appendix 4.A) [32, 33]:

$$\tilde{H} = \sum_i \epsilon_i^{\sigma_i\sigma_j} c_{i\sigma_i}^\dagger c_{i\sigma_i} + \sum_{i,j} \Gamma_{\sigma_i\sigma_j} c_{i\sigma_i}^\dagger c_{j\sigma_j} + \Lambda_{\sigma_i\sigma_j} c_{i\sigma_i}^\dagger c_{j\sigma_j}^\dagger + \text{h.c.}\,, \tag{4.6}$$

where $\epsilon_i^{\sigma_i\sigma_j}$ is the renormalised onsite energy of dot i, $\Gamma_{\sigma_i\sigma_j}$ is the ECT rate and $\Lambda_{\sigma_i\sigma_j}$ is the CAR rate. While $t \neq 0$, we do not vary the chemical potential of the outer dots, $\mu_L = \mu_R = 0$. For simplicity, we also assume no Zeeman splitting within the middle dot $B = 0$ and that the spin precession angles are symmetric $\theta_L = \theta_R = \theta$ (see Appendix 4.A for more general form). In such case, the effective parameters for the anti-parallel spin configuration are:

$$\Lambda_{\uparrow\downarrow} = \kappa\Delta\cos(2\theta)\,, \quad \Gamma_{\uparrow\downarrow} = -i\kappa\mu_M \sin(2\theta)\,, \tag{4.7}$$

and for the parallel channel:

$$\Lambda_{\uparrow\uparrow} = -i\kappa\Delta\sin(2\theta)\,, \quad \Gamma_{\uparrow\uparrow} = -\kappa\mu_M\cos(2\theta)\,, \tag{4.8}$$

where

$$\kappa = t^2/(\Delta^2 + \mu_M^2 - B^2)\,. \tag{4.9}$$

Both onsite corrections terms are equal:

$$\epsilon_L^{\sigma_i\sigma_j} = \epsilon_R^{\sigma_i\sigma_j} = \kappa\mu_M. \tag{4.10}$$

We observe that the magnitude of $\Lambda_{\sigma_i\sigma_j}$ is maximum at $\mu_M = 0$ and drops with increasing chemical potential μ_M. On the other hand, $\Gamma_{\sigma_i\sigma_j}$ has maxima at finite μ_M. The magnitude of both processes depends on the spin-precession angle θ and spin configuration of the outer dots as shown in Fig. 4.2 (a) and (b). To ensure that operation times for $\mathscr{U}_2$ and $\mathscr{U}_3$ are similar, the convenient regime is where $\max\Gamma_{\sigma_i\sigma_j} \sim \max\Lambda_{\sigma_i\sigma_j}$.

4.3.2. CAPACITIVE COUPLING

The electrostatic energy between the two dots is [34]:

$$H_C = \sum_{i=L,R} v_i c_{i\sigma_i}^\dagger c_{i\sigma_i} + U_m c_{L\sigma_L}^\dagger c_{L\sigma_L} c_{R\sigma_R}^\dagger c_{R\sigma_R}\,, \tag{4.11}$$

where $U_m = C_m e^2/\tilde{C}$ is the mutual interaction between the two dots,

$$v_{L/R} = \frac{C_{R/L}(2n_{g,L/R}+1) + C_m n_{g,R/L}}{2\tilde{C}} \tag{4.12}$$

is the renormalization to the onsite energy, $\tilde{C} = C_L C_R - C_m^2$, C_L and C_R are the capacitances of the left and right dots, C_m is the mutual capacitance, and $n_{g,i}$ is the charge offset in the site i. Notice that we consider singly-occupied dots in (4.11). This approximation is valid when $U_m \ll \Delta \ll e^2 C_{L/R}/\tilde{C}$ because the charging energy renormalization due to the mutual capacitance is negligible in this regime. The last term in (4.11) gives the Coulomb interaction between the dots required to implement $\mathscr{U}_4$.

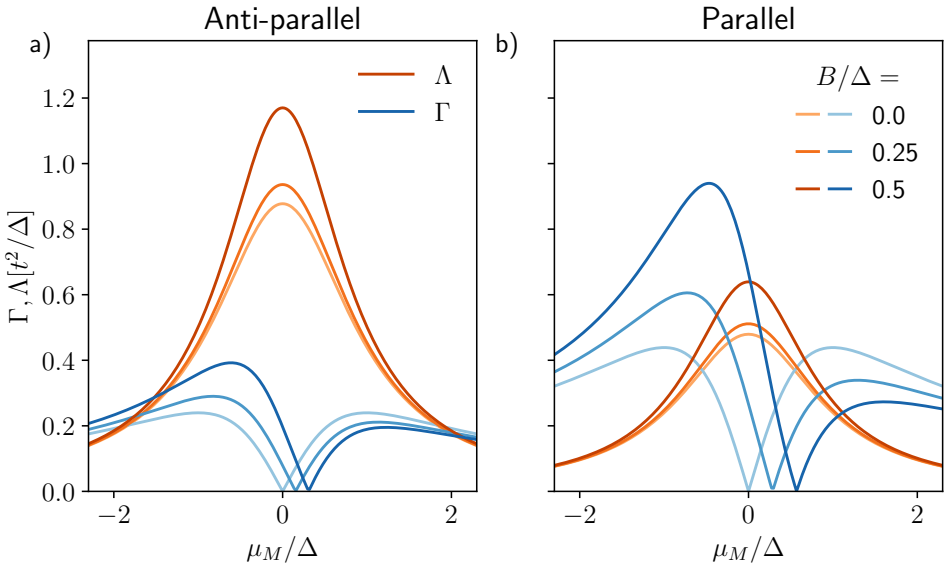

Figure 4.2: Absolute value of Λ (blue) and Γ (orange) as a function of μ_M for different values of B for the anti-parallel configuration (a) and the parallel configuration (b). System parameters are $t = 0.15$, $\theta_L = 0.7$ and $\theta_R = 0.3$.

4.4. FERMIONIC QUANTUM GATES

4.4.1. UNITARY GATE OPERATIONS

To achieve the fermionic quantum operations defined in Eq. (4.1), we need to engineer specific time-dependent profiles for the tunable system parameters. In this case, we control the following system parameters through Eqs. (4.11) and (4.6): left and right plunger gates (μ_L, μ_R), middle plunger gate (μ_M), tunnel gates (t, we treat the two tunnel gates together), and mutual capacitance (C_m). For simplicity, we only consider square pulses in time

$$H(\tau) = H_P(S)[\Theta(\tau) - \Theta(\tau - \tau_P)] \tag{4.13}$$

where $\Theta(\tau)$ is the Heaviside step function, τ is time and τ_P is the duration of the pulse. We define the pulse Hamiltonian $H_P(S)$ as a constant total Hamiltonian where $S = \{t, \mu_M, ...\}$ are non-zero system parameters in the pulse. For example, $H_P(\{t\})$ is a constant Hamiltonian with all system parameters zero except the tunnel coupling t. We set the idle (reference) Hamiltonian to one where all gates are zero, $t = \mu_L = \mu_R = \mu_M = U = 0$. Thus, the time-evolution operator simplifies to

$$\mathcal{U}(\tau_2, \tau_1) = \exp\left[-\frac{i}{\hbar}\int_{\tau_1}^{\tau_2} d\tau'\, H(\tau')\right] = \exp\left[-\frac{i}{\hbar} H_P(S)\tau_P\right]. \tag{4.14}$$

where τ_2, τ_1 are the initial and final times, and τ_P is the duration of the pulse. In practice, the transition between the idle Hamiltonian and H_P in Eq. (4.13) is not instantaneous but ramps up smoothly over a time τ_R to minimize non-adiabatic transitions.

We engineer the unitary operations as an ordered sequence of pulses defined in Eq. (4.14). For simplicity, we assume no Zeeman splitting in the middle dot, $B = 0$, and leave the discussion of the more general case to section 4.4.2. In this case, the minimal pulse sequence scheme which implements the gates in Eq. (4.1) is:

1. onsite operation:

$$\mathscr{U}_1 = \exp\left[-\frac{i}{\hbar} H_P\left(\{\mu_L, \mu_R\}\right)\tau_P\right]; \tag{4.15}$$

2. hopping operation:

$$\begin{aligned}\mathscr{U}_2 = &\exp\left[-\frac{i}{\hbar} H_P\left(\{\mu_L = \mu, \mu_R = \mu\}\right)\tau_P^{(4)}\right] \times \exp\left[-\frac{i}{\hbar} H_P\left(\{t\}\right)\tau_P^{(3)}\right] \\ &\times \exp\left[-\frac{i}{\hbar} H_P\left(\{\mu_L = \mu, \mu_R = \mu\}\right)\tau_P^{(2)}\right] \times \exp\left[-\frac{i}{\hbar} H_P\left(\{t, \mu_M\}\right)\tau_P^{(1)}\right]\end{aligned} \tag{4.16}$$

3. superconducting pairing operation:

$$\mathscr{U}_3 = \exp\left[-\frac{i}{\hbar} H_P\left(\{t\}\right)\tau_P\right]; \tag{4.17}$$

4. Coulomb interaction operation:

$$\mathscr{U}_4 = \exp\left[-\frac{i}{\hbar} H_P\left(\{\mu_L, \mu_R\}\right)\tau_P^{(2)}\right] \times \exp\left[-\frac{i}{\hbar} H_P\left(\{U\}\right)\tau_P^{(1)}\right]; \tag{4.18}$$

where we indicate as $\tau_P^{(i)}$ the duration of the i-th pulse.

In the above scheme, the operations $\mathscr{U}_1$ and $\mathscr{U}_3$ require a single pulse. The gate $\mathscr{U}_1$ requires a single pulse because the dots are uncoupled from one another and the plunger gates affect the onsite energies without inducing any sort of coupling between the dots. Similarly, $\mathscr{U}_3$ is also a single operation because the CAR rate is maximum at $\mu_M = 0$ whereas both ECT rate and onsite corrections are zero according to Eqs. (4.7— 4.10). We show the time-dependent simulation of the $\mathscr{U}_3$ gate in Fig. 4.3.

On the other hand, the first pulse of Eq. (4.16) introduces finite onsite corrections to the outer dots and CAR according to Eqs. (4.7— 4.10). Since the onsite corrections are equal, only a global phase factor is accumulated within the odd fermion parity sector. On the other hand, both onsite corrections and CAR result in undesired rotations within the even fermion parity subspace. We undo these operations with an Euler rotation using two orthogonal operations, resulting in the three subsequent pulses in Eq. (4.16). Similarly, the Coulomb operation in Eq. (4.18) also requires a correction puls with the plunger gates because the mutual capacitance C_m renormalizes the onsite energies in the outer dots, as shown in Eq. (4.11).

4.4.2. FINITE ZEEMAN SPLITTING IN THE MIDDLE DOT

The presence of Zeeman splitting in the middle dot B introduces (see Appendix 4.A) an asymmetric the onsite renormalisation $\epsilon_L^{\sigma_i\sigma_j} \neq \epsilon_R^{\sigma_i\sigma_j}$ and a shift in the minima of $\Gamma_{\sigma_i\sigma_j}$

shifts away from $\mu_M = 0$, as shown in Fig. 4.2. These changes affect the prescriptions for $\mathscr{U}_2$ and $\mathscr{U}_3$ since these operations require finite t.

The asymmetric onsite corrections break the orthogonality between $\mathscr{U}_1$ and the unitary operation prescribed in Eq. (4.16). It is still possible to implement the $\mathscr{U}_2$ with two non-orthogonal rotation axes in the odd fermion parity sector with additional operations to compensate for the non-orthogonality [35].

The operation in Eq. (4.17) also introduces finite $\Gamma_{\sigma_i\sigma_j}$ in the odd parity sector. We show in Appendix 4.B that anti-parallel spin configuration with symmetric spin-orbit precession $\theta_L = \theta_R$ removes the shifting Λ minima away from $\mu_M = 0$ and restores the orthogonality of the operations within the even parity sector.

4.4.3. GATE PERFORMANCE

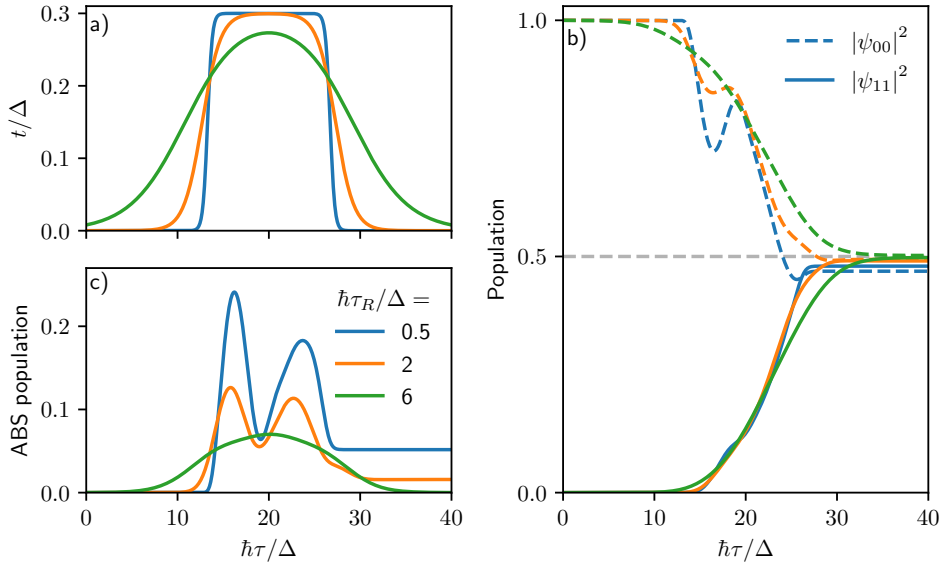

Figure 4.3: Time-dependent simulation of pairing gate $\mathscr{U}_3$ acting on an initial vacuum state with different pulse rise time τ_R profiles. The vacuum population is $|\psi_{00}|^2$ whereas the double occupation population (with middle dot unoccupied) is $|\psi_{11}|^2$. Longer pulses (a) result in a smoother transient population profile (b) and less leakage into the middle ABS state (c). The configuration is the spin-antiparallel with finite Zeeman field within the middle dot $B/\Delta = 0.2$ and symmetric spin-orbit precession $\theta_L = \theta_R = \pi/8$

Switching on the pulse in Eq. (4.13) happens over a finite rise time τ_R. Short rise times τ_R induce transitions from the LFM dots into the middle ABS at energy $\sim \Delta$ which limits the performance of the gates. To avoid such transitions, the pulse times need to be $\tau_R \gg \hbar/\Delta$. In Fig. 4.2 we show the time-dependent simulation of the gate $\mathscr{U}_3$ with different rise times. We find that rise times $\tau_R > 2\hbar/\Delta$ ensures negligible transitions into the ABS. In a system of $\Delta = 100\,\mu$eV that corresponds to rise times of $\tau_R > 13$ ps.

Current tunable capacitors [25, 26] vary over a limited range. The upper limit for the ratio between the maximum and minimum capacitance $r = C_{\text{off}}/C_{\text{on}}$ is $r \approx 40$ [25, 26].

Thus, there is a non-negligible residual capacitance between the dots when the $\mathcal{U}_4$ gate is off. This residual capacitance acts as an unwanted source of phase and limits the performance of the device. Because such error is coherent, we argue it is possible to offset it after each or a few operations with a compensating $\mathcal{U}_4$ pulse. However, since $[\mathcal{U}_3, \mathcal{U}_4] \neq 0$, the $\mathcal{U}_3$ operation would require similar compensation pulses to Eq. (4.16) to offset the effect of the residual capacitor.

4.5. FUTURE DIRECTIONS

Although the device we proposed has the ingredients to implement universal fermionic gates, further work is required to mitigate the main sources of errors. Because of its similarities to a quantum dot charge qubit, we expect the limiting decoherence mechanism to be the same - charge noise [36]. Typical coherence times are on the order of a few nanoseconds [21, 36–38]. In comparison, Dvir et al. [20] reports CAR/ECT strengths of $\hbar/\Gamma_{\mathrm{CAR/ECT}} \approx 10\,\mu\mathrm{s}$ from which we estimate the gate pulse of our proposed device to be $\approx 50\,\mathrm{ps}$. On the other hand, if the outer dots in the device shown in Fig. 6.1 are also proximitized by a superconductor, the local fermionic modes would be encoded by Andreev quasiparticles. Because Andreev states are linear combinations of electron and hole-like excitations, it is possible to design a device that operates with neutral fermions. A similar idea was recently proposed to avoid charge noise in fermion-parity qubits [39]. Finally, minimization of the main sources of errors allows implementation of error-correction codes for fermionic systems [40].

In the current device, superconducting pairing persists under all possible parameters. Because of that, the hopping operation in Eq. (4.16) requires a complicated procedure in order to remove the effects of the induced superconducting gap. To simplify the hopping operation, we suggest using a device that allows control of the amount of induced superconducting pairing into the middle dot. For example, a tunnel barrier between the middle dot and the superconducting lead would mediate the induced superconducting pairing. Alternatively, connecting the middle dot to two superconducting leads and controlling the phase difference between them would also allow to control the induced superconducting pairing.

Our proposed device consists of a chain of single-orbital fermionic sites. The device layout is a limiting factor, as it only allows nearest-neighbor hoppings, superconducting pairing, and electrostatic interactions. The layout limitations are detrimental to effective scalability. Thus, future works could for example generalize the model to, for example, two-dimensional lattices.

We showed that the proposed device is a building block of a fermionic quantum computer. However, we must also emphasize that the high control of the system parameters allows to use the same device as a quantum simulator. For example, a chain-like device with the unit cell shown in Fig. 6.1 at finite Γ and U can be directly mapped to the Heisenberg model. Thus, together with superconducting correlations, these devices would be an extension of other quantum dot platforms [41].

We mentioned in Sec. 4.4 that all tunable capacitors proposed present a residual mutual capacitance C_{off}. The external capacitor is necessary because direct mutual capacitance is suppressed by the charge screening in the superconducting island. On the other hand, a floating superconducting island offers a direct interdot capacitance [42]. In

a device with a switch between a floating and grounded superconductor, there would be direct control of the mutual capacitance. Moreover, the large charge screening due to the grounded superconducting island sets $C_{\text{off}} \approx 0$, removing the need to fix offset phases due to the residual capacitance.

4.6. SUMMARY

We showed that Copper pair-splitting devices with tunable capacitors make up a building block of a fermionic quantum computer. We derived the low-energy Hamiltonian and showed that it contains all the necessary processes to build a universal set of gate operations. Moreover, we showed how to use experimentally controllable parameters to implement the gate operations. We find that the presence of Zeeman splitting in the superconducting island complicates the implementation of gates and necessitates additional steps. Based on the low-energy theory, we also studied optimal regimes for the device operation. While our design was mostly inspired by recent experiments, we also discussed how to avoid foreseeable limitations such as (i) the use of neutral fermions to suppress charge noise; (ii) a floating superconducting island to simplify the layout; (iii) control of the superconducting gap to simplify gate operations.

ACKNOWLEDGEMENTS

The authors acknowledge the inputs of: Isidora Araya Day on perturbation theory calculations; Mert Bozkurt and Chun-Xiao Liu on the device conception and development of an effective model; Christian Prosko, Valla Fatemi, David van Driel, Francesco Zatelli, and Greg Mazur on the experimental feasibility.

DATA AVAILABILITY

All code used in the manuscript is available on Zenodo [32].

AUTHOR CONTRIBUTIONS

A.A and M.W. formulated the initial project idea and advised on various technical aspects. K.V. and A.M. supervised the project. K.V., A.M. and J.T. developed the effective model and the device design. K.V., A.M., J.T, and S.M. constructed the gate operations. K.V. performed the time-dependent calculations. All authors contributed to the final version of the manuscript.

FUNDING INFORMATION

The project received funding from the European Research Council (ERC) under the European Union's Horizon 2020 research and innovation program grant agreement No. 828948 (AndQC). The work acknowledges NWO HOT-NANO grant (OCENW.GROOT.2019.004) and VIDI Grant (016.Vidi.189.180) for the research funding.

4.A. SCHIEFFER-WOLFF TRANSFORMATION

To obtain the effective Hamiltonian from Eq. (4.6), we perform a Schieffer-Wolff transformation. We, first, diagonalize the Hamiltonian of the middle dot in Eq. (4.3):

$$H_{\mathrm{ABS}} = (\epsilon_{\mathrm{ABS}} + B)\gamma_{\uparrow}^{\dagger}\gamma_{\uparrow} + (\epsilon_{\mathrm{ABS}} - B)\gamma_{\downarrow}^{\dagger}\gamma_{\downarrow}\,, \tag{4.19}$$

where $\epsilon_{\mathrm{ABS}} = \sqrt{\Delta^2 + \mu_M^2}$, γ_σ are the annihillation operators of Andreev quasiparticles

$$\gamma_{\uparrow}^{\dagger} = uc_{M\uparrow}^{\dagger} + vc_{M\downarrow}\,, \quad \gamma_{\downarrow}^{\dagger} = uc_{M\downarrow}^{\dagger} - vc_{M\uparrow}\,, \tag{4.20}$$

and u and v are the coherence factors.

We now define the occupation basis for the many-body states as $|n_L, n_M, n_R\rangle$, where n_i corresponds to the occupation number at the site i. Notice that for the middle dot, we define the number operator as $\hat{n}_{M\sigma} = \gamma_{M\sigma}^{\dagger}\gamma_{M\sigma}$, whereas in the outer dots $\hat{n}_{i\sigma_i} = c_{i\sigma_i}^{\dagger}c_{i\sigma_i}$. Because we consider $\mu_{L/R}, B \ll \Delta$, in the absence of hopping between the dots,

$$\langle n_L, 0, n_R|H|n_L, 0, n_R\rangle \ll \langle n_L, n_M, n_R|H|n_L, n_M, n_R\rangle\,, \tag{4.21}$$

for $n_{L/R} \in \{0, 1\}$, and $n_M > 0$. Thus, the states with zero occupation in the middle dot form our low-energy manifold.

Occupied states in the middle dot are separated by an energy $\sim \Delta$ from the low-energy manifold. In the weak coupling limit $t \ll \Delta$, the high-energy subspace only contributes to the low-energy dynamics through virtual processes. Therefore, we use a Schieffer-Wolff transformation to obtain the effective Hamiltonian in the low-energy subspace in Eq. (4.6). Whenever $\mu_L = \mu_R = 0$, the terms in Eq. (4.6) for the anti-parallel spin configuration are:

$$\epsilon_R^{\uparrow\downarrow} = \kappa\left(-2B\sin^2(\theta_R) + B + \mu_M\right), \quad \epsilon_L^{\uparrow\downarrow} = \kappa\left(-2B\cos^2(\theta_L) + B + \mu_M\right), \tag{4.22}$$

$$\Lambda_{\uparrow\downarrow} = \kappa\Delta\cos(\theta_L + \theta_R)\,, \quad \Gamma_{\uparrow\downarrow} = -i\kappa\left[\mu_M\cos(\theta_L + \theta_R) - B\sin(\theta_L - \theta_R)\right]\,, \tag{4.23}$$

and for the parallel configuration:

$$\epsilon_R^{\uparrow\uparrow} = \kappa\left(-2B\cos^2(\theta_R) + B + \mu_M\right), \quad \epsilon_L^{\uparrow\uparrow} = \kappa\left(-2B\cos^2(\theta_L) + B + \mu_M\right), \tag{4.24}$$

$$\Lambda_{\uparrow\uparrow} = -i\kappa\Delta\sin(\theta_L + \theta_R)\,, \quad \Gamma_{\uparrow\uparrow} = -\kappa\left[\mu_M\cos(\theta_L + \theta_R) - B\cos(\theta_L - \theta_R)\right]\,, \tag{4.25}$$

where

$$\kappa = t^2/(\Delta^2 + \mu_M^2 - B^2)\,. \tag{4.26}$$

At finite B, the chemical potential μ_M at which $\Gamma_{\sigma_i\sigma_j} = 0$ shifts to:

$$\mu_{\mathrm{shift}}^{\uparrow\downarrow} = \frac{B\sin(\theta_L - \theta_R)}{\sin(\theta_L + \theta_R)}, \quad \mu_{\mathrm{shift}}^{\uparrow\uparrow} = \frac{B\cos(\theta_L - \theta_R)}{\cos(\theta_L + \theta_R)}\,, \tag{4.27}$$

for anti-parallel and parallel spin configurations.

4.B. CONVENIENCE OF THE ANTI-PARALLEL SPIN CONFIGURATION

4.B.1. ORTHOGONALITY WITH SYMMETRIC SPIN PRECESSION

In Eq. (4.22) for the anti-parallel spin configuration we notice that when the spin precession angles are equal $\theta_L = \theta_R = \theta$, the double occupation onsite energy $\epsilon_L + \epsilon_R = 0$ is zero at $\mu_M = 0$ and the ETC minima shifts disappear as shown in Eq. (4.27). That restores the orthogonality of operations within the even parity sector and thus we express $\mathscr{U}_3(\gamma)$ operation as:

$$\mathscr{U}_3(\gamma) = \exp\left[-\frac{i}{\hbar} H_P\left(\{\mu_{L/R}\}\right)\tau_P^{(2)}\right] \times \exp\left[-\frac{i}{\hbar} H_P\left(\{t\}\right)\tau_P^{(1)}\right], \tag{4.28}$$

where we compensate a finite $\epsilon_L - \epsilon_R$ with an onsite pulse. On the other hand, the hopping operation requires additional operations to compensate for non-orthogonality [35]:

$$\begin{aligned}\mathscr{U}_2(\beta) = &\exp\left[-\frac{i}{\hbar} H_P\left(\{\mu_L = \mu, \mu_R = \mu\}\right)\tau_P^{(N+4)}\right] \times \exp\left[-\frac{i}{\hbar} H_P\left(\{t\}\right)\tau_P^{(N+3)}\right] \\ &\times \exp\left[-\frac{i}{\hbar} H_P\left(\{\mu_L = \mu, \mu_R = \mu\}\right)\tau_P^{(N+2)}\right] \times \exp\left[-\frac{i}{\hbar} H_P\left(\{\mu_{L/R}\}\right)\tau_P^{(N+1)}\right] \\ &\times \prod_{j=1}^{N/2} \exp\left[-\frac{i}{\hbar} H_P\left(\{t, \mu_M\}\right)\tau_P^{(2j)}\right] \times \exp\left[-\frac{i}{\hbar} H_P\left(\{\mu_{L/R}\}\right)\tau_P^{(2j-1)}\right]\end{aligned} \tag{4.29}$$

where N is the number of pulses required to correct for the non-orthogonality within the odd parity sector.

4.B.2. STABILITY AND NUMBER OF OPERATIONS

To quantify the degree of linear dependence of the operations, we define the following metric

$$\mathscr{L}_o = \sqrt{\frac{(\epsilon_L - \epsilon_R)^2}{(\epsilon_L - \epsilon_R)^2 + \Gamma^2}}, \tag{4.30}$$

$$\mathscr{L}_e = \sqrt{\frac{(\epsilon_L + \epsilon_R)^2}{(\epsilon_L + \epsilon_R)^2 + \Lambda^2}} \tag{4.31}$$

for $\mathscr{L}_e$ even $\mathscr{L}_o$ and odd fermion parity sectors. If $\mathscr{L}_{e/o} = 0$, the operations are orthogonal and the scheme outlined in Section 4.4 is valid. On the other hand, if $\mathscr{L}_{e/o} = 1$, it is impossible to generate a universal set of operations. To understand how robust the scheme in Eq. (4.28) is, we consider small deviations from the perfect spin precession case: $\theta_L = \theta$ and $\theta_R = \theta + \delta$. In this case, the metric $\mathscr{L}_{e/o}$ reads:

$$\mathscr{L}_o = \left[1 + \left(\frac{\mu_M}{B}\tan 2\theta\right)^2\right]^{-1/2} + O(\delta), \tag{4.32}$$

$$\mathscr{L}_e = \delta\left(\frac{B}{\Delta}\right)\tan 2\theta + O(\delta^2). \tag{4.33}$$

Depending on the linear dependence $\mathscr{L}_{e/o}$ of the hopping and pairing operations, we can estimate the maximal number of pulses required to implement an arbitrary operation [35] within a given fermion parity subspace:

$$\mathscr{N}(\mathscr{L}_{e/o}) = \lceil \frac{\pi}{\arccos(\mathscr{L}_{e/o})} \rceil + 1. \tag{4.34}$$

REFERENCES

[1] M. H. Devoret and R. J. Schoelkopf, *Superconducting circuits for quantum information: An outlook,* Science **339**, 1169 (2013).

[2] M. Kjaergaard, M. E. Schwartz, J. Braumüller, P. Krantz, J. I.-J. Wang, S. Gustavsson, and W. D. Oliver, *Superconducting qubits: Current state of play,* Annual Review of Condensed Matter Physics **11**, 369 (2020).

[3] C. D. Bruzewicz, J. Chiaverini, R. McConnell, and J. M. Sage, *Trapped-ion quantum computing: Progress and challenges,* Applied Physics Reviews **6**, 021314 (2019).

[4] H. Häffner, C. Roos, and R. Blatt, *Quantum computing with trapped ions,* Physics Reports **469**, 155 (2008).

[5] G. Burkard, T. D. Ladd, A. Pan, J. M. Nichol, and J. R. Petta, *Semiconductor spin qubits,* Rev. Mod. Phys. **95**, 025003 (2023).

[6] A. Rahmani, K. J. Sung, H. Putterman, P. Roushan, P. Ghaemi, and Z. Jiang, *Creating and manipulating a laughlin-type $\nu = 1/3$ fractional quantum hall state on a quantum computer with linear depth circuits,* PRX Quantum **1** (2020), 10.1103/prxquantum.1.020309.

[7] F. Arute, K. Arya, R. Babbush, D. Bacon, J. C. Bardin, R. Barends, A. Bengtsson, S. Boixo, M. Broughton, B. B. Buckley, D. A. Buell, B. Burkett, N. Bushnell, Y. Chen, Z. Chen, Y.-A. Chen, B. Chiaro, R. Collins, S. J. Cotton, W. Courtney, S. Demura, A. Derk, A. Dunsworth, D. Eppens, T. Eckl, C. Erickson, E. Farhi, A. Fowler, B. Foxen, C. Gidney, M. Giustina, R. Graff, J. A. Gross, S. Habegger, M. P. Harrigan, A. Ho, S. Hong, T. Huang, W. Huggins, L. B. Ioffe, S. V. Isakov, E. Jeffrey, Z. Jiang, C. Jones, D. Kafri, K. Kechedzhi, J. Kelly, S. Kim, P. V. Klimov, A. N. Korotkov, F. Kostritsa, D. Landhuis, P. Laptev, M. Lindmark, E. Lucero, M. Marthaler, O. Martin, J. M. Martinis, A. Marusczyk, S. McArdle, J. R. McClean, T. McCourt, M. McEwen, A. Megrant, C. Mejuto-Zaera, X. Mi, M. Mohseni, W. Mruczkiewicz, J. Mutus, O. Naaman, M. Neeley, C. Neill, H. Neven, M. Newman, M. Y. Niu, T. E. O'Brien, E. Ostby, B. Pató, A. Petukhov, H. Putterman, C. Quintana, J.-M. Reiner, P. Roushan, N. C. Rubin, D. Sank, K. J. Satzinger, V. Smelyanskiy, D. Strain, K. J. Sung, P. Schmitteckert, M. Szalay, N. M. Tubman, A. Vainsencher, T. White, N. Vogt, Z. J. Yao, P. Yeh, A. Zalcman, and S. Zanker, *Observation of separated dynamics of charge and spin in the fermi-hubbard model,* (2020), arXiv:2010.07965 [quant-ph] .

[8] G. A. Quantum, Collaborators*†, F. Arute, K. Arya, R. Babbush, D. Bacon, J. C. Bardin, R. Barends, S. Boixo, M. Broughton, B. B. Buckley, D. A. Buell, B. Burkett, N. Bushnell, Y. Chen, Z. Chen, B. Chiaro, R. Collins, W. Courtney, S. Demura, A. Dunsworth, E. Farhi, A. Fowler, B. Foxen, C. Gidney, M. Giustina, R. Graff, S. Habegger, M. P. Harrigan, A. Ho, S. Hong, T. Huang, W. J. Huggins, L. Ioffe, S. V. Isakov, E. Jeffrey, Z. Jiang, C. Jones, D. Kafri, K. Kechedzhi, J. Kelly, S. Kim, P. V. Klimov, A. Korotkov, F. Kostritsa, D. Landhuis, P. Laptev, M. Lindmark, E. Lucero, O. Martin, J. M. Martinis, J. R. McClean, M. McEwen, A. Megrant, X. Mi, M. Mohseni, W. Mruczkiewicz, J. Mutus, O. Naaman, M. Neeley, C. Neill, H. Neven, M. Y. Niu, T. E. O'Brien, E. Ostby, A. Petukhov, H. Putterman, C. Quintana, P. Roushan, N. C. Rubin, D. Sank, K. J. Satzinger, V. Smelyanskiy, D. Strain, K. J. Sung, M. Szalay, T. Y. Takeshita, A. Vainsencher, T. White, N. Wiebe, Z. J. Yao, P. Yeh, and A. Zalcman, *Hartree-fock on a superconducting qubit quantum computer,* Science **369**, 1084 (2020).

[9] S. McArdle, S. Endo, A. Aspuru-Guzik, S. C. Benjamin, and X. Yuan, *Quantum computational chemistry,* Rev. Mod. Phys. **92**, 015003 (2020).

[10] J. D. Whitfield, J. Biamonte, and A. Aspuru-Guzik, *Simulation of electronic structure hamiltonians using quantum computers,* Mol. Phys. **109**, 735 (2011).

[11] A. S. Wightman, ed., *The Collected Works of Eugene Paul Wigner* (Springer Berlin Heidelberg, 1993).

[12] S. B. Bravyi and A. Y. Kitaev, *Fermionic quantum computation,* Ann. Phys-new. York. **298**, 210 (2002).

[13] Y. Herasymenko, M. Stroeks, J. Helsen, and B. Terhal, *Optimizing sparse fermionic hamiltonians,* Quantum **7**, 1081 (2023).

[14] M. B. Hastings and R. O'Donnell, *Optimizing strongly interacting fermionic hamiltonians,* in *Proceedings of the 54th Annual ACM SIGACT Symposium on Theory of Computing* (ACM, 2022).

[15] M. Leijnse and K. Flensberg, *Parity qubits and poor man's majorana bound states in double quantum dots,* Phys. Rev. B **86** (2012), 10.1103/physrevb.86.134528.

[16] Q. Wang, S. L. D. ten Haaf, I. Kulesh, D. Xiao, C. Thomas, M. J. Manfra, and S. Goswami, *Triplet cooper pair splitting in a two-dimensional electron gas,* (2022), arXiv:2211.05763 [cond-mat.mes-hall] .

[17] G. Wang, T. Dvir, G. P. Mazur, C.-X. Liu, N. van Loo, S. L. D. ten Haaf, A. Bordin, S. Gazibegovic, G. Badawy, E. P. A. M. Bakkers, M. Wimmer, and L. P. Kouwenhoven, *Singlet and triplet cooper pair splitting in hybrid superconducting nanowires,* Nature **612**, 448 (2022).

[18] C.-X. Liu, G. Wang, T. Dvir, and M. Wimmer, *Tunable superconducting coupling of quantum dots via andreev bound states in semiconductor-superconductor nanowires,* Phys. Rev. Lett. **129**, 267701 (2022).

[19] A. Bordin, G. Wang, C.-X. Liu, S. L. D. ten Haaf, G. P. Mazur, N. van Loo, D. Xu, D. van Driel, F. Zatelli, S. Gazibegovic, G. Badawy, E. P. A. M. Bakkers, M. Wimmer, L. P. Kouwenhoven, and T. Dvir, *Controlled crossed andreev reflection and elastic co-tunneling mediated by andreev bound states,* (2022), arXiv:2212.02274 [cond-mat.mes-hall] .

[20] T. Dvir, G. Wang, N. van Loo, C.-X. Liu, G. P. Mazur, A. Bordin, S. L. D. ten Haaf, J.-Y. Wang, D. van Driel, F. Zatelli, X. Li, F. K. Malinowski, S. Gazibegovic, G. Badawy, E. P. A. M. Bakkers, M. Wimmer, and L. P. Kouwenhoven, *Realization of a minimal kitaev chain in coupled quantum dots,* Nature **614**, 445 (2023).

[21] D. Kim, D. R. Ward, C. B. Simmons, J. K. Gamble, R. Blume-Kohout, E. Nielsen, D. E. Savage, M. G. Lagally, M. Friesen, S. N. Coppersmith, and M. A. Eriksson, *Microwave-driven coherent operation of a semiconductor quantum dot charge qubit,* Nature Nanotechnology **10**, 243 (2015).

[22] J. Gorman, D. G. Hasko, and D. A. Williams, *Charge-qubit operation of an isolated double quantum dot,* Phys. Rev. Lett. **95**, 090502 (2005).

[23] M. W. A. de Moor, J. D. S. Bommer, D. Xu, G. W. Winkler, A. E. Antipov, A. Bargerbos, G. Wang, N. van Loo, R. L. M. O. het Veld, S. Gazibegovic, D. Car, J. A. Logan, M. Pendharkar, J. S. Lee, E. P. A. M. Bakkers, C. J. Palmstrøm, R. M. Lutchyn, L. P. Kouwenhoven, and H. Zhang, *Electric field tunable superconductor-semiconductor coupling in majorana nanowires,* New J. Phys. **20**, 103049 (2018).

[24] I. van Weperen, B. Tarasinski, D. Eeltink, V. S. Pribiag, S. R. Plissard, E. P. A. M. Bakkers, L. P. Kouwenhoven, and M. Wimmer, *Spin-orbit interaction in insb nanowires,* Phys. Rev. B **91**, 201413 (2015).

[25] N. Materise, M. C. Dartiailh, W. M. Strickland, J. Shabani, and E. Kapit, *Tunable capacitor for superconducting qubits using an InAs/InGaAs heterostructure,* Quantum Science and Technology **8**, 045014 (2023).

[26] R. S. Eggli, S. Svab, T. Patlatiuk, D. Trüssel, M. J. Carballido, P. C. Kwon, S. Geyer, A. Li, E. P. A. M. Bakkers, A. V. Kuhlmann, and D. M. Zumbühl, *Cryogenic hyperabrupt strontium titanate varactors for sensitive reflectometry of quantum dots,* (2023), arXiv:2303.02933 [cond-mat.mes-hall] .

[27] A. Hamo, A. Benyamini, I. Shapir, I. Khivrich, J. Waissman, K. Kaasbjerg, Y. Oreg, F. von Oppen, and S. Ilani, *Electron attraction mediated by coulomb repulsion,* Nature **535**, 395 (2016).

[28] W. Lu, Z. Ji, L. Pfeiffer, K. W. West, and A. J. Rimberg, *Real-time detection of electron tunnelling in a quantum dot,* Nature **423**, 422 (2003).

[29] S. T. Gill, J. Damasco, D. Car, E. P. A. M. Bakkers, and N. Mason, *Hybrid superconductor-quantum point contact devices using InSb nanowires,* Applied Physics Letters **109** (2016), 10.1063/1.4971394.

[30] Önder Gül, H. Zhang, F. K. de Vries, J. van Veen, K. Zuo, V. Mourik, S. Conesa-Boj, M. P. Nowak, D. J. van Woerkom, M. Quintero-Pérez, M. C. Cassidy, A. Geresdi, S. Koelling, D. Car, S. R. Plissard, E. P. A. M. Bakkers, and L. P. Kouwenhoven, *Hard superconducting gap in InSb nanowires,* Nano Letters **17**, 2690 (2017).

[31] T. D. Stanescu and S. Das Sarma, *Proximity-induced low-energy renormalization in hybrid semiconductor-superconductor majorana structures,* Phys. Rev. B **96**, 014510 (2017).

[32] K. Vilkelis, A. Manesco, J. D. Torres Luna, S. Miles, M. Wimmer, and A. Akhmerov, *Fermionic quantum computation with Cooper pair splitters,* (2023).

[33] I. Araya Day, S. Miles, D. Varjas, and A. R. Akhmerov, *Pymablock,* (2023).

[34] W. G. van der Wiel, S. De Franceschi, J. M. Elzerman, T. Fujisawa, S. Tarucha, and L. P. Kouwenhoven, *Electron transport through double quantum dots,* Rev. Mod. Phys. **75**, 1 (2002).

[35] M. Hamada, *The minimum number of rotations about two axes for constructing an arbitrarily fixed rotation,* Royal Society Open Science **1**, 140145 (2014).

[36] K. D. Petersson, J. R. Petta, H. Lu, and A. C. Gossard, *Quantum coherence in a one-electron semiconductor charge qubit,* Phys. Rev. Lett. **105**, 246804 (2010).

[37] B. P. Wuetz, D. D. Esposti, A.-M. J. Zwerver, S. V. Amitonov, M. Botifoll, J. Arbiol, A. Sammak, L. M. K. Vandersypen, M. Russ, and G. Scappucci, *Reducing charge noise in quantum dots by using thin silicon quantum wells,* Nature Communications **14** (2023), 10.1038/s41467-023-36951-w.

[38] J. W. G. van den Berg, S. Nadj-Perge, V. S. Pribiag, S. R. Plissard, E. P. A. M. Bakkers, S. M. Frolov, and L. P. Kouwenhoven, *Fast spin-orbit qubit in an indium antimonide nanowire,* Phys. Rev. Lett. **110**, 066806 (2013).

[39] M. Geier, R. S. Souto, J. Schulenborg, S. Asaad, M. Leijnse, and K. Flensberg, *A fermion-parity qubit in a proximitized double quantum dot,* (2023), arXiv:2307.05678 [cond-mat.mes-hall] .

[40] S. Vijay and L. Fu, *Quantum error correction for complex and majorana fermion qubits,* (2017), arXiv:1703.00459 [cond-mat.mes-hall] .

[41] C. van Diepen, T.-K. Hsiao, U. Mukhopadhyay, C. Reichl, W. Wegscheider, and L. Vandersypen, *Quantum simulation of antiferromagnetic heisenberg chain with gate-defined quantum dots,* Physical Review X **11** (2021), 10.1103/physrevx.11.041025.

[42] F. K. Malinowski, R. K. Rupesh, L. Pavešić, Z. Guba, D. de Jong, L. Han, C. G. Prosko, M. Chan, Y. Liu, P. Krogstrup, A. Pályi, R. Žitko, and J. V. Koski, *Quantum capacitance of a superconducting subgap state in an electrostatically floating dot-island,* (2022), arXiv:2210.01519 [cond-mat.mes-hall] .

5

ELECTRONIC PROPERTIES OF INAS/EUS/AL HYBRID NANOWIRES

This chapter has been previously published as Chun-Xiao Liu, Sergej Schuwalow, Yu Liu, Kostas Vilkelis, A. L. R. Manesco, P. Krogstrup, and Michael Wimmer *Electronic properties of InAs/EuS/Al hybrid nanowires,* Phys. Rev. B 104, 014516 (2021).
Own contribution to work: I contributed to performing an survey on the appropriate model of the hybrid nanowire.

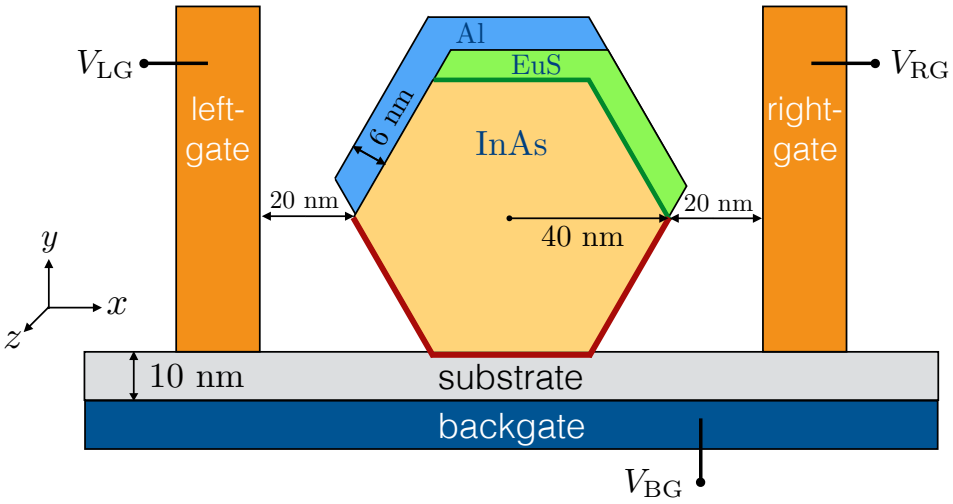

Figure 5.1: Schematic of the device studied in the experiment [30] and in this work. An InAs nanowire (yellow) is partially covered by Al (blue) and EuS (green) layers and is placed on a dielectric substrate (grey). A back-gate (dark blue) and two side-gates (orange) are applied to control the electrostatic potential profile in the InAs nanowire. Surface charges are added on the three facets of the bare InAs nanowire (brown) and on the two facets of the InAs/EuS interface (dark green) to account for the band bending effect.

5.1. Introduction

Topological superconductivity (TSC) has attracted lots of attention and inspired intensive research over the last few decades. The defects or wire ends of a TSC can host Majorana zero modes which are non-Abelian anyons and potential building blocks of topological quantum computing [1–14]. Heterostructures between a spin-orbit coupled semiconducting nanowire and a conventional *s*-wave superconductor is one of the promising platforms for realizing TSC [15–18]. In these hybrid devices, topological superconductivity is realized for a sufficiently strong Zeeman splitting.

In most experimental studies of semiconductor-superconductor hybrid nanowires so far, Zeeman splitting is induced by an externally applied magnetic field [19–29]. However, Zeeman energy in the hybrid system can also be induced by proximity effect from ferromagnetic insulators (FMI) [15, 18]. In a recent experiment, topological properties of InAs/EuS/Al ferromagnetic (FM) hybrid nanowires have been investigated [30]. Tunneling spectroscopy revealed zero-bias conductance peaks over a finite parameter regime for multiple devices, compatible with Majorana zero modes and topological superconductivity. Interestingly, such zero-bias peaks have appeared only in devices of a particular geometry, namely when the Al and EuS layers overlap with each other by one facet (see Fig. 5.1), but not in other device geometries without such an overlap. This raises the question on the fundamental physical mechanisms for realizing TSC in such ferromagnetic hybrid nanowires.

In this work, we explore systematically different mechanisms for inducing an effective Zeeman energy in the nanowire, using detailed microscopic device simulations. To this

end it is essential to have a faithful description of the electrostatic potential in the device. Previous works highlighted the critical role of band offsets at interfaces of the semiconductor with other materials [31, 32]. For the bare InAs surface and the InAs/Al interface this has been studied systematically using angle-resolved photoemission spectroscopy (ARPES) [33], but no such analysis has been available for the InAs/EuS interface so far.

We combine an analysis of the band offset at the InAs/EuS interface from ARPES data with electrostatic device simulations to arrive at a faithful description of the electronic density in these hybrid nanowires. In particular, we find that the enhanced band bending at the InAs/EuS interface leads to an accumulation of electrons along these facets. Using a microscopic model for superconductivity we conclude that the magnetic proximity effects at the Al/EuS as well as the InAs/EuS interfaces are both essential for inducing a sufficiently large effective Zeeman spin splitting allowing to reach a topological phase. Our calculations show that a topological phase can be reached with plausible parameter values, and we discuss how topological properties can be optimized by external gating.

5.2. BAND BENDING AND ELECTROSTATICS

5.2.1. BAND BENDING AT THE INAS/EUS INTERFACE

Accurate values of band offset at the interface of InAs with other materials are crucial for obtaining faithful electrostatic potential and charge density profiles inside the InAs nanowire. In a previous work [33], the planar interfaces of InAs/Al and InAs/vacuum were both carefully investigated using the ARPES measurements along with the core-level fitting procedure. The resulting values of the band offset of InAs(100)/Al and InAs(100)/vacuum, and the band bending profile near the interface are summarized as the blue and red lines in Fig. 5.2 (data from Ref. [33]).

In this work, we focus on the band bending effect at the InAs(100)/EuS interface. ARPES data obtained for this interface has been presented in Ref. [34]. Here, we use the methods described in Ref. [33] to extract the band bending from this data. In particular, the fit of the In4d core-level spectra for the InAs/EuS interface is performed simultaneously for a set of photon energies in the range 350-750 eV. We use a bulk and an interface component consisting of two Voigt functions each. The broadening and shift of the line profile by the band bending potential is accounted for using an auxiliary Schrödinger-Poisson simulation and the characteristic energy between the conduction band minimum and the In4d core level $\Delta_{\mathrm{CL}}(\mathrm{In4d,InAs}) = -17.22(3)$ eV for InAs [33].

The result of the core-level fitting for $h\nu = 750$ eV is shown in the inset of Fig. 5.2. While the overall shape of the core line is well captured by our model, the bulk component binding energy seems to be underestimated by ~0.08 eV. We suspect that this may be caused by nonlinear behavior of the background or by a small additional interface component that is not adequately captured in our approach, which is reflected in the increased estimate for the confidence interval towards lower binding energies. The bend bending profile of InAs(100)/EuS interface is shown as the green line in Fig. 5.2, and we see that the band offset value of InAs/EuS is in between the values of InAs/Al and InAs/vacuum.

Finally, we note that owing to the geometrical difference between a planar interface and a multi-facet nanowire structure, the band offset values shown in Fig. 5.2 should be regarded as guiding values. For the InAs/Al interface specifically, we typically observe the

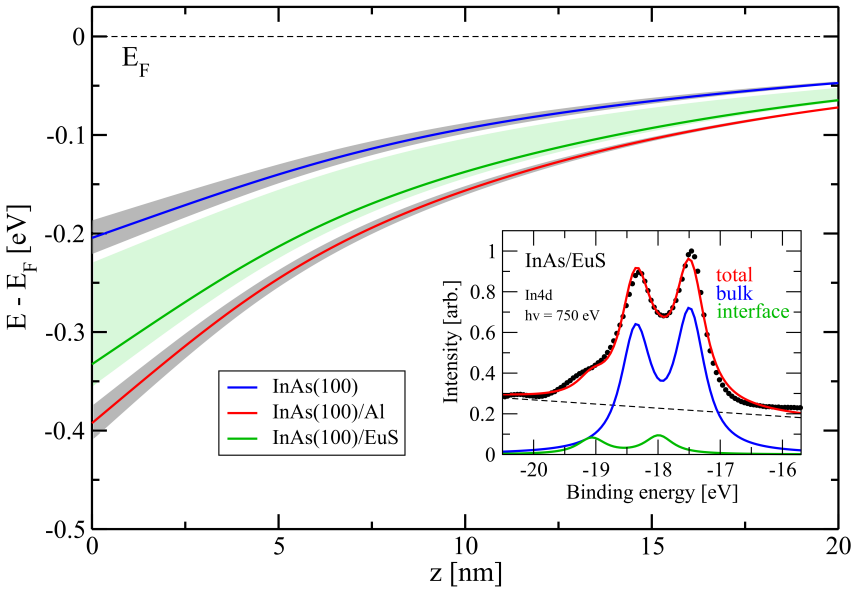

Figure 5.2: Interface band offsets and band bending profiles for the bare InAs(100) planar surface, the InAs(100)/Al, and InAs(100)/EuS heterostructures. Estimated confidence intervals are shown in grey and light green, respectively. Inset: Fit of the In4d core-level peaks of the InAs/EuS heterostructure for photon energy $h\nu$ = 750 eV. The InAs(100)/EuS interface was grown in the MBE system of the Niels Bohr Institute in Copenhagen and transported for spectroscopic measurements at the ADRESS beamline of the SWISS Light Source at PSI, Switzerland in protective atmosphere. Data for InAs and InAs/Al is from Ref. [33], and ARPES data obtained for InAs/EuS interface is in Ref. [34].

value of band offset for in-situ planar MBE growth shown here to be an upper bound, with a reduction of 0.05-0.1 eV for interfaces with a reduced quality using other growth modes such as growth after decapping. We can expect this to apply to growth on nanowire facets. So without loss of generality, in this work we choose the band offset values in our model to be $W_{\mathrm{InAs/vac}}$ =0.2 eV, $W_{\mathrm{InAs/EuS}}$ =0.26 eV and $W_{\mathrm{InAs/Al}}$ =0.35 eV, respectively.

5.2.2. Thomas Fermi-Poisson approach

The setup for studying the electrostatics in this work is schematically shown in Fig. 5.1. We focus on the two-dimensional cross section (in the x-y plane) of the system, and assume translational symmetry along the third dimension (z axis). The hexagonal InAs nanowire of radius 40 nm is covered by the EuS layer on two of the top facets, and also covered by the Al layer on one adjacent facet. The hybrid nanowire is placed on a dielectric layer of thickness 10 nm, and a back-gate and two side-gates are applied below or beside the nanowire. To obtain the electrostatic potential $\phi(\mathbf{r})$ for the setup, we solve

Table I. Physical parameters for InAs and Al

Parameter (unit)	InAs	Al
m (m_0)	0.023 [39]	1
α_R (eVÅ)	0.3 [44]	0
E_F(eV)	0	11.27 [45]
Δ_0 (meV)	0	0.34 [45]
ε_r	15.15	

the self-consistent Thomas Fermi-Poisson equation [31, 32, 35–38]

$$\nabla \cdot [\varepsilon_r(\mathbf{r})\nabla\phi(\mathbf{r})] = \frac{\rho_{\text{tot}}[\phi(\mathbf{r})]}{\varepsilon_0}, \tag{5.1}$$

with appropriate boundary conditions. Here the total charge density

$$\rho_{\text{tot}}[\phi(\mathbf{r})] = \rho_{\text{e}}(\phi) + \rho_{\text{hh}}(\phi) + \rho_{\text{lh}}(\phi) + \rho_{\text{surf}} \tag{5.2}$$

includes the conduction electrons, the heavy/light holes, and the surface charges. We use the Thomas-Fermi approximation for a 3D electron gas to determine the mobile charge densities inside the InAs nanowire:

$$\begin{aligned}\rho_{\text{e}}(\phi) &= -\frac{e}{3\pi^2}\left(\frac{2m_{\text{e}}e\phi\theta(\phi)}{\hbar^2}\right)^{3/2},\\ \rho_{\text{hh/lh}}(\phi) &= \frac{e}{3\pi^2}\left(\frac{2m_{\text{hh/lh}}(-e\phi - E_g)\theta(-e\phi - E_g)}{\hbar^2}\right)^{3/2}\end{aligned} \tag{5.3}$$

where $m_{\text{e}} = 0.023\ m_0$, $m_{\text{hh}} = 0.41\ m_0$, $m_{\text{lh}} = 0.026\ m_0$ are the effective mass of the conduction electron, the heavy-hole and the light-hole in unit of electron mass, $E_g = 0.418$ eV is the band gap between conduction and valence bands [39], and $\theta(x)$ is the Heaviside step function. The surface charges are added to account for the band bending effect at both InAs/EuS and InAs/vacuum interfaces. At the two top facets of the InAs nanowire, where it is in contact with the EuS layer, a positive charge layer of 1 nm thickness and density $\rho_{\text{surf}} = 1.8\times10^{19}\ e/\text{cm}^3$ is added, leading to a band offset $W_{\text{InAs/EuS}} = 0.26$ eV. Similarly, at the three facets where the InAs nanowire is either in contact with vacuum or the dielectric layer, another 1 nm thick positive charge layer of density $\rho_{\text{surf}} = 1.3\times10^{19}\ e/\text{cm}^3$ is applied to model the band offset value $W_{\text{InAs/vac}} = 0.2$ eV [37, 40–42]. The band bending effect at the interface of InAs and the metallic aluminum layer is modeled by the Dirichlet boundary condition, i.e., $\phi = e^{-1}W_{\text{InAs/Al}} = 0.35$ V at the remaining one facet of the InAs nanowire. Additionally, the regions of the gates are also Dirichlet boundary conditions, with the values being determined by the applied voltage value, i.e., $\phi = V_i$, i =BG, LG, and RG. It is noteworthy that the treatment of the band bending effect at the InAs/EuS interface is unique to this work, and thus distinguishes our work from others [43]

5.3. ELECTRONIC PROPERTIES OF FERROMAGNETIC HYBRID NANOWIRES

5.3.1. MODEL HAMILTONIAN

The quantum model for investigating the electronic properties of the hybrid nanowire is shown in Fig. 5.1. We consider the two-dimensional cross section of the nanowire

(xy-plane), assuming translational symmetry along the wire axis (z-axis). The quantum system consists of only the InAs nanowire and the Al layer, which we treat on equal footing at the quantum mechanical level. We model the role of EuS as an induced exchange coupling term in InAs and Al, while neglecting the stray field from EuS [46]. The effects of gates, surface charges, dielectric layers, and the vacuum are taken into account via the self-consistently calculated electrostatic potential inside the InAs nanowire. Under these assumptions, the normal-state Hamiltonian for the ferromagnetic hybrid nanowire can be written as

$$\begin{aligned} H_{\mathrm{N}} =& \mathbf{p}^{\mathsf{T}} \frac{1}{2m(\mathbf{r})} \mathbf{p} + \alpha_R(\mathbf{r})(-i\partial_x \sigma_z - k_z \sigma_x) - E_F(\mathbf{r}) \\ & - e\phi(\mathbf{r}) + h_{\mathrm{ex}}(\mathbf{r})\sigma_z, \end{aligned} \tag{5.4}$$

where $\mathbf{p} = (-i\hbar\partial_x, -i\hbar\partial_y, \hbar k_z)$ is the momentum operator with $\hbar$ being the Planck constant, k_z the wave vector along the nanowire axis, σ_i the Pauli matrices acting on the spin space, $m(\mathbf{r})$ the effective mass, $\alpha_R(\mathbf{r})$ the strength of the Rashba spin-orbit coupling, $E_F(\mathbf{r})$ the Fermi energy, $\phi(\mathbf{r})$ the electrostatic potential, $e > 0$ the elementary charge, and $h_{\mathrm{ex}}(\mathbf{r})$ the strength of the induced exchange coupling due to the magnetic proximity effect from EuS. The physical parameters for InAs and Al are summarized in Table I. In addition, a random onsite potential is added within a distance of 2 nm from the outer surface of Al, modeling the effect of disorder induced by the amorphous oxide layer in realistic devices [31]. We assume that the disorder potential has strength $U_0 = 1$ eV with zero average, and is spatially uncorrelated, i.e., $\langle\langle \delta E_F(\mathbf{r}) \rangle\rangle = 0$, $\langle\langle \delta E_F(\mathbf{r}_i) \delta E_F(\mathbf{r}_j) \rangle\rangle = U_0^2/3 \cdot \delta_{ij}$, such that the bands in Al and InAs couple to each other strongly [31, 37].

When superconductivity is taken into consideration, the system is described by the Bogoliubov-de Gennes (BdG) Hamiltonian

$$\begin{aligned} H_{\mathrm{BdG}} =& \Big(\mathbf{p}^{\mathsf{T}} \frac{1}{2m(\mathbf{r})} \mathbf{p} + \alpha_R(\mathbf{r})(-i\partial_x \sigma_z - k_z \sigma_x) - E_F(\mathbf{r}) \\ & - e\phi(\mathbf{r}) \Big) \tau_z + h_{\mathrm{ex}}(\mathbf{r})\sigma_z + \Delta(\mathbf{r})\tau_x, \end{aligned} \tag{5.5}$$

in the basis of $(\psi_{\mathrm{e}\uparrow}, \psi_{\mathrm{e}\downarrow}, \psi_{\mathrm{h}\downarrow}, -\psi_{\mathrm{h}\uparrow})$. Here τ_i are the Pauli matrices acting on the Nambu space, and $\Delta(\mathbf{r})$ is the pairing potential in the superconductor.

For the numerical calculations, the Hamiltonians in Eqs. (5.4) and (5.5) are first discretized into a tight-binding model on a square lattice using the KWANT package [47]. We choose the lattice constants for InAs and Al to be 5 Å and 1 Å, respectively, to account for the large Fermi energy difference between the two materials. Then the eigenenergies and eigenstates are obtained by diagonalizing the sparse Hamiltonian matrices.

5.3.2. Exchange coupling in Al

We first investigate the effect of induced exchange coupling inside the aluminum layer on the electronic properties of the InAs/Al hybrid system. The origin of this exchange coupling is the magnetic proximity effect between the Al and EuS layers when they overlap with each other, as indicated in the schematic of Fig. 5.1. To model this proximity effect, we assume that $h_{\mathrm{ex}}(\mathbf{r}) = h_{\mathrm{ex}}^{\mathrm{Al}} > 0$ inside the Al layer. At this point we still neglect the magnetic proximity effect at the InAs/EuS interface; this will be discussed in the next section.

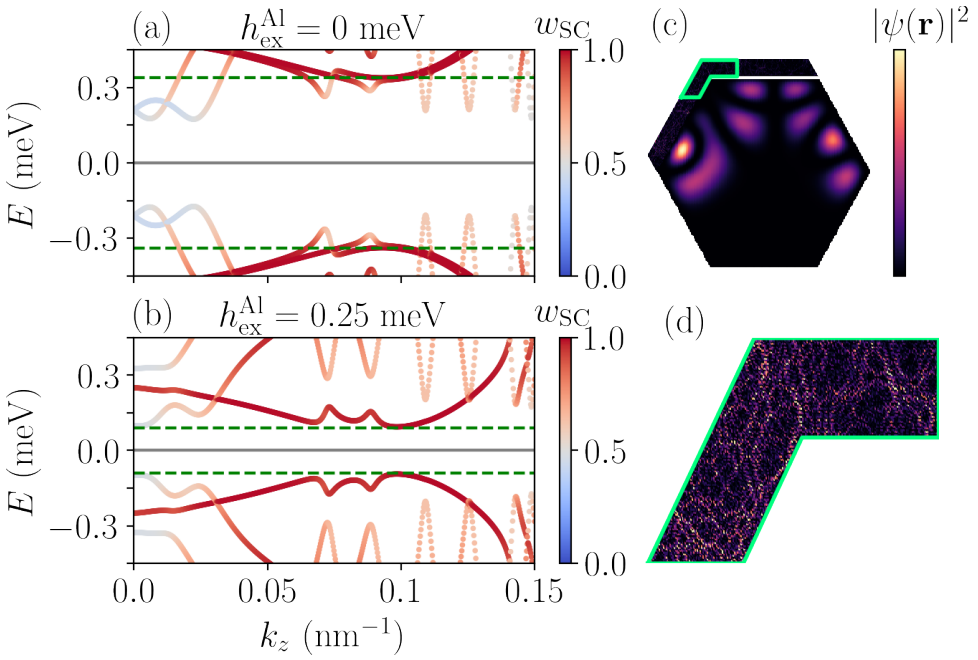

Figure 5.3: (a) and (b) BdG band diagrams for the InAs/Al hybrid nanowire in the absence and presence of the induced exchange coupling in Al. The gate voltages are fixed at $V_{BG} = -3.4$ V, $V_{LG} = V_{RG} = 0$ V. We note that a finite h_{ex}^{Al} lifts up the spin-orbit degeneracy at $k_z = 0$ in the hybrid state and reduces the continuum gap of the superconducting states. (c) wavefunction profile of the hybrid state at $k_z = 0$ and $E_{BdG} \approx 0.2$ meV with $h_{ex}^{Al} = 0$. (d) zoom-in of the wavefunction profile in the boxed region in Al (color scale adjusted).

Figures 5.3(a) and 5.3(b) show the BdG band diagrams of the InAs/Al hybrid system in the absence ($h_{ex}^{Al} = 0$ meV) and presence ($h_{ex}^{Al} = 0.25$ meV) of the induced exchange coupling in Al, with the gate voltages being fixed at $V_{BG} = -3.4$ V and $V_{LG} = V_{RG} = 0$ V. The color of the band indicates the degree of wavefunction hybridization, which is defined as $w_{SC} = \sum_{\mathbf{r}\in\Omega_{Al}} |\psi(\mathbf{r})|^2 \leq 1$, with Ω_{Al} denoting the volume of the Al layer. A finite h_{ex}^{Al} has two effects on the band properties of the hybrid nanowire.

First, a finite h_{ex}^{Al} would induce an effective Zeeman spin slitting for the hybrid state. As can be seen, the spin-orbit degeneracy at $k_z = 0$ and $E_{BdG} \approx 0.2$ meV in Fig. 5.3(a) for the hybrid state ($w_{SC} \approx 0.5$) is now lifted by the finite induced exchange coupling in Al in Fig. 5.3(b). The amplitude of the effective Zeeman energy is approximately

$$E_Z^{(1)} \approx w_{SC} \cdot h_{ex}^{Al}, \tag{5.6}$$

which is proportional to the weight of the wavefunction in Al. Figures 5.3(c) and 5.3(d) show the wavefunction profiles of the hybrid state in InAs and Al, respectively. Thereby, although InAs is not directly subject to the magnetic proximity effect from EuS in the physical scenario considered here, the hybrid state still gains a finite effective Zeeman spin splitting by distributing its wavefunction into the magnetized Al layer.

Second, the induced exchange coupling in Al would reduce the quasiparticle contin-

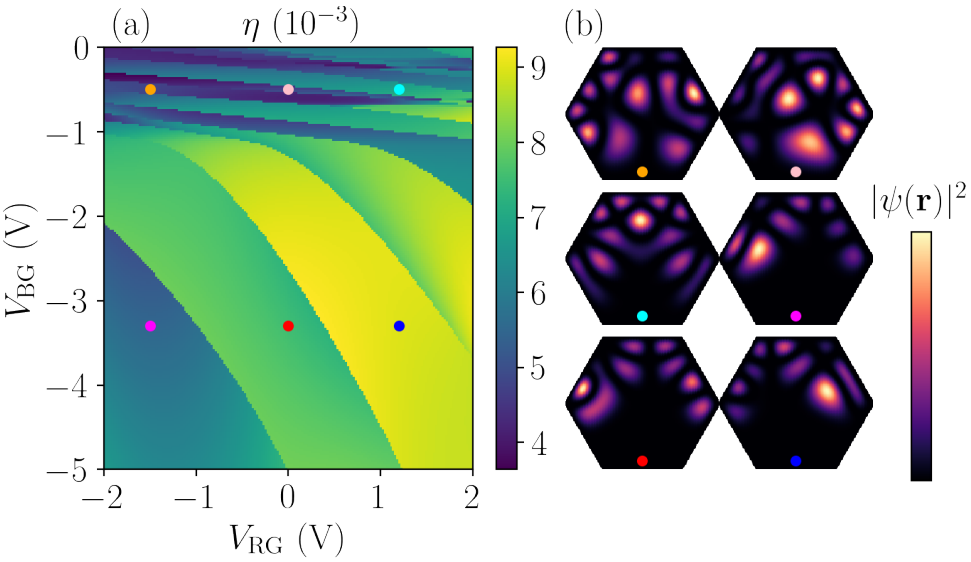

Figure 5.4: Magnetic proximity efficiency and wavefunction profiles in a bare InAs nanowire. (a) η of the normal eigenstate closest to the Fermi surface as a function of the backgate and the rightgate voltages. (b) $|\psi(\mathbf{r})|^2$ of the normal eigenstates at specific gate voltages.

uum gap. By comparing those superconducting states ($w_{SC} \approx 1$) in Figs. 5.3(a) and 5.3(b), we find that the excitation gap of the Al layer decreases from the bare value $\Delta_{qp} = 0.34$ meV to about $\Delta_{qp} \approx 0.09$ meV [green dashed lines in Figs. 5.3(a) and 5.3(b)]. Since Al is an *s*-wave BCS superconductivity, the quasiparticle continuum gap decreases with the induced exchange coupling in Al in a linear manner:

$$\Delta_{qp}(h_{ex}^{Al}) = \Delta_0 - h_{ex}^{Al}. \tag{5.7}$$

Thus we can estimate the strength of induced exchange coupling h_{ex}^{Al} from experimental data by considering the reduction of the quasiparticle continuum gap in Al. On the other hand, for the hybrid state ($w_{SC} \approx 0.5$), the k_F excitation gap (inverse of the localization length of the Majorana modes) at $k_z \approx 0.025\text{nm}^{-1}$ in Figs. 5.3(a) and 5.3(b) changes very little with h_{ex}^{Al}, possibly owing to the spin-orbit protection from InAs [48, 49].

When considering both of the abovementioned two effects on the InAs/Al hybrid nanowire, we conclude that an induced exchange coupling in Al alone *cannot* drive the hybrid system into the topological phase. Because by combining Eqs. (5.6) and (5.7), the induced effective Zeeman energy of the hybrid state is always less than the induced superconducting gap, i.e.,

$$E_Z^{(1)} < \Delta_{ind} \approx w_{SC}\Delta_0, \tag{5.8}$$

as long as the quasiparticle continuum gap in Al remains finite $\Delta_{qp}(h_{ex}^{Al}) > 0$. This is in agreement with a fundamental no-go theorem for topology for BdG Hamiltonians [50].

5.3.3. DIRECT MAGNETIC PROXIMITY EFFECT

We now focus on the direct magnetic proximity effect at the InAs/EuS interface and its dependence on gates, neglecting the superconducting shell completely. In particular for the quantum problem, we consider a bare InAs nanowire and the direct proximity effect is modeled phenomenologically as a local exchange coupling $h_{\rm ex}^{\rm InAs}\sigma_z$ within a distance $d = 1.5$ nm from the two-facet boundaries where InAs and EuS contact with each other. Here, the distance d is chosen to be about the penetration length of the wavefunction in a typical magnetic insulator [18], such that the magnitude of $h_{\rm ex}^{\rm InAs}$ can be approximated as the strength of the ferromagnetic coupling inside EuS. We have chosen for this phenomenological approach as the band structure of EuS may not be represented faithfully with an effective mass model as used for InAs and Al in our study. The effect of the back-gate and two side-gates is included via the electrostatic potential profile $\phi(\mathbf{r})$, which is calculated based on the geometry shown in Fig. 5.1. In order to quantify the magnetic proximity effect, we define the efficiency $\eta = [E_{n\uparrow}(k_z = 0) - E_{n\downarrow}(k_z = 0)]/2h_{\rm ex}^{\rm InAs}$, which is the Zeeman energy splitting of the n-th spinful subband in the presence of a unit-strength $h_{\rm ex}^{\rm InAs}$. $E_{n\sigma}$ is the energy eigenstate of the discretized normal Hamiltonian $H_{\rm N}$ in Eq. (5.4).

Figure 5.4(a) shows the calculated η of the normal subband mode closest to the Fermi surface as a function of the backgate and rightgate voltages (the leftgate dependence is weak due to the screening effect of Al). The efficiency η is a piecewise function of the gate voltages, with each piece corresponding to a particular subband mode. The η difference between distinct subband modes can be stark and dominates the η variations within a single subband mode. Note that although the dependence of η on the gate voltages is not monotonic, a general trend is that the subband mode at a more negative (positive) value of the backgate (rightgate) voltage would have a larger η, because their wavefunctions are more confined towards the InAs/EuS interface where the direct magnetic proximity effect is the strongest, as shown in Fig. 5.4(b).

The generalization from the bare InAs to the InAs/Al hybrid nanowire is straightforward. Namely, the effective Zeeman splitting for the hybrid state due to the direct magnetic proximity effect can be approximated as

$$E_Z^{(2)} \approx (1 - w_{\rm SC}) \cdot \eta \cdot h_{\rm ex}^{\rm InAs}, \tag{5.9}$$

where the prefactor $(1 - w_{\rm SC})$ accounts for the semiconductor-superconductor hybridization. In the absence of other mechanisms of inducing Zeeman splitting, the minimal strength of the exchange coupling for realizing TSC would be about $h_{\rm ex,min}^{\rm InAs} = \frac{w_{\rm SC}\Delta_0}{(1-w_{\rm SC})\eta}$ by requiring $E_Z^{(2)} = \Delta_{\rm ind}$. For a typical device with strong coupling at both InAs/Al and InAs/EuS interfaces, e.g., $w_{\rm SC} \approx 0.5$ and $\eta \approx 7 \times 10^{-3}$ [see Fig. 5.4(a)], we have $h_{\rm ex,c}^{\rm InAs} \approx 50$ meV. Such a large strength of exchange coupling sets a demanding requirement for the proximity magnetic insulator candidates.

5.3.4. TOPOLOGICAL PHASE DIAGRAM

We now consider the scenario in which the InAs/Al hybrid nanowire is subject to the joint magnetic proximity effect from both Al/EuS and InAs/EuS interfaces, and study the topological phase diagrams as a function of gate voltages and exchange couplings. Namely, the induced exchange coupling is finite both in Al and at the boundaries of InAs,

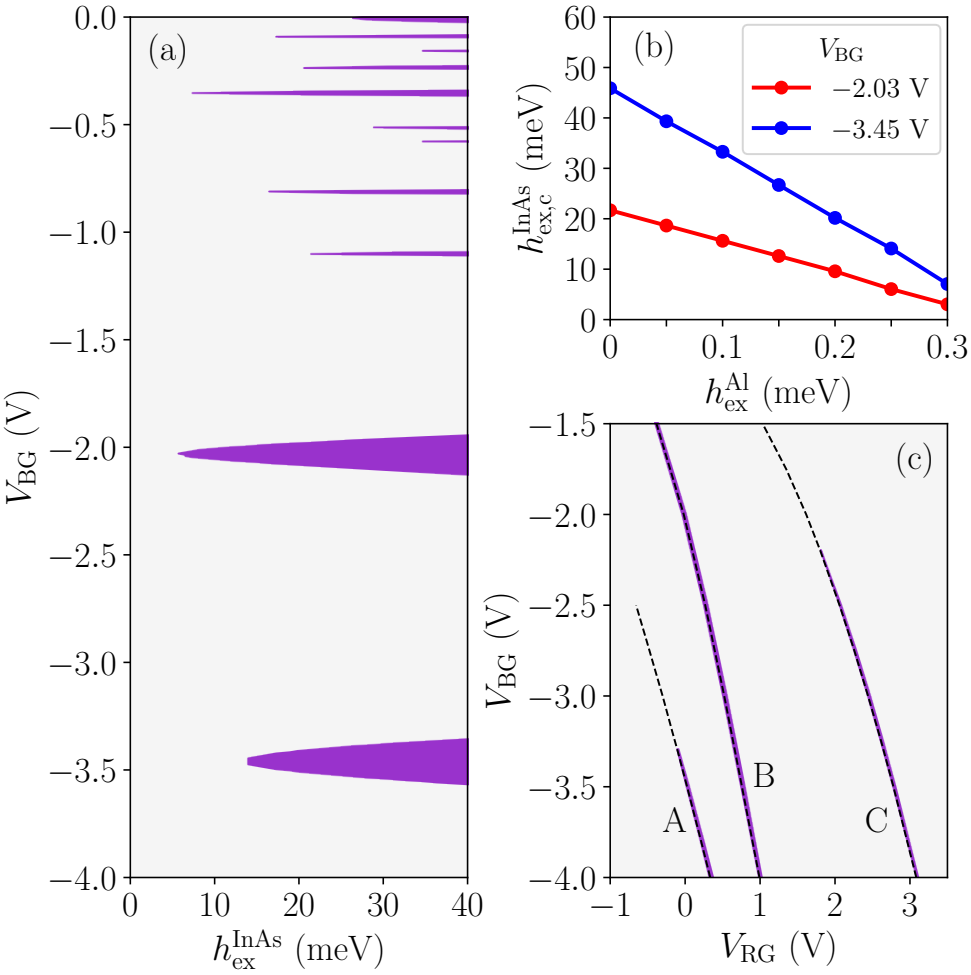

Figure 5.5: (a) Topological phase diagram in (h_{ex}^{InAs}, V_{BG}) with h_{ex}^{Al} = 0.25 meV, and V_{LG} = V_{RG} = 0 V. The area in purple represents the topological phase of the hybrid nanowire, while that in grey represents the trivial phase. (b) Minimally required exchange coupling at the InAs/EuS interface for realizing TSC as a function of the strength of the induced exchange coupling in Al. The two lines correspond to the topological phases in (a) at V_{BG} = −2.03 V and −3.45 V. (c) Topological phase diagram in (V_{RG}, V_{BG}) with h_{ex}^{Al} = 0.25 meV, h_{ex}^{InAs} = 15 meV, and V_{LG} = 0 V.

and thereby the total effective Zeeman spin splitting now is the combined contribution of two mechanisms:

$$E_Z^{\rm tot}(h_{\rm ex}^{\rm Al}, h_{\rm ex}^{\rm InAs}) = E_Z^{(1)}(h_{\rm ex}^{\rm Al}) + E_Z^{(2)}(h_{\rm ex}^{\rm InAs}), \tag{5.10}$$

where $E_Z^{(1)}$ and $E_Z^{(2)}$ are estimated in Eqs. (5.6) and (5.9). To determine the topological phase diagram of the hybrid nanowire, we keep track of the energy gap $E_{\rm BdG}(k_z = 0)$. For semiconductor-superconductor nanowires, the closing and reopening of $E_{\rm BdG}(k_z = 0)$ signifies the topological quantum phase transition [15–18]. Figure 5.5(a) shows the topological phase diagram of the device in Fig. 5.1 as a function of the backgate voltage $V_{\rm BG}$ and the exchange coupling $h_{\rm ex}^{\rm InAs}$ in InAs, with other parameters being fixed at $h_{\rm ex}^{\rm Al} = 0.25$ meV, and $V_{\rm LG} = V_{\rm RG} = 0$ V. The areas in purple represent the topological phase of the nanowire, while those in grey represent the trivial phase. There are several observations on the result in Fig. 5.5(a). First, the pattern of the phase diagram resembles those of the hybrid nanowires for which the Zeeman energy is induced by an applied magnetic field but without including the orbital effect from the field. Because in our model, the Zeeman energy is induced by the exchange couplings at zero magnetic field. Second, the TSC phases (lobes in purple) at $V_{\rm RG} < -1.5$ V are more robust, based on the fact that they have a smaller critical exchange coupling strength, and a larger width along $V_{\rm BG}$. The robustness is the consequence of the joint effect of a larger direct magnetic proximity effect ($\eta > 7 \times 10^{-3}$ as shown in Fig. 5.4) and a stronger InAs/Al hybridization ($w_{\rm SC} \approx 0.5$ as shown in Fig. 5.3) at more negative gate voltages. Third, the minimal strength of the critical exchange field $h_{\rm ex,c}^{\rm InAs}$ for achieving topological phases is about 10 meV for the two lobes at $V_{\rm RG} \approx -2$ V and -3.5 V. Such a strength of $h_{\rm ex,c}^{\rm InAs}$ at the InAs/EuS interface is comparable to the estimated strength of exchange coupling at the interface of III-V compounds and magnetic insulators, which confirms the feasibility to realize TSC in semiconductor-superconductor-ferromagnetic hybrid nanowires with overlapping Al and EuS layers. This is one of the central result in the current work.

Figure 5.5(b) shows the minimally required strength of $h_{\rm ex,c}^{\rm InAs}$ at the InAs/EuS interface as a function of $h_{\rm ex}^{\rm Al}$ in Al for two particular subband modes. The minimal strength $h_{\rm ex,c}^{\rm InAs}$ decreases linearly with an increasing $h_{\rm ex}^{\rm Al}$, because an larger effective Zeeman energy $E_Z^{(1)} \propto h_{\rm ex}^{\rm Al}$ facilitates the realization of topological superconductivity in the hybrid nanowire. In particular, the minimally required exchange coupling at the InAs/EuS interface is about $h_{\rm ex,c}^{\rm InAs} \sim$50 or 20 meV if no exchange coupling is induced in Al. This value reduces significantly to $h_{\rm ex,c}^{\rm InAs} \lesssim 10$ or 5 meV as $h_{\rm ex}^{\rm Al} \approx 0.28$ meV. Here for comparison between theory and experiment, the value of $h_{\rm ex}^{\rm Al}$ is chosen such that the shrinking of the continuum gap is comparable to the observations in Ref. [30], i.e., the gap in devices with overlapping Al and EuS layers is $\sim 0.04/0.23$ of the gap in non-overlapping ones. If we assume that the properties of a hybrid nanowire with non-overlapping Al and EuS layers are approximately captured by setting $h_{\rm ex}^{\rm Al} = 0$ in our model, Fig. 5.5(b) explains why zero-bias conductance peaks in the tunnel spectroscopy are only observed in overlapping devices in Ref. [30].

Figure 5.5(c) shows the topological phase diagram in the ($V_{\rm RG}$, $V_{\rm BG}$) plane, focusing on the three topological lobes at $V_{\rm BG} < -1.5$ V. Now the exchange couplings are fixed at $h_{\rm ex}^{\rm InAs} = 15$ meV and $h_{\rm ex}^{\rm Al} = 0.25$ meV, and gate voltages $V_{\rm LG} = 0$ V. The topological phase

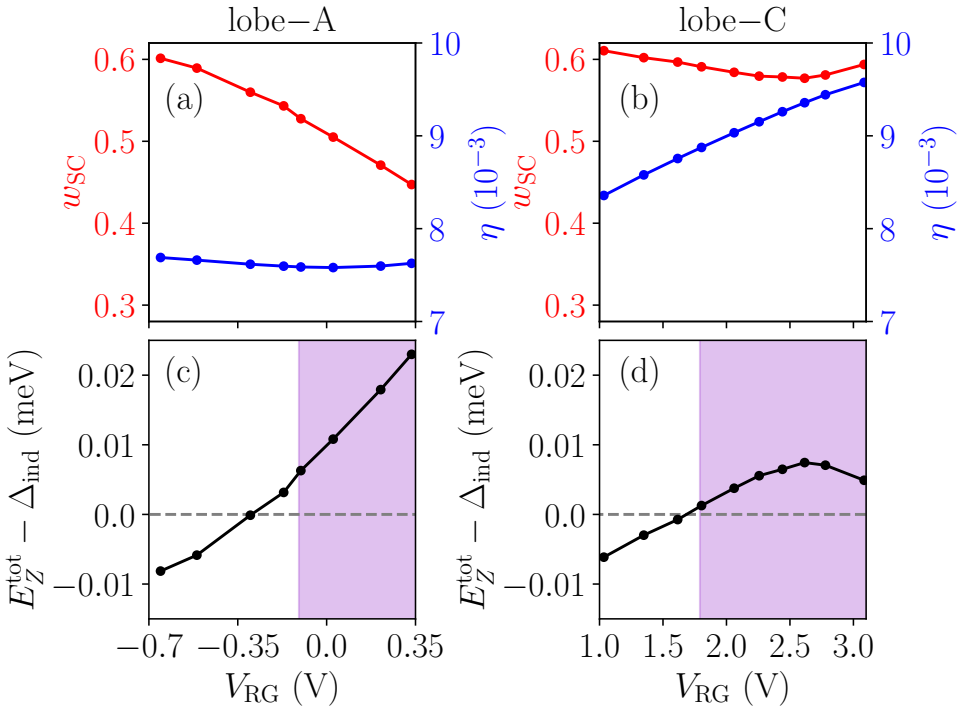

Figure 5.6: (a) w_{SC} and η of lobe-A along the zero-Fermi-energy line [dashed lines in Fig. 5.5(c)]. Here the variation of w_{SC} has a dominant effect over η in determining the topological phase of the hybrid state. (c) Calculated $E_Z^{tot} - \Delta_{ind}$ (black dots) of lobe-A. Ideally, the hybrid state at zero Fermi energy becomes topological when $E_Z^{tot} - \Delta_{ind}$ is greater than zero. The purple shaded area represents the topological phase indicated in Fig. 5.5(c). (b) and (d) Similar to (a) and (c) for lobe-C. For lobe-C, the change of η is larger than w_{SC}, and the hybrid state becomes topological when the direct magnetic proximity effect is prominent ($\eta > 9 \times 10^{-3}$).

shows up as a diagonal line, along which the Fermi energy of the relevant subband mode keeps close to zero. Note that the hybrid state of the particular subband mode can remain topological all the way along the diagonal zero-Fermi-energy line (e.g., the continuous lobe-B), or it can transform between topologically trivial and nontrivial phases (e.g., lobes-A or -C). It turns out that the topology along the zero-Fermi-energy line depends crucially on how the semiconductor-superconductor hybridization (w_{SC}) and direct magnetic proximity efficiency (η) respond to the gate voltage variations. For the hybrid state with zero Fermi energy, we can use a simplified criterion in the form

$$\begin{aligned} & E_Z^{tot} - \Delta_{ind} \\ =& E_Z^{(2)} - \left(\Delta_{ind} - E_Z^{(1)}\right) \\ =& (1 - w_{SC}) \cdot \eta \cdot h_{ex}^{InAs} - w_{SC}(\Delta_0 - h_{ex}^{Al}) > 0, \end{aligned} \tag{5.11}$$

based on the definitions in Eqs. (5.6), (5.8), (5.9) and (5.10). In Eq. (5.11), the relative strength of Zeeman energy due to the direct magnetic proximity effect $E_Z^{(2)}$ and the

induced quasiparticle continuum gap $w_{\mathrm{SC}}(\Delta_0 - h_{\mathrm{ex}}^{\mathrm{Al}})$ depend on w_{SC} and η explicitly.

Figure 5.6 shows the w_{SC} and η of the lobes-A and -C along the zero-Fermi-energy line, i.e., the dashed lines in Fig. 5.5(c). In Fig. 5.6(a), the variation of w_{SC} dominates that of η, and the hybrid state is topological [see Fig. 5.6(c)] when the hybridization is moderately small, i.e., $w_{\mathrm{SC}} \lesssim 0.5$. As indicated by Eq. (5.11), a smaller degree of semiconductor-superconductor hybridization means a stronger $E_Z^{(2)}$ from the InAs side and a smaller induced continuum gap from Al, making it easier to satisfy the topological criterion. In another scenario, as shown by Fig. 5.6(b) for lobe-C, η increases monotonically as the voltage of the right-gate becomes more positive, and has a dominant effect than w_{SC}. The hybrid state becomes topological when η is sufficiently large. We thus see that depending on the details of a subband, a topological transition can be driven by two gates by both changing the induced superconducting gap or the directly induced Zeeman splitting. This is in contrast to the usual topological phase transition driven by changing the chemical potential by a gate.

5.4. SUMMARY

In this work, we studied the electronic properties of InAs/EuS/Al hybrid nanowires. We analyzed the band bending at the InAs/EuS interface using ARPES data and found that this interface enhances electron accumulation compared to a bare InAs surface. Using this input, we performed microscopic electrostatics and device simulations. From these we concluded that it is feasible to achieve topological superconductivity in the device geometry shown in Fig. 5.1, within the realistic parameters: the calculated minimal strength of $h_{\mathrm{ex}}^{\mathrm{InAs}}$ at the InAs/EuS interface is about 10 meV, consistent with the induced exchange coupling between III-V semiconductors and magnetic insulators. Our calculations also indicate that in experiments a topological phase is only achieved by the combination of both an induced Zeeman splitting in the superconducting Al shell by EuS, and an induced Zeeman splitting directly at the InAs/EuS interface. We also find in this hybrid device additional ways to control the topological phase by gates compared to the well-known control by changing the chemical potential: Topology can be controlled using two gates either by changing the effective induced superconducting gap or by changing the overlap of the wave function with the InAs/EuS interface and thus the directly induced Zeeman splitting. This gives new avenues to experimentally optimizing topological phases in a given device geometry.

While finishing this work we became aware of a similar study on InAs/EuS/Al nanodevices focusing on electrostatic effects [43]. That work concludes, opposite to our findings, that only the directly induced Zeeman splitting is necessary for a topological phase. The reason for this discrepancy is that Ref. [43] only assumes electron accumulation due to the work function difference between Al and InAs, and not at the InAs/EuS interface, contrary to our experimental finding. We note that there is concurrent work on the effects of electrostatics in these hybrid systems [51]. Also, there are concurrent efforts to go beyond the effective model as used in our work, and do a self-consistent treatment of proximity effect between EuS and Al when the shells overlap [52].

ACKNOWLEDGEMENTS

We are grateful to Aleksei Khindanov, Andrey E. Antipov, William S. Cole, Bernard van Heck for discussions at the initial stage of this project. We would like to thank Anton Akhmerov, Artem Pulkin, Haining Pan, and F. Setiawan for useful comments on the manuscript. C.-X.L. thanks Zhenglu Li, Qisi Wang for helpful discussions. S.S., Y.L. and P.K. would like to acknowledge J. Krieger and V. Strocov from the ADDRESS beamline at the Swiss Light Source, PSI, Switzerland. This work was supported by a subsidy for top consortia for knowledge and innovation (TKl toeslag), by the European Union's Horizon 2020 research and innovation programme FETOpen Grant No. 828948 (AndQC), by Microsoft Quantum, by the European Union's Horizon 2020 research and innovation programme under grant numbers 716655 (ERC Stg HEMs-DAM), by the international training network "INDEED" (grant agreement no. 722176), and by São Paulo Research Foundation, grants 2016/10167-8 and 2019/07082-9.

AUTHOR CONTRIBUTIONS.

C.-X.L. proposed the idea of microscopic device simulation and initiated the project, the scope of the project was later refined using contributions from all authors. C.-X.L., K.V., and A.M. performed an extensive survey on the appropriate model of the hybrid nanowire. C.-X.L. conceived the model in this work, implemented the numerical methods, and performed the numerical calculations. S.S., Y.L. and P.K. carried out the data analysis for band bending at the InAs/EuS interface. M.W. supervised the project. All authors discussed the results. C.-X.L. and M. W. wrote the manuscript with input from all authors.

REFERENCES

[1] C. Nayak, S. H. Simon, A. Stern, M. Freedman, and S. Das Sarma, *Non-Abelian anyons and topological quantum computation,* Rev. Mod. Phys. **80**, 1083 (2008).

[2] J. Alicea, *New directions in the pursuit of Majorana fermions in solid state systems,* Rep. Prog. Phys. **75**, 076501 (2012).

[3] M. Leijnse and K. Flensberg, *Introduction to topological superconductivity and Majorana fermions,* Semicond. Sci. Technol. **27**, 124003 (2012).

[4] C. Beenakker, *Search for Majorana fermions in superconductors,* Annu. Rev. Condens. Matter Phys. **4**, 113 (2013).

[5] T. D. Stanescu and S. Tewari, *Majorana fermions in semiconductor nanowires: fundamentals, modeling, and experiment,* J. Phys.: Condens. Matter **25**, 233201 (2013).

[6] J.-H. Jiang and S. Wu, *Non-Abelian topological superconductors from topological semimetals and related systems under the superconducting proximity effect,* J. Phys.: Condens. Matter **25**, 055701 (2013).

[7] S. R. Elliott and M. Franz, *Colloquium: Majorana fermions in nuclear, particle, and solid-state physics,* Rev. Mod. Phys. **87**, 137 (2015).

[8] S. D. Sarma, M. Freedman, and C. Nayak, *Majorana zero modes and topological quantum computation,* Npj Quantum Information **1**, 15001 EP (2015).

[9] M. Sato and S. Fujimoto, *Majorana fermions and topology in superconductors,* J. Phys. Soc. Jpn. **85**, 072001 (2016).

[10] M. Sato and Y. Ando, *Topological superconductors: a review,* Rep. Prog. Phys. **80**, 076501 (2017).

[11] R. Aguado, *Majorana quasiparticles in condensed matter,* Riv. Nuovo Cimento **40**, 523 (2017).

[12] R. M. Lutchyn, E. P. A. M. Bakkers, L. P. Kouwenhoven, P. Krogstrup, C. M. Marcus, and Y. Oreg, *Majorana zero modes in superconductor–semiconductor heterostructures,* Nat. Rev. Mater. **3**, 52 (2018).

[13] H. Zhang, D. E. Liu, M. Wimmer, and L. P. Kouwenhoven, *Next steps of quantum transport in Majorana nanowire devices,* Nature Communications **10**, 5128 (2019).

[14] S. M. Frolov, M. J. Manfra, and J. D. Sau, *Topological superconductivity in hybrid devices,* Nature Physics **16**, 718 (2020).

[15] J. D. Sau, R. M. Lutchyn, S. Tewari, and S. Das Sarma, *Generic new platform for topological quantum computation using semiconductor heterostructures,* Phys. Rev. Lett. **104**, 040502 (2010).

[16] R. M. Lutchyn, J. D. Sau, and S. Das Sarma, *Majorana fermions and a topological phase transition in semiconductor-superconductor heterostructures,* Phys. Rev. Lett. **105**, 077001 (2010).

[17] Y. Oreg, G. Refael, and F. von Oppen, *Helical liquids and Majorana bound states in quantum wires,* Phys. Rev. Lett. **105**, 177002 (2010).

[18] J. D. Sau, S. Tewari, R. M. Lutchyn, T. D. Stanescu, and S. Das Sarma, *Non-Abelian quantum order in spin-orbit-coupled semiconductors: Search for topological Majorana particles in solid-state systems,* Phys. Rev. B **82**, 214509 (2010).

[19] V. Mourik, K. Zuo, S. M. Frolov, S. Plissard, E. P. A. M. Bakkers, and L. P. Kouwenhoven, *Signatures of Majorana fermions in hybrid superconductor-semiconductor nanowire devices,* Science **336**, 1003 (2012).

[20] A. Das, Y. Ronen, Y. Most, Y. Oreg, M. Heiblum, and H. Shtrikman, *Zero-bias peaks and splitting in an Al-InAs nanowire topological superconductor as a signature of Majorana fermions,* Nat. Phys. **8**, 887 (2012).

[21] M. T. Deng, C. L. Yu, G. Y. Huang, M. Larsson, P. Caroff, and H. Q. Xu, *Anomalous zero-bias conductance peak in a Nb-InSb nanowire-Nb hybrid device,* Nano Lett. **12**, 6414 (2012).

[22] H. O. H. Churchill, V. Fatemi, K. Grove-Rasmussen, M. T. Deng, P. Caroff, H. Q. Xu, and C. M. Marcus, *Superconductor-nanowire devices from tunneling to the multichannel regime: Zero-bias oscillations and magnetoconductance crossover,* Phys. Rev. B **87**, 241401(R) (2013).

[23] A. D. K. Finck, D. J. Van Harlingen, P. K. Mohseni, K. Jung, and X. Li, *Anomalous modulation of a zero-bias peak in a hybrid nanowire-superconductor device,* Phys. Rev. Lett. **110**, 126406 (2013).

[24] S. Albrecht, A. Higginbotham, M. Madsen, F. Kuemmeth, T. Jespersen, J. Nygård, P. Krogstrup, and C. Marcus, *Exponential protection of zero modes in Majorana islands,* Nature **531**, 206 (2016).

[25] J. Chen, P. Yu, J. Stenger, M. Hocevar, D. Car, S. R. Plissard, E. P. A. M. Bakkers, T. D. Stanescu, and S. M. Frolov, *Experimental phase diagram of zero-bias conductance peaks in superconductor/semiconductor nanowire devices,* Science Advances **3** (2017), 10.1126/sciadv.1701476.

[26] M. T. Deng, S. Vaitiekenas, E. B. Hansen, J. Danon, M. Leijnse, K. Flensberg, J. Nygård, P. Krogstrup, and C. M. Marcus, *Majorana bound state in a coupled quantum-dot hybrid-nanowire system,* Science **354**, 1557 (2016).

[27] H. Zhang, Ö. Gül, S. Conesa-Boj, M. Nowak, M. Wimmer, K. Zuo, V. Mourik, F. K. de Vries, J. van Veen, M. W. A. de Moor, J. D. S. Bommer, D. J. van Woerkom, D. Car, S. R. Plissard, E. P. A. M. Bakkers, M. Quintero-Pérez, M. C. Cassidy, S. Koelling, S. Goswami, K. Watanabe, T. Taniguchi, and L. P. Kouwenhoven, *Ballistic superconductivity in semiconductor nanowires,* Nature Communications **8**, 16025 EP (2017).

[28] Ö. Gül, H. Zhang, J. D. S. Bommer, M. W. A. de Moor, D. Car, S. R. Plissard, E. P. A. M. Bakkers, A. Geresdi, K. Watanabe, T. Taniguchi, and L. P. Kouwenhoven, *Ballistic Majorana nanowire devices,* Nat. Nanotechnol. **13**, 192 (2018).

[29] F. Nichele, A. C. C. Drachmann, A. M. Whiticar, E. C. T. O'Farrell, H. J. Suominen, A. Fornieri, T. Wang, G. C. Gardner, C. Thomas, A. T. Hatke, P. Krogstrup, M. J. Manfra, K. Flensberg, and C. M. Marcus, *Scaling of Majorana zero-bias conductance peaks,* Phys. Rev. Lett. **119**, 136803 (2017).

[30] S. Vaitiekėnas, Y. Liu, P. Krogstrup, and C. M. Marcus, *Zero-bias peaks at zero magnetic field in ferromagnetic hybrid nanowires,* Nature Physics (2020), 10.1038/s41567-020-1017-3.

[31] A. E. Antipov, A. Bargerbos, G. W. Winkler, B. Bauer, E. Rossi, and R. M. Lutchyn, *Effects of gate-induced electric fields on semiconductor Majorana nanowires,* Phys. Rev. X **8**, 031041 (2018).

[32] A. E. G. Mikkelsen, P. Kotetes, P. Krogstrup, and K. Flensberg, *Hybridization at superconductor-semiconductor interfaces,* Phys. Rev. X **8**, 031040 (2018).

[33] S. Schuwalow, N. Schroeter, J. Gukelberger, C. Thomas, V. Strocov, J. Gamble, A. Chikina, M. Caputo, J. Krieger, G. C. Gardner, *et al.*, *Band bending profile and band offset extraction at semiconductor-metal interfaces,* arXiv:1910.02735 (2019).

[34] Y. Liu, A. Luchini, S. Martí-Sánchez, C. Koch, S. Schuwalow, S. A. Khan, T. Stankevič, S. Francoual, J. R. L. Mardegan, J. A. Krieger, V. N. Strocov, J. Stahn, C. A. F. Vaz, M. Ramakrishnan, U. Staub, K. Lefmann, G. Aeppli, J. Arbiol, and P. Krogstrup, *Coherent epitaxial semiconductor–ferromagnetic insulator InAs/EuS interfaces: Band alignment and magnetic structure,* ACS Applied Materials & Interfaces **12**, 8780 (2020).

[35] A. Vuik, D. Eeltink, A. R. Akhmerov, and M. Wimmer, *Effects of the electrostatic environment on the Majorana nanowire devices,* New Journal of Physics **18**, 033013 (2016).

[36] B. D. Woods, T. D. Stanescu, and S. Das Sarma, *Effective theory approach to the Schrödinger-Poisson problem in semiconductor Majorana devices,* Phys. Rev. B **98**, 035428 (2018).

[37] G. W. Winkler, A. E. Antipov, B. van Heck, A. A. Soluyanov, L. I. Glazman, M. Wimmer, and R. M. Lutchyn, *Unified numerical approach to topological semiconductor-superconductor heterostructures,* Phys. Rev. B **99**, 245408 (2019).

[38] P. Armagnat, A. Lacerda-Santos, B. Rossignol, C. Groth, and X. Waintal, *The self-consistent quantum-electrostatic problem in strongly non-linear regime,* SciPost Phys. **7**, 31 (2019).

[39] R. Winkler, S. Papadakis, E. De Poortere, and M. Shayegan, *Spin-Orbit Coupling in Two-Dimensional Electron and Hole Systems*, Vol. 41 (Springer, 2003).

[40] L. O. Olsson, C. B. M. Andersson, M. C. Håkansson, J. Kanski, L. Ilver, and U. O. Karlsson, *Charge accumulation at InAs surfaces,* Phys. Rev. Lett. **76**, 3626 (1996).

[41] V. E. Degtyarev, S. V. Khazanova, and N. V. Demarina, *Features of electron gas in InAs nanowires imposed by interplay between nanowire geometry, doping and surface states,* Scientific Reports **7**, 3411 (2017).

[42] B. D. Woods, S. Das Sarma, and T. D. Stanescu, *Subband occupation in semiconductor-superconductor nanowires,* Phys. Rev. B **101**, 045405 (2020).

[43] B. D. Woods and T. D. Stanescu, *Electrostatic effects and topological superconductivity in semiconductor-superconductor-magnetic insulator hybrid wires,* arXiv:2011.01933 (2020).

[44] M. Gmitra and J. Fabian, *First-principles studies of orbital and spin-orbit properties of GaAs, GaSb, InAs, and InSb zinc-blende and wurtzite semiconductors,* Phys. Rev. B **94**, 165202 (2016).

[45] J. F. Cochran and D. E. Mapother, *Superconducting transition in aluminum,* Phys. Rev. **111**, 132 (1958).

[46] Y. Liu, S. Vaitiekėnas, S. Martí-Sánchez, C. Koch, S. Hart, Z. Cui, T. Kanne, S. A. Khan, R. Tanta, S. Upadhyay, M. E. Cachaza, C. M. Marcus, J. Arbiol, K. A. Moler, and P. Krogstrup, *Semiconductor–ferromagnetic insulator–superconductor nanowires: Stray field and exchange field, Nano Letters*, Nano Letters **20**, 456 (2020).

[47] C. W. Groth, M. Wimmer, A. R. Akhmerov, and X. Waintal, *Kwant: a software package for quantum transport,* New Journal of Physics **16**, 063065 (2014).

[48] J. D. S. Bommer, H. Zhang, O. Gül, B. Nijholt, M. Wimmer, F. N. Rybakov, J. Garaud, D. Rodic, E. Babaev, M. Troyer, D. Car, S. R. Plissard, E. P. A. M. Bakkers, K. Watanabe, T. Taniguchi, and L. P. Kouwenhoven, *Spin-orbit protection of induced superconductivity in Majorana nanowires,* Phys. Rev. Lett. **122**, 187702 (2019).

[49] C.-X. Liu, J. D. Sau, T. D. Stanescu, and S. Das Sarma, *Conductance smearing and anisotropic suppression of induced superconductivity in a Majorana nanowire,* Phys. Rev. B **99**, 024510 (2019).

[50] K. Pöyhönen, D. Varjas, M. Wimmer, and A. Akhmerov, *Minimal zeeman field requirement for a topological transition in superconductors,* SciPost Physics **10** (2021), 10.21468/scipostphys.10.5.108.

[51] A. L. Yeyati and E. Prada, Private communication and `https://youtu.be/vmSYmj_vqk8?t=2669`.

[52] A. Antipov, Private communication.

6

SCATTERING MATRIX REDUCTION WITHIN THE SHORT JUNCTION APPROXIMATION

This chapter is an unpublished work in progress.

6.1. INTRODUCTION

The ability of a superconductor to induce superconducting behaviour in adjacent materials [1–3], known as the superconducting proximity effect, is an invaluable tool for engineering quantum states in mesoscopic structures. It is the key method that allows the exploration of novel quantum materials by combining materials with different properties. In particular, it is used for the creation of Majorana zero modes in systems such as semiconductor heterostructures [4] and YSR chains [5].

However, modelling the proximity effect numerically is a challenging task. To capture the phenomena correctly, one needs to consider a large superconductor such that bound state wavefunctions sufficiently decay into it. In two dimensions and more this task becomes computationally intractable. While there are efficient bound-state energy algorithms which eliminate the superconductor leads [6, 7], the problem definition is still non-linear. On the other hand, modelling the superconductor through the short-junction approximation [8] allows us to express the problem as a linear eigenvalue problem which utilizes the scattering matrix of the superconductor lead. However, the method relies on finding all the modes in the superconductor which becomes expensive in the case that the number of modes within the superconductor is much larger than the number of modes in the scattering region.

In this paper, we further reduce the computational complexity of the short-junction approximation by reducing the scattering matrix of the superconductor to a smaller matrix which only contains the modes that couple to the scattering region. We do so by developing the concept of virtual leads — eigenmodes of the current operator — which decouple the scattering region from the superconductor. We demonstrate the efficiency of our method by calculating the dispersion of a YSR chain.

6.2. SHORT JUNCTION THEORY

We consider a magnetic impurity H_i that is connected to a large superconducting lead. In the case that the superconductor coherence length is much larger than the distance between the superconductor and the impurity, $\chi \gg L$, the dynamical phase of the bound state becomes negligible. This limit is known as the short junction limit and allows us to model the superconductor as a boundary condition on the impurity [8]:

$$\begin{aligned} \begin{pmatrix} 0 & -iA^\dagger \\ iA & 0 \end{pmatrix} \Psi &= \frac{E}{\Delta}\Psi, \\ A &= \frac{1}{2}\left(r_A S - S^T r_A\right), \end{aligned} \tag{6.1}$$

where S is the normal state scattering matrix in the case that superconducting lead was metallic and r_A is the Andreev reflection matrix. Whenever time-reversal symmetry holds, the Andreev reflection couples electrons and holes which are time-reversed partners. Therefore, we choose a basis such that the outgoing modes are the time-reversed partners of the incoming ones which gives a diagonal Andreev reflection matrix $r_A = i$, and simplifies the Eq. (6.1) to:

$$\begin{pmatrix} 0 & \left(S^T - S\right)^\dagger \\ S^T - S & 0 \end{pmatrix} \Psi = \frac{E}{\Delta}\Psi. \tag{6.2}$$

However, to obtain S, we are required to simulate a dense metallic lead which is expensive and redundant because a portion of the modes usually do not couple to the bound state. To distinguish the modes that couple to the bound state, we partition the impurity from the superconducting leads by inserting in-between them an auxiliary pair of leads whose modes are current eigenmodes — a construction we refer to as virtual leads. By passing current through the virtual leads, we identify the modes that propagate between the impurity and the superconductor. We then take the resulting scattering matrix between virtual leads and the superconductor, relate it to the original scattering matrix S and perform a polar decomposition [9] to remove the redundant modes which do not couple to the bound states.

6.3. VIRTUAL LEADS

Consider a tight-binding system composed of a finite system A and a semi-infinite lead B connected through a hopping matrix V:

$$\hat{H}_{\text{sys}} = \begin{pmatrix} H_A & V & & & & \\ V^\dagger & H_B & V_B & & & \\ & V_B^\dagger & H_B & V_B & & \\ & & V_B^\dagger & H_B & V_B & \\ & & & \ddots & \ddots & \ddots \end{pmatrix}, \tag{6.3}$$

where H_A and H_B are the Hamiltonians of A and B unit cells and V_B is the hopping between the lead B unit cells. In the eigenbasis of leads B, the Eq. (6.3) defines the scattering problem for a scattering matrix S that relates the incoming and outgoing propagating waves of lead B. Rather than solve the full scattering problem, we wish to decouple the two systems into two independent sub-problems. Such decoupling is beneficial because it allows us to:

- solve the scattering problem for the system A (B) and hopping V independently of the system B (A).
- take advantage of symmetries in system A (B) and hopping V which may not be present in the system B (A).

A standard way to decouple the systems is through the self-energy $\Sigma_{A(B)}$ which encodes the system $A(B)$. We propose an alternative method to decouple the systems through the use of virtual leads inserted between the system A and B. The method is equivalent and dual to the recursive Green's function method in the sense that it encodes the system $A(B)$ in the scattering matrix $S_{A(B)}$ rather than the self-energy $\Sigma_{A(B)}$.

Our goal is to split the systems A and B into two distinct scattering problems. To achieve this, we consider the tight-binding equations in Eq. (6.3) at the intersection of the two systems:

$$(H_A - E)\psi_A + V\psi_{B,1} = 0, \tag{6.4}$$

$$V^\dagger\psi_A + (H_B - E)\psi_B + V_B\psi_{B,2} = 0, \tag{6.5}$$

where ψ_A and $\psi_{B,1}$ are the wavefunction amplitudes in the system A and the first unit cell of lead B respectively. Because the hopping matrix V in Eqs. (6.4) and (6.5) is not diagonal, the current operator $\hat{I}$ mixes different A and B channels together:

$$\begin{aligned}\langle\psi|\hat{I}|\psi\rangle = \begin{pmatrix}\psi_A\\ \psi_{B,1}\end{pmatrix}^\dagger \hat{I}\begin{pmatrix}\psi_A\\ \psi_{B,1}\end{pmatrix} = \\ \begin{pmatrix}\psi_A\\ \psi_{B,1}\end{pmatrix}^\dagger \begin{pmatrix}0 & iV\\ -iV^\dagger & 0\end{pmatrix}\begin{pmatrix}\psi_A\\ \psi_{B,1}\end{pmatrix}.\end{aligned} \tag{6.6}$$

To simplify the problem, we consider a similarity transformation that diagonalizes V and therefore ensures that A and B systems are singly connected. To find the transformation, we perform an SVD decomposition on V:

$$V = U_A U_B^\dagger, \tag{6.7}$$

where U_A and U_B are matrices of shape $N_A \times M$ and $N_B \times M$ such that N_A and N_B is the size of H_A and H_B respectively and M is the rank of V. Through Eq. (6.7) we define the similarity transformation:

$$\begin{pmatrix}\phi_A\\ \phi_B\end{pmatrix} = \begin{pmatrix}U_A^\dagger & 0\\ 0 & U_B^\dagger\end{pmatrix}\begin{pmatrix}\psi_A\\ \psi_{B,1}\end{pmatrix}. \tag{6.8}$$

We then substitute Eq. (6.8) into Eq. (6.6) to find the current in the new basis:

$$\langle\psi|\hat{I}|\psi\rangle = \begin{pmatrix}\phi_A\\ \phi_B\end{pmatrix}^\dagger \sigma_y \begin{pmatrix}\phi_A\\ \phi_B\end{pmatrix}. \tag{6.9}$$

We first construct the scattering matrix for the sub-system A in Eq. (6.4). To achieve this, we decompose $(\phi_A, \phi_B)^T$ onto two full rank basis decompositions of incoming (i) and outgoing modes (o):

$$\begin{pmatrix}\phi_A\\ \phi_B\end{pmatrix} = \begin{pmatrix}\Phi_A^{\mathrm{o}}\\ \Phi_B^{\mathrm{o}}\end{pmatrix} q^{\mathrm{o}} - \begin{pmatrix}\Phi_A^{\mathrm{i}}\\ \Phi_B^{\mathrm{i}}\end{pmatrix} q^{\mathrm{i}}, \tag{6.10}$$

where $\Phi_{A/B}^{\mathrm{i/o}}$ is the matrix of modes of shape $M \times M$ and where q^{i} and q^{o} are the incoming and outgoing mode amplitudes respectively. We relate the incoming and outgoing modes through the scattering equation for subsystem A:

$$q^{\mathrm{o}} = S_A q^{\mathrm{i}}, \tag{6.11}$$

where S_A is the scattering matrix for subsystem A given the definition of incoming/outgoing modes in (6.10). In this basis, the scattering matrix for subsystem A in Eq. (6.4) becomes:

$$\begin{pmatrix}H_A & U_A\Phi_B^{\mathrm{o}}\\ -U_A^\dagger & \Psi_A^{\mathrm{o}}\end{pmatrix}\begin{pmatrix}\Psi_A\\ S_A\end{pmatrix} = \begin{pmatrix}U_A\Phi_B^{\mathrm{i}}\\ \Phi_A^{\mathrm{i}}\end{pmatrix}, \tag{6.12}$$

where Ψ_A is the matrix of column vectors of shape $N_A \times M$ that defines the solution of a system for each incoming mode. To construct the scattering problem for subsystem B scattering matrix S_B in Eq. (6.5), we use the same modes in Eq. (6.10) but now the incoming and outgoing modes switch.

To preserve current, we require the incoming and outgoing modes to carry equal, but opposite current in Eq. (6.9). As a consequence, that enforces unitary S_A and the incoming/outgoing modes to be eigenvectors of the current operator:

$$\begin{pmatrix}\Phi_A^{\mathrm{i/o}}\\ \Phi_B^{\mathrm{i/o}}\end{pmatrix} = \frac{1}{\sqrt{2}}\begin{pmatrix}\Phi_A^{\mathrm{i/o}}\\ \pm i\Phi_A^{\mathrm{i/o}}\end{pmatrix}, \tag{6.13}$$

where we are free to choose any full rank $\Phi_A^{\mathrm{i/o}}$. We refer to this choice of modes as virtual modes.

The scattering matrix S_B contains an additional set of leads and therefore it has the following block structure:

$$S_B = \begin{pmatrix} r_1 & t_1\\ t_2 & r_2\end{pmatrix}, \tag{6.14}$$

where r_1 and r_2 are the reflection matrices for the incoming modes from the virtual and physical leads respectively. Similarly, t_1 and t_2 are the transmission matrices for the outgoing modes for virtual to physical leads and vice versa. Because the virtual modes in S_A are the same as in S_B, we combine the two systems and solve the Dyson equation for the full scattering matrix S:

$$S = r_2 + t_1\left(S_A^{-1} - r_1\right)^{-1} t_2. \tag{6.15}$$

6.4. GENERALISED SHORT JUNCTION THEORY

We choose time-reversal symmetric virtual leads through the SVD decomposition of V as in Eq. (6.7) by ensuring that the incoming and outgoing modes are time-reversed partners of each other:

$$\Phi_A^{\mathrm{o}} = U_A^\dagger T\left(U_A^\dagger\right)^+ \Phi_A^{\mathrm{i}}, \tag{6.16}$$

where T is the time-reversal operator and + superscript indicates the Moore-Penrose pseudoinverse of a matrix. The time-reversal basis of virtual leads is possible whenever hopping V preserves time-reversal symmetry. Because both the superconductor and virtual leads are time-reversal symmetric, S_B is an antisymmetric matrix, $S_B = -S_B^T$, in this basis. Then we carry out a cosine-sine decomposition of S_B [9] to remove the trivial modes that do not couple to the bound states:

$$S_B = \begin{pmatrix} U_1 & 0\\ 0 & U_2\end{pmatrix}\left[\begin{array}{c|cc} \tilde{r} & \tilde{t} & 0\\ \hline -\tilde{t} & \tilde{r} & 0\\ 0 & 0 & I\end{array}\right]\begin{pmatrix} V_1 & 0\\ 0 & V_2\end{pmatrix}, \tag{6.17}$$

where $\tilde{r}, \tilde{t}$ are diagonal real-valued matrices that quantify reflectance/transmission and U, V are unitary matrices. In the basis defined by U, V, the Eq. (6.17) shows that the trivial modes are fully decoupled from the bound states and can be ignored. Therefore, we transform S_A into this basis:

$$\tilde{S}_A = V_1 S_A U_1, \tag{6.18}$$

and re-write the Dyson equation in Eq. (6.15) as:

$$\tilde{S} = \begin{pmatrix}\tilde{r} & 0\\ 0 & I\end{pmatrix} - \begin{pmatrix}\tilde{t}\left(\tilde{S_A}^{-1} - \tilde{r}\right)^{-1}\tilde{t} & 0\\ 0 & 0\end{pmatrix}. \tag{6.19}$$

The only non-trivial eigenvalues (norm < 1) are in the first block of Eq. (6.19):

$$\tilde{S}_{\text{red}} = \tilde{r} - \tilde{t}\left(\tilde{S_A}^{-1} - \tilde{r}\right)^{-1}\tilde{t}. \tag{6.20}$$

In the original basis Eq (6.20) becomes:

$$S_{\text{red}} = r_1^\dagger - V_1^\dagger \tilde{t} V_1 \left(S_A^{-1} - r_1\right)^{-1} U_1 \tilde{t} U_1^\dagger, \tag{6.21}$$

where $r_1 = U_1 \tilde{r} V_1$ and $\tilde{t} = \sqrt{1-\tilde{r}^2}$. Therefore, bound state energies only depend on the incoming modes (from the impurity) that reflect from the normal metallic leads r_1 and not the full scattering matrix S.

6.5. APPLICATION TO A YSR CHAIN

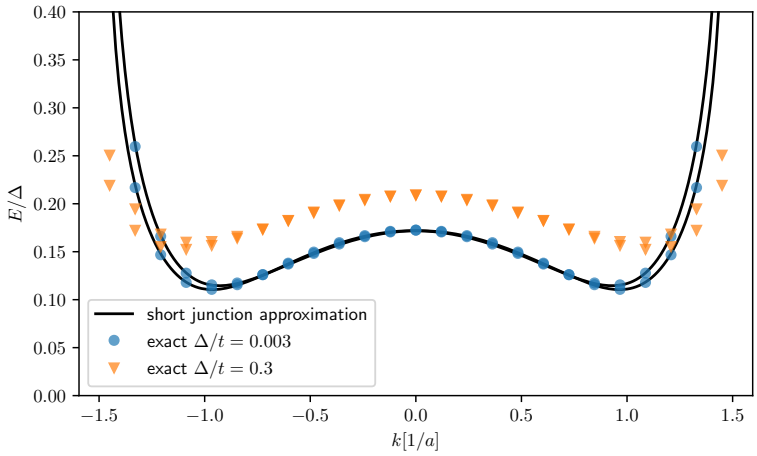

Figure 6.1: Shiba chain subgap dispersion calculated exactly (blue circles and orange triangles) and through the short-junction method (black line).

To test the validity of the approach, we consider a chain of magnetic impurities along the edge of a 2D superconductor. We model the impurities as a tight-binding chain with a single orbital per site and a local magnetic moment J:

$$H_i = \sum_\sigma \left[J(\sigma_z)_{\sigma,\sigma} + \epsilon\right] \sum_m d^\dagger_{m,\sigma} d_{m,\sigma}, \tag{6.22}$$

where $d^\dagger_{m,\sigma}$ is the creation operator of electron on the magnetic impurity site m and spin σ, and the sum over m runs over the sites along a chain. The J term is the exchange coupling between the magnetic impurity and the superconductor and ϵ is the energy of the impurity level. The superconductor is a 2D square lattice that is infinite along the

chain direction and finite but large perpendicular to the chain:

$$H_{SC} = \sum_j \left(\sum_\sigma \left[4t - \mu \right] c^\dagger_{j,\sigma} c_{j,\sigma} + \Delta c^\dagger_{j,\uparrow} c^\dagger_{j,\downarrow} + \text{h.c.} \right) - \sum_{\sigma,\sigma'} \sum_{\langle j,k \rangle} \left(t\delta_{\sigma,\sigma'} + i\alpha \left(\hat{\boldsymbol{r}}_{jk} \times \boldsymbol{\sigma}_{\sigma,\sigma'} \right) \cdot \hat{z} \right) c^\dagger_{j,\sigma} c_{k,\sigma'}, \quad (6.23)$$

where $c^\dagger_{j,\sigma}$ is the creation operator of electron on the superconductor site j with spin σ. The symbol t is the hopping between nearest neighbours, μ is the chemical potential, Δ is the superconducting gap, α is the spin-orbit coupling strength, $\hat{\boldsymbol{r}}_{jk}$ is the unit vector pointing from site j to site k and $\boldsymbol{\sigma}$ is the vector of Pauli matrices. The sum in $\langle j,k \rangle$ runs over the nearest neighbours and h.c. indicates the Hermitian conjugate. We connect the impurity chain to the surface of the superconductor by a simple hopping term:

$$H_B = -t_B \sum_{\langle m,j \rangle} \sum_\sigma d^\dagger_{m,\sigma} c_{j,\sigma} + \text{h.c.}, \quad (6.24)$$

where t_B is the hopping between the impurity chain and the superconductor. The total Hamiltonian then becomes:

$$H = H_{SC} + H_i + H_B. \quad (6.25)$$

We numerically diagonalize the full tight-binding model of Eq. (6.25) with 5000 superconductor atoms perpendicular to the chain to find the exact subgap dispersion of the YSR states. We use the parameters $t = 1, \epsilon = 0.2, t_B = 0.75, \mu = 2, J = 0.7, \alpha = 0.1$ and $\Delta = 0.003$ We then compute the subgap dispersion according to the short-junction method through Eqs. (6.21) and (6.2) and compare to the exact results in Fig. 6.1. For small values of Δ, the short-junction method is in good agreement with the exact results. However, when Δ increases, the coherence length becomes comparable to the distance between the impurity and the superconductor and the short-junction method breaks down.

6.6. CONCLUSSION

We generalised the theory of the short-junction approximation to calculate the subgap bound state energies of systems in contact with a superconducting lead. We showed that the bound state energies only depend on the incoming modes that reflect from the normal metallic leads and not the full scattering matrix. The advantage of this approach is that it does not require modelling the full superconductor explicitly and the system of equations is linear, making it a computationally efficient method to calculate the subgap bound state energies.

REFERENCES

[1] A. Kastalsky, A. W. Kleinsasser, L. H. Greene, R. Bhat, F. P. Milliken, and J. P. Harbison, *Observation of pair currents in superconductor-semiconductor contacts*, Physical Review Letters **67**, 3026 (1991).

[2] W. Chang, S. M. Albrecht, T. S. Jespersen, F. Kuemmeth, P. Krogstrup, J. Nygård, and C. M. Marcus, *Hard gap in epitaxial semiconductor–superconductor nanowires*, Nature Nanotechnology **10**, 232 (2015).

[3] J. O. Island, R. Gaudenzi, J. de Bruijckere, E. Burzurí, C. Franco, M. Mas-Torrent, C. Rovira, J. Veciana, T. M. Klapwijk, R. Aguado, and H. S. van der Zant, *Proximity-induced shiba states in a molecular junction,* Physical Review Letters **118** (2017), 10.1103/physrevlett.118.117001.

[4] R. M. Lutchyn, E. P. A. M. Bakkers, L. P. Kouwenhoven, P. Krogstrup, C. M. Marcus, and Y. Oreg, *Majorana zero modes in superconductor–semiconductor heterostructures,* Nature Reviews Materials **3**, 52 (2018).

[5] L. Schneider, P. Beck, T. Posske, D. Crawford, E. Mascot, S. Rachel, R. Wiesendanger, and J. Wiebe, *Topological shiba bands in artificial spin chains on superconductors,* Nature Physics **17**, 943 (2021).

[6] M. Istas, C. Groth, and X. Waintal, *Pushing the limit of quantum transport simulations,* Physical Review Research **1** (2019), 10.1103/physrevresearch.1.033188.

[7] M. Istas, C. Groth, A. Akhmerov, M. Wimmer, and X. Waintal, *A general algorithm for computing bound states in infinite tight-binding systems,* SciPost Physics **4** (2018), 10.21468/scipostphys.4.5.026.

[8] B. van Heck, S. Mi, and A. R. Akhmerov, *Single fermion manipulation via superconducting phase differences in multiterminal josephson junctions,* Phys. Rev. B **90**, 155450 (2014).

[9] C. W. J. Beenakker, *Random-matrix theory of quantum transport,* Reviews of Modern Physics **69**, 731 (1997).

ACKNOWLEDGMENTS

I would like to express my sincere gratitude to my supervisors, Anton and Michael, for the chance to pursue a PhD here. The productive and friendly group environment you fostered not only made me a better researcher but also provided a joyful time that kept me motivated to learn new skills every day. To Anton, it was a privilege to work closely with you — the way of thinking and approach to problems I apply now is, in no small part, based on learning directly from you. To Antonio, I have been blessed to have you as a research collaborator and, more importantly, a great friend. Thank you, Isidora, for your unwavering support throughout my time here. Your motivation and drive are inspiring, and I look forward to working with you in the future. I extend my gratitude to Juan, Johanna, and Ivan for the light-hearted coffee break discussions. A big thanks to Hélène: your boundless creativity was incredibly refreshing and often inspired my imagination in various projects. Thanks to all Quantum Tinkerers; you were a pleasure to be around, and I'll always look back fondly on our morning coffee discussions. I would also like to thank Hristo for all the thought-provoking discussions we had. Last but not least, I am forever grateful to my parents and sisters. I definitely could not be where I am today without your support.

CURRICULUM VITÆ

Kostas VILKELIS

28-05-1995 Born in Vilnius, Lithuania.

EDUCATION

2014–2019 MChemPhys (Hons) Chemical Physics with Industrial Experience
University of Edinburgh, Edinburgh, United Kingdom
Thesis: Reflectivity Evolution of Potassium under Extreme Pressure
Supervisor: Dr. Andreas Hermann

2019–2024 PhD in Condensed Matter Physics
Delft University of Technology, Delft, Netherlands

Thesis: Coherent manipulation of normal and Andreev Fermions
Promotor: Dr. Anton R. Akhmerov
Copromotor: Dr. Michael T. Wimmer

List of Publications

1. **Kostas Vilkelis**, Antonio Manesco, Juan Daniel Torres Luna, Sebastian Miles, Michael Wimmer, Anton Akhmerov *Fermionic quantum computation with Cooper pair splitters*, arXiv:2309.00447

2. **Kostas Vilkelis**, Ady Stern, Anton Akhmerov *Aharonov-Bohm magnetism in open Fermi surfaces*, arXiv:2303.04310

3. Chun-Xiao Liu, Sergej Schuwalow, Yu Liu, **Kostas Vilkelis**, A. L. R. Manesco, P. Krogstrup, and Michael Wimmer *Electronic properties of InAs/EuS/Al hybrid nanowires*, Phys. Rev. B 104, 014516

4. **Kostas Vilkelis**, Lin Wang, Anton Akhmerov *Bloch-Lorentz magnetoresistance oscillations in delafossites*, SciPost Phys. 15, 019